

THE UNIVERSITY OF CHICAGO

A MEASUREMENT OF THE BRANCHING RATIO OF THE π^0 DALITZ
DECAY USING $K_L \rightarrow 3\pi^0$ DECAYS FROM KTEV

A DISSERTATION SUBMITTED TO
THE FACULTY OF THE DIVISION OF THE PHYSICAL SCIENCES
IN CANDIDACY FOR THE DEGREE OF
DOCTOR OF PHILOSOPHY

DEPARTMENT OF PHYSICS

BY
ERIN E. ABOUZOID

CHICAGO, ILLINOIS

AUGUST 2007

Copyright © 2007 by Erin E. Abouzaid

All rights reserved

ABSTRACT

We present a measurement of $B(\pi^0 \rightarrow e^+e^-\gamma)/B(\pi^0 \rightarrow \gamma\gamma)$ using data taken in 1999 by the E832 KTeV experiment at Fermilab. The π^0 s were produced by K_L decays in flight that are fully reconstructed. We find 63,693 $K_L \rightarrow 3\pi^0 \rightarrow \gamma\gamma \gamma\gamma e^+e^-\gamma$ decays in KTeV data (an increase of a factor of ~ 20 in event statistics over previous experiments), and normalize to $K_L \rightarrow 3\pi^0 \rightarrow 6\gamma$, to extract

$$B(\pi^0 \rightarrow e^+e^-\gamma, m_{e^+e^-} > 15\text{MeV}/c^2)/B(\pi^0 \rightarrow \gamma\gamma) = (3.920 \pm 0.016 \pm 0.036) \times 10^{-3},$$

where the first error is statistical and the second is systematic. Using the Mikaelian and Smith prediction for the e^+e^- mass spectrum as implemented in the KTeV Monte Carlo to correct to the full e^+e^- mass range yields

$$B(\pi^0 \rightarrow e^+e^-\gamma)/B(\pi^0 \rightarrow \gamma\gamma) = (1.1559 \pm 0.0046 \pm 0.0107)\%.$$

This result is consistent with previous measurements and with theoretical predictions, and the uncertainty is a factor of three smaller than any previous measurement.

ACKNOWLEDGMENTS

There are many people who deserve thanks for their contributions to this thesis and to my graduate school career, either directly or indirectly. First, thanks to Ed Blucher for being both an excellent advisor and a great friend. He helped me to envision what KTeV was like when it was taking data and to understand the detector. I learned so much from him about data analysis, and he always helped me keep the big picture in mind. Second, thanks to Rick Kessler and Sasha Glazov; I could not have done this analysis without their suggestions, help, and guidance. They are both amazing sources of knowledge about the details of the KTeV detector, simulation, and analysis.

Thanks, of course, to all the people who built and ran the KTeV detector – this analysis is built on their work. Several people in the KTeV collaboration deserve special mention. Thanks to Bob Tschirhart for his useful suggestions at collaboration meetings and for being at DPF. Thanks to Mike Wilking for helpful discussions about the simulation's radiative corrections to the Dalitz decay. Thanks to Elliott Cheu for helping me with several computing issues when the HelpDesk couldn't. Thanks also to Steve Timm and Margaret Greaney at the Fermilab HelpDesk who did help me with countless computing problems, both real and imagined. Additionally, thanks to Ben Lillie, a Chicago-Argonne postdoc, with whom I had useful discussions about radiative corrections. Thanks for bridging the wide gap between the way theory papers describe the calculations and the way I could understand them.

Other faculty members here also deserve thanks. I am grateful to Henry Frisch for giving me the opportunity to work with him during my first year in Chicago. Mark Oreglia invited me to become involved in several outreach programs with a local public school which I enjoyed immensely. Thanks also to Stuart Gazes; even after I was finished with my classes, I knew he cared about how I was doing.

I am fortunate to have been surrounded by an excellent group of graduate and undergraduate students during my time here. During first and second year, Collin Wolfe and Jahred Adelman were great homework partners, and since then, we have eaten a lot of tea and cookies together. Gabe Perdue and Jon Nix were always around, and always willing to help me when I came to their office. No matter what random problem (dying power supply batteries, accidentally locking my computer screen, forgetting my keys) I was having, they had an answer for me and, sometimes, a retro candy bar. It was great to have Martina Hurwitz around for a couple years before she went off to CERN; best of luck to her. It was also great to work with an outstanding set of undergrads – David Underwood, Jen Seger, Abby Kaboth, and Nathan Whitehorn among others.

All sorts of things would have been a lot harder without Nobuko McNeill, Mary Heintz, and Aspasia Sotir-Plutis. From registering for classes to fixing various computer issues to getting my paycheck and mail, you all helped me figure out lots of day-to-day things here. I owe Aspasia thanks for her candy jar, which I frequented when in need of some chocolate or just a kind word from her.

I would also like to thank the science and math teachers I was lucky enough to learn from during my years of secondary schooling: Ms. Simmons, Mrs. Hollick, Mrs. Pringle, Mrs. Edmonds, Mr. Godshall, Mrs. Bair, and Mr. Battaglia. Your excitement about science and math was infectious and your confidence in me made me want to challenge myself. My math and science professors at the University of Richmond were excellent teachers who made a point of giving students an incredible amount of individual time and attention. I learned so much from Dr. Kerckhove, Dr. Davis, Dr. Nall, Dr. Charlesworth, Dr. Rubin, Dr. Guilfoyle, Dr. Vineyard, and Dr. Fetea. They set me on the path to graduate school.

I owe enormous thanks to my family. My parents have always encouraged me to

do my best and have been there for me, together with Travis and Susan, for all the ups and downs along the way. Finally, I am grateful to my husband, Mohammed. He saw me through the late nights of homework during the first year of classes, the agony of studying for the candidacy exam, and all of my research-related frustrations. His willingness to listen to me explain analysis code was often the key to me stumbling onto answers to problems I was having. For so many things, thank you.

TABLE OF CONTENTS

| | |
|--|-----------|
| ABSTRACT | iii |
| ACKNOWLEDGMENTS | iv |
| LIST OF FIGURES | xi |
| LIST OF TABLES | xviii |
| 1 INTRODUCTION | 1 |
| 1.1 Motivation for Studying $B(\pi^0 \rightarrow e^+e^-\gamma)/B(\pi^0 \rightarrow \gamma\gamma)$ | 1 |
| 1.2 The Neutral Pion: Properties and Decays | 2 |
| 1.3 Theoretical Predictions | 4 |
| 1.3.1 $B(\pi^0 \rightarrow \gamma\gamma)$ and the $\pi^0\gamma\gamma$ Form Factor | 4 |
| 1.3.2 $B(\pi^0 \rightarrow e^+e^-\gamma)$ at Leading Order | 5 |
| 1.3.3 Radiative Corrections to $B(\pi^0 \rightarrow e^+e^-\gamma)$ | 8 |
| 1.4 Previous Measurements of $B(\pi^0 \rightarrow e^+e^-\gamma)/B(\pi^0 \rightarrow \gamma\gamma)$ | 12 |
| 1.5 Overview of this Dissertation | 14 |
| 2 THE KTEV DETECTOR | 16 |
| 2.1 Overview of the Detector | 16 |
| 2.2 Beamline and Target | 18 |
| 2.2.1 Experimental Coordinate System | 19 |
| 2.2.2 Purifying and Collimating the Beams | 19 |
| 2.2.3 Accidental Counters | 21 |
| 2.3 Decay Region: Vacuum and Regenerator Beams | 21 |
| 2.4 Spectrometer | 23 |
| 2.4.1 Analysis Magnet | 23 |
| 2.4.2 Drift Chambers | 24 |
| 2.5 The CsI Calorimeter | 28 |
| 2.5.1 Digitization | 30 |
| 2.5.2 Energy Calibration | 31 |
| 2.6 Veto System | 34 |
| 2.6.1 Photon Veto Counters | 34 |
| 2.6.2 The Regenerator | 36 |
| 2.6.3 The Mask Anti | 37 |
| 2.6.4 The Collar Anti | 37 |
| 2.6.5 The Hadron Anti and Back Anti | 38 |
| 2.6.6 Muon Veto Counters | 38 |
| 2.7 Trigger System | 39 |
| 2.7.1 Trigger Hodoscope: VV' Counters | 40 |

| | | |
|-------|--|----|
| 2.7.2 | Level 1 Trigger | 40 |
| 2.7.3 | Level 2 Trigger | 42 |
| 2.7.4 | Level 1 and 2 Trigger Definitions | 43 |
| 2.7.5 | Level 3 Trigger and Online Data Split | 44 |
| 3 | DATA ANALYSIS | 46 |
| 3.1 | Overview of Analysis Technique | 46 |
| 3.2 | Trigger and Veto Requirements | 47 |
| 3.2.1 | Trigger Elements Common to Both Modes | 47 |
| 3.2.2 | Trigger Elements Unique to Signal Mode | 48 |
| 3.2.3 | Equalizing the HA and MU2 Requirements in the Two Triggers | 49 |
| 3.2.4 | Level 3 Trigger Requirements | 50 |
| 3.3 | Data Sample Integrity | 50 |
| 3.4 | Event Reconstruction | 53 |
| 3.4.1 | Track Finding | 53 |
| 3.4.2 | Clustering | 57 |
| 3.5 | Reconstructing the Decay Vertex | 59 |
| 3.5.1 | Vertex z Position: Normalization Mode | 59 |
| 3.5.2 | Pairing χ^2 | 61 |
| 3.5.3 | Vertex z Position: Signal Mode | 63 |
| 3.5.4 | The Energy Scale | 64 |
| 3.5.5 | Vertex x and y Positions | 65 |
| 3.6 | Reconstructing the Mass | 67 |
| 3.7 | Selection Criteria | 68 |
| 3.7.1 | Criteria Used in Both Signal and Normalization Modes | 68 |
| 3.7.2 | Criteria Unique to Signal Mode | 73 |
| 3.8 | Final Data Samples | 80 |
| 4 | MONTE CARLO SIMULATION | 84 |
| 4.1 | Overview of Simulation | 84 |
| 4.2 | MC Beamline and Detector Geometry | 85 |
| 4.3 | Kaon Propagation and Decay | 85 |
| 4.4 | Accidental Overlays | 86 |
| 4.5 | Simulation of the Drift Chambers | 88 |
| 4.6 | Simulation of the CsI Calorimeter | 89 |
| 4.7 | Simulation of the Veto Counters | 91 |
| 4.8 | Simulation of the Trigger | 91 |
| 4.9 | Aspects of the Simulation Important for this Analysis | 91 |
| 4.9.1 | Unsmearing the Cluster Positions | 92 |
| 4.9.2 | Radiative Corrections to the Dalitz Decay | 93 |
| 4.10 | Background Simulation | 95 |

| | | |
|--------|--|-----|
| 5 | RESULTS | 96 |
| 5.1 | Monte Carlo Acceptance | 96 |
| 5.2 | Corrections to the MC Acceptance | 98 |
| 5.2.1 | Tracking Inefficiency Correction | 98 |
| 5.2.2 | Trigger Inefficiency Correction | 99 |
| 5.2.3 | Corrected Acceptances | 100 |
| 5.3 | Calculation of $B(\pi^0 \rightarrow e^+e^-\gamma)/B(\pi^0 \rightarrow \gamma\gamma)$ | 100 |
| 6 | SYSTEMATIC UNCERTAINTIES | 103 |
| 6.1 | Tracking Inefficiency | 103 |
| 6.2 | Radiative Corrections | 106 |
| 6.2.1 | The Reconstructed $e^+e^-\gamma$ Mass | 107 |
| 6.2.2 | The Reconstructed e^+e^- Mass | 109 |
| 6.2.3 | The Distribution of the Number of Software Clusters | 110 |
| 6.3 | Detector Material | 113 |
| 6.4 | Accidentals | 115 |
| 6.4.1 | Study Using the SOD Distribution | 115 |
| 6.4.2 | Study Using Software Clusters | 117 |
| 6.5 | Relative Trigger Inefficiency | 120 |
| 6.6 | $3\pi^0$ Trigger Inefficiency | 121 |
| 6.7 | $3\pi^0$ Trigger Prescale | 122 |
| 6.7.1 | Study Using Trigger 5 Random Accepts | 123 |
| 6.7.2 | Study Using Scaler Data | 123 |
| 6.8 | Form Factor | 125 |
| 6.9 | Photon Inefficiency | 126 |
| 6.10 | Background | 127 |
| 6.11 | Cut Variations | 129 |
| 6.11.1 | Varying the Vertex z Requirement | 131 |
| 6.11.2 | Varying the Cell Separation Requirement | 131 |
| 6.11.3 | Varying the e^+e^- Mass Requirement | 131 |
| 6.12 | e^+e^- Mass Scale | 133 |
| 6.13 | Monte Carlo Statistics | 133 |
| 6.14 | Other Systematics Checks | 133 |
| 7 | CROSS CHECKS | 135 |
| 7.1 | Cell Separation Dependence | 135 |
| 7.2 | e^+e^- Mass Dependence | 138 |
| 7.3 | Intensity Dependence | 140 |
| 7.4 | Run Dependence | 149 |
| 7.5 | Inbends versus Outbends | 152 |
| 7.6 | Magnet Polarity | 153 |

| | | |
|-------|--|-----|
| 8 | CONCLUSION | 156 |
| 8.1 | Final Result | 156 |
| 8.2 | Comparison to Previous Measurements and to Theory | 157 |
| 8.3 | Effect of New Result on Other Measurements | 157 |
| 8.3.1 | Correcting the KTeV measurement of $B(\pi^0 \rightarrow e^+e^-)$ | 159 |
| 8.3.2 | Correcting the KTeV measurement of $B(K_L \rightarrow e^+e^-\gamma)$ | 161 |
| | REFERENCES | 163 |

LIST OF FIGURES

| | | |
|-----|--|----|
| 1.1 | The Feynman diagram for the most common decay mode of the neutral pion, $\pi^0 \rightarrow \gamma\gamma$. k_1 and k_2 are the momenta of the photons; ϵ_1 and ϵ_2 are the polarizations. | 3 |
| 1.2 | The Feynman diagram for the π^0 Dalitz decay, $\pi^0 \rightarrow e^+e^-\gamma$. The virtual photon, γ^* , immediately internally converts to the e^+e^- pair. | 4 |
| 1.3 | The Feynman diagrams for the virtual corrections to π^0 Dalitz decay, $\pi^0 \rightarrow e^+e^-\gamma$. The left diagram represents an electromagnetic loop correction to the virtual photon line, and the right diagram shows photon exchange between the e^+ and e^- lines. | 10 |
| 1.4 | The Feynman diagrams for the real (bremsstrahlung) corrections to π^0 Dalitz decay, $\pi^0 \rightarrow e^+e^-\gamma$. Each of these counts twice, since there are two other identical diagrams with the radiative and decay photons interchanged. | 10 |
| 2.1 | The KTeV detector in the E832 configuration, viewed from above. . . | 17 |
| 2.2 | The KTeV beamline, as viewed from above. The target is located at $z = 0$ | 20 |
| 2.3 | (a) Diagram of the regenerator, and (b) detailed view of the downstream end of the regenerator. The kaon beam enters from the left. . . | 22 |
| 2.4 | The drift chamber cells are formed by the six field wires (open circles) around each sense wire (black dots). The vertical dashed lines are the boundaries of the off-set cells, formed by the other plane in the same view. | 25 |
| 2.5 | A typical charged particle track through a drift chamber. The thin lines are the drift paths of the ionization electrons towards the sense wires. | 27 |
| 2.6 | Transverse view of the CsI calorimeter. There are 868 5.0×5.0 cm ² outer crystals and 2232 2.5×2.5 cm ² inner crystals. The beam holes are 15×15 cm ² each and are 30 cm apart from center to center. . . . | 29 |
| 2.7 | CsI calibration using electrons from $K_L \rightarrow \pi^\pm e^\mp \nu$ decays. Figure courtesy of E. Worcester. | 32 |
| 2.8 | Energy resolution of the calorimeter. Figure courtesy of E. Worcester. | 33 |
| 2.9 | Three-dimensional cut-away view of the KTeV apparatus. The components that differ between E799 and E832 are labelled; recall that this analysis uses the E832 configuration. Figure courtesy of E. Pod. . . . | 35 |

| | | |
|------|--|----|
| 2.10 | (a) Transverse view of a ring counter photon veto detector. Five of these are between the regenerator and the vacuum window. The square hole is approximately 1 meter. (b) Mask anti (MA) photon veto detector at $z = 123$ m. The beam holes are 9×9 cm ² , and they are separated by 20 cm from center to center. The black areas represent the active veto region on both diagrams. The PMTs are located at the outer edges of the two detectors. | 36 |
| 2.11 | The collar anti (CA) is the dark square surrounding each of the calorimeter's beam holes. The inner 1.50 cm (60%) of the crystals around each beam hole are covered by the CA. The beams travel into the page. Wavelength-shifting fibers transmit signals to the PMTs at the outer edges of the calorimeter. | 37 |
| 2.12 | Diagram of the V and V' (also called V0 and V1) banks that make up the trigger hodoscope. The V counters are offset from the V' counters by half a paddle to minimize the possibility of missing a charged particle. The dark squares are the beam holes. | 41 |
| 3.1 | The sigma distribution, fit to a gaussian, for the ratio of trigger 6 ($3\pi^0$) events to trigger 14 (Dalitz) events in each DAQ plane in each run, relative to the average ratio over all included runs. | 52 |
| 3.2 | Diagram of types of SODs and hits used in the track-finding algorithm. The diamonds are sense wire positions in the drift chamber and the vertical dashed lines are the tracks. The horizontal solid lines are the true drift distances; the horizontal dotted lines show the same drift distance for a track on the opposite side of the sense wire. The pairs that the tracking algorithm would find in this example are described in the text. | 55 |
| 3.3 | The three ways to pair four photons to make two π^0 s. Pairing (a) is the best pairing, since the two vertices are at the same position, within reconstruction uncertainties. Both modes in this analysis have more possible pairings (15 each) since there are more than four photons in the final states, but this diagram illustrates the basic idea of reconstructing the π^0 s by looking at all possible pairing combinations. | 62 |
| 3.4 | The pairing χ^2 distributions in the data for both the signal and normalization mode samples. The arrow indicates the analysis requirement that the pairing χ^2 be less than 75 in each sample in order to reduce cases of mispairing. | 63 |

| | | |
|------|--|----|
| 3.5 | The reconstructed vertex z position for $K_L \rightarrow 3\pi^0$ decays in the regenerator beam. The dots are data and the solid histogram is Monte Carlo. The downstream end of the regenerator is located at about $z = 125.5$ m. In (a), the energy scale has not been applied, and the data-Monte Carlo mismatch is clear. In (b), an energy scale of 0.9985 has been applied to the data, and the data and Monte Carlo agree. | 66 |
| 3.6 | The data to Monte Carlo overlay of the shape χ^2 distribution, in both signal and normalization modes. The dots are data and the solid histogram is Monte Carlo. All selection criteria have been applied, except the one on the shape χ^2 . The arrow indicates the selection requirement of a shape χ^2 of 100 or less. | 72 |
| 3.7 | The ring number distribution in data, in both signal and normalization modes. All selection criteria have been applied, except the one on the ring number. The arrow indicates the selection requirement of a ring number of 110 or less. | 74 |
| 3.8 | The E/p distribution for the track with the higher momentum. All selection criteria have been applied except the requirement that E/p be greater than 0.9. The arrow indicates where this cut is. | 75 |
| 3.9 | The vertex χ^2 distribution in data. All selection criteria have been applied except the requirement that the vertex χ^2 be less than 100. The arrow indicates where this cut is. | 76 |
| 3.10 | The brem- γ distance in data. The brem- γ distance is defined as the distance between the projection of the upstream track segment at the CsI and the nearest neutral cluster. All selection criteria have been applied except the requirement on the brem- γ distance; that requirement is that the brem- γ distance must be more than 1 cm, as indicated by the arrow. | 78 |
| 3.11 | The definition of the wire-centered cells used in the cell separation cut. In the diagram, Track 2 is three cells away from Track 1, while Track 3 is six cells from Track 1. | 79 |
| 3.12 | The e^+e^- mass distribution. The top line is the distribution for all generated events, the middle line is the distribution with all selection requirements except the cell separation cut (and except the requirement on the e^+e^- mass itself), and the bottom line is the e^+e^- mass distribution with all selection requirements (except that on the e^+e^- mass). | 81 |
| 3.13 | (a) The reconstructed $3\pi_D^0$ mass and (b) the reconstructed $e^+e^-\gamma$ mass in the signal (Dalitz) mode. The dots are data, and the solid histogram is Monte Carlo. All cuts have been applied except the cut on the quantity plotted. | 82 |

| | | |
|------|---|-----|
| 3.14 | The reconstructed $3\pi^0$ mass in the normalization mode. The dots are data, and the solid histogram is Monte Carlo. All cuts have been applied except the cut on the reconstructed $3\pi^0$ mass. | 83 |
| 6.1 | The left plots show the data to nominal Monte Carlo overlay and ratio for the reconstructed $e^+e^-\gamma$ mass. The right plots are the overlay and ratio for the reconstructed $e^+e^-\gamma$ mass in data and Monte Carlo with no radiative corrections. All selection criteria have been applied except for the requirement on the reconstructed $e^+e^-\gamma$ mass. The dots are data; the solid histogram is MC. | 108 |
| 6.2 | The left plots show the data to nominal Monte Carlo overlay and ratio for the reconstructed e^+e^- mass. The right plots are the overlay and ratio for the reconstructed e^+e^- mass in data and Monte Carlo with no virtual corrections. All selection criteria have been applied except the requirement on the reconstructed e^+e^- mass and the cell separation requirement; the sample includes events with cell separation of one and greater (the nominal requirement is cell separation greater than three). The dots are data; the solid histogram is MC. | 111 |
| 6.3 | Data to Monte Carlo overlays of the number of software clusters in Dalitz mode. The left plots are nominal MC and the right plots are MC with no radiative corrections. The top plots are the overlays and the bottom plots are the data to MC ratios. The dots are data and the solid histogram is MC. | 112 |
| 6.4 | Data to MC overlays of the distribution of the brem- γ distance at the calorimeter. The data are compared to nominal MC, to MC with no bremsstrahlung, to MC with no radiative corrections, and to MC with no bremsstrahlung and no radiative corrections. The dots are data and the solid histogram is MC. All selection criteria have been applied except for the requirement on the brem- γ distance; this requirement is that the brem- γ distance be greater than 1 cm, and is indicated by the arrow on each plot. | 114 |
| 6.5 | Data to Monte Carlo overlays of drift chamber sum-of-distance (SOD) distributions for one of the x tracks in DC1. The top plot is nominal MC and the bottom plot is MC without accidentals. The dots are data and the solid histogram is MC. Deviation between SOD and cell spacing is shown, so zero deviation means SOD=6.35mm, and negative deviations are low SODs. | 116 |
| 6.6 | Data to Monte Carlo overlays of the distribution of the number of software clusters. The dots are data and the solid histogram is MC. The top plot is the nominal MC and the bottom plot is the MC without accidentals. | 119 |

| | | |
|------|---|-----|
| 6.7 | The sigma distribution for the ratio of trigger 6 events after the hardware prescale to trigger 6 events before the hardware prescale for each run used in the nominal analysis, relative to the average ratio over all these runs. | 124 |
| 6.8 | The reconstructed vertex z position of events with a photon conversion, focusing on the region near the vacuum window (at $z = 159$ m). The plots on the left show the reconstructed vertex position based on the neutral clusters in the calorimeter (the photons from two of the π^0 s). The plots on the right are the reconstructed vertex z position based on the vertex of the two tracks. The top plot on each side is before cuts, the middle plot is after all cuts except the cell separation requirement, and the bottom plot is after all cuts. In the top-right and middle-right plots, the spike at the vacuum window is visible, indicating that the tracks are from photon conversions there. Note that the vertex z requirement in the analysis applies to the z reconstructed from the neutral clusters. Also note that seven events remain after all cuts, although none of them are near the vacuum window, and so do not appear in the bottom two plots. | 128 |
| 6.9 | The reconstructed kaon z -vertex for both modes, after all selection requirements except the z requirement. The top plots are the data to MC overlays, where the dots are data and the solid histogram is Monte Carlo. The bottom plots are the data to MC ratios. | 130 |
| 6.10 | Data to MC overlays and ratios of the reconstructed cell separation of the tracks in the Dalitz mode. The dots are data and the solid histogram is MC. The left pair of plots is after all selection requirements except the cell separation cut, and the right pair is after all selection requirements. | 132 |
| 7.1 | The ratio of branching ratios versus cell separation. The Dalitz events (both data and reconstructed MC events) that contribute to the answer in each of the first six bins are the events which have a minimum cell separation equal to the bin number. For example, the events in the cell separation = 0 bin all have a minimum cell separation of exactly 0. The last (seventh) point includes the rest of the events, that is, events which have a minimum cell separation greater than or equal to six. The error bars represent the independent statistical uncertainty in each bin. The solid horizontal line is the weighted average, and the dashed horizontal lines indicate the statistical uncertainty on the weighted average. | 136 |

- 7.2 The ratio of branching ratios for the nominal sample on the right and for the sample of Dalitz events with low cell separations (less than or equal to 3 cells) on the left. The events in the low cell separation sample pass all other selection requirements. The error bars on the points indicate the uncertainty from the data and MC statistics on the Dalitz events in each (independent) sample. The solid line is the weighted average of the two points, and the dashed lines are the uncertainty on the weighted average. 137
- 7.3 The result for events with e^+e^- mass between 10 and 15 MeV/c^2 that pass all other selection criteria, and the result for events in the nominal sample ($m_{e^+e^-} > 15 \text{ MeV}/c^2$). The error bars correspond to the independent statistical uncertainties in the two samples. The solid line is the weighted average and the dashed lines are the uncertainty on the weighted average. 139
- 7.4 The dots are the ratio of branching ratios in each intensity sample. Note that the medium and high intensity samples are subsets of the nominal sample, while the low intensity sample is from a special set of runs described in the text. The solid line is the weighted average and the dashed lines indicate the uncertainty on the weighted average. . . 143
- 7.5 The dots are the result in the two intensity samples using nominal MC; the boxes are MC with no accidentals. The solid lines are the weighted averages of the result in the medium and high intensity samples for nominal MC and for MC with no accidentals. The dashed lines indicate the uncertainties on the weighted averages. 145
- 7.6 The points are the ratio of branching ratios in each of the eight subsamples described in the text. The run range and the average intensity is given for each subsample. The boxes indicate the results in the high intensity subsamples, while the dots indicate the results in the medium intensity subsamples. The error bars are the independent statistical uncertainties on each point. The solid line is the weighted average and the dashed lines indicate the uncertainty on the weighted average. . . 146
- 7.7 The points are the ratio of branching ratios of $K_L \rightarrow \pi^\pm e^\mp \nu$ (denoted Ke3) to $K_L \rightarrow 3\pi^0$ in each of the eight subsamples described in the text. The small numbers at the bottom of the plot are average intensity ($\times 10^{12}$) in each subsample. The boxes indicate the results in the high intensity subsamples, while the dots indicate the results in the medium intensity subsamples. The error bars are the independent statistical uncertainties on each point. The solid line is the weighted average and the dashed lines indicate the uncertainty on the weighted average. The small arrows outside the plot show the expected separation if the Ke3/ $3\pi^0$ high versus medium has the same ($\sim 2.4\%$) discrepancy as the Dalitz to $3\pi^0$ ratio of branching ratios. Figure courtesy of R. Kessler. 148

| | | |
|------|--|-----|
| 7.8 | The ratio of branching ratios versus run, for medium intensity runs, which are defined as runs 13670 through 14104. (Note that this does not exactly correspond to the medium intensity sample, since events for the medium intensity sample are selected on a spill-by-spill basis.) Only runs which have a non-zero number of events are included. The error bars on the points are based on the independent statistical uncertainty in each run. The line is the weighted average across all medium intensity runs. | 150 |
| 7.9 | The ratio of branching ratios versus run, for high intensity runs, which are defined as runs 14105 through 14523. (Note that this does not exactly correspond to the high intensity sample, since events for the high intensity sample are selected on a spill-by-spill basis.) Only runs which have a non-zero number of events are included. The error bars on the points are based on the independent statistical uncertainty in each run. The line is the weighted average across all of the high intensity runs. | 151 |
| 7.10 | The track configuration corresponding to (a) an inbend event and (b) an outbend event. | 153 |
| 7.11 | The ratio of branching ratios in the two subsamples of the nominal sample corresponding to which way the tracks bend at the magnet, denoted inbends and outbends. The uncertainties on the two points are based on the reconstructed Dalitz event statistics in data and MC. The solid line is the weighted average and the dashed lines indicate the uncertainty on the weighted average. | 154 |
| 7.12 | The ratio of branching ratios in the two subsamples of the nominal sample corresponding to the two analysis magnet polarities. The uncertainties on the two points are based on the reconstructed event statistics in data and MC for both decay modes. The solid line is the weighted average and the dashed lines indicate the uncertainty on the weighted average. | 155 |
| 8.1 | A comparison of previous measurements, theoretical predictions, and this KTeV measurement of $B(\pi^0 \rightarrow e^+e^-\gamma)/B(\pi^0 \rightarrow \gamma\gamma)$ | 158 |
| 8.2 | The recent KTeV result for $B(\pi^0 \rightarrow e^+e^-)$, using the 2006 PDG average for the normalization decay mode ($\pi^0 \rightarrow e^+e^-\gamma$) branching ratio (left) and corrected using this new result for the $\pi^0 \rightarrow e^+e^-\gamma$ branching ratio (right). | 160 |
| 8.3 | The recent KTeV result for $B(K_L \rightarrow e^+e^-\gamma)$, using the 2006 PDG average for $B(\pi^0 \rightarrow e^+e^-\gamma)$ in the normalization decay mode branching ratio (left) and corrected using this new result for the $\pi^0 \rightarrow e^+e^-\gamma$ branching ratio (right). | 162 |

LIST OF TABLES

| | | |
|-----|---|-----|
| 2.1 | z -positions of the midplanes of the four drift chambers and the analysis magnet. | 23 |
| 2.2 | Z -positions of the photon veto counters: ring counters (RCs), spectrometer antis (SAs), and Cesium Iodide anti (CIA). | 34 |
| 2.3 | Z -positions of the detector components downstream of the calorimeter. | 38 |
| 3.1 | Selection criteria for signal and normalization modes. | 69 |
| 5.1 | Number of events reconstructed in data and Monte Carlo and number of events generated in Monte Carlo for both signal and normalization decay modes. | 96 |
| 5.2 | The Monte Carlo acceptances (with uncertainties) for both normalization ($3\pi^0$) and signal (Dalitz) modes. The Dalitz mode acceptance has been corrected for the tracking and trigger inefficiencies as described in the text. | 100 |
| 6.1 | Summary of systematic errors. | 103 |
| 6.2 | Tracking inefficiencies in $K_L \rightarrow \pi^+\pi^-\pi^0$ data and Monte Carlo, for both medium and high intensity. The correction applied to the acceptance is the difference between the total data inefficiency and the total MC inefficiency. The bottom section of the table gives the inefficiencies for MC events in which no accidentals were included. | 105 |
| 6.3 | The width (and error on the width) of the gaussian fit to the reconstructed $e^+e^-\gamma$ mass distribution in data, nominal Monte Carlo, and Monte Carlo with no radiative corrections. The third column gives the data-MC difference in width in terms of the number of sigma, for both nominal MC and MC with no radiative corrections. The χ^2 per degree of freedom of the data to MC overlay is also given. | 109 |
| 6.4 | The percent change in acceptance resulting from “turning on” radiative corrections (that is, going from MC with no radiative corrections to the nominal MC). The nominal MC sample is broken into subsamples based on whether an event was affected by the real or virtual corrections; 16.18% of generated events have a real radiated photon (that is, they are $\pi^0 \rightarrow e^+e^-\gamma\gamma$ events) and the remaining 83.82% have virtual corrections. The percent change in acceptance is given for each of these subsamples. | 110 |
| 6.5 | The fraction of events (and the error) whose SOD is more than 0.2 mm lower than the nominal value (6.35 mm). The last column gives the difference in this low-sod fraction between data and Monte Carlo for nominal MC, for MC with no accidentals, and for a combination of the two Monte Carlos. | 117 |

| | | |
|-----|--|-----|
| 6.6 | The fraction of events with no software clusters (and the uncertainty on this fraction). The last column gives the difference in this fraction between data and Monte Carlo for nominal MC, for MC with no accidentals, and for a combination of the two Monte Carlos. | 118 |
| 7.1 | The range of protons per spill corresponding to each of the three intensity ranges. | 141 |
| 7.2 | Number of events in data and Monte Carlo, and acceptances (with errors) for both modes, in the special low intensity runs and in the medium and high intensity ranges of the nominal set of runs. In the Dalitz mode, the acceptance has been corrected for the tracking inefficiency and for the relative trigger inefficiency, as described in the text. | 142 |
| 7.3 | The ratio of branching ratios in each intensity range as well as the error from both data and MC statistics. The nominal result is included for comparison. | 144 |
| 7.4 | A list of the run ranges and the average intensities of each of the eight subsamples used in the final intensity dependence cross check described in the text. | 147 |
| 8.1 | A summary of the previous measurements and theoretical prediction for the π^0 Dalitz decay branching ratio. | 157 |

CHAPTER 1

INTRODUCTION

1.1 Motivation for Studying $B(\pi^0 \rightarrow e^+e^-\gamma)/B(\pi^0 \rightarrow \gamma\gamma)$

Richard H. Dalitz first postulated the decay $\pi^0 \rightarrow e^+e^-\gamma$ in 1951 while thinking about the images cosmic rays produced on photographic plates. These images of large nuclear ‘stars’ (as they were called at the time) had allowed experimentalists to establish the existence of neutral π mesons. The decay $\pi^0 \rightarrow \gamma\gamma$ was confirmed by looking at the energies of electrons created when the photons converted in the plates; this method was also used to establish an upper limit on the lifetime of the π^0 . However, the lifetime measurement was limited by the fact that most ($\sim 97\%$) of the photons converted too far away from the nuclear ‘star’ for the resulting electrons to be identified. Dalitz realized that the interactions describing the two-photon decay process implied the existence of another decay mode, that of the π^0 into one real photon and one virtual photon, which would immediately internally convert to an electron-positron pair. Although he calculated the rate for this mode to be down by almost two orders of magnitude from $\pi^0 \rightarrow \gamma\gamma$, Dalitz suggested that identifying these decays would allow an improved π^0 lifetime measurement [1]. This decay, $\pi^0 \rightarrow e^+e^-\gamma$, was confirmed experimentally soon after the 1951 paper, and was dubbed the π^0 Dalitz decay.

The current world average for the measured π^0 Dalitz branching fraction has a large uncertainty (see Section 1.4). Since it is used experimentally as the normalization mode for measuring branching ratios of many rare pion and kaon decay modes, our relatively poor knowledge of the π^0 Dalitz branching ratio limits these measurements, since it must be taken as an external systematic error. A partial list of decay

modes where $\pi^0 \rightarrow e^+e^-\gamma$ has been used as a normalization mode (including cases where $K_L \rightarrow 3\pi^0 \rightarrow \gamma\gamma \gamma\gamma e^+e^-\gamma$ is the normalization mode) follows.

- $\pi^0 \rightarrow e^+e^-$
- $K_L \rightarrow e^+e^-\gamma$
- $K_L \rightarrow e^+e^-e^+e^-$
- $K_L \rightarrow \pi^+\pi^-\pi^0e^+e^-$
- $K_L \rightarrow \pi^0e^+e^-\gamma$
- $K_L \rightarrow \pi^0\pi^0\gamma$

Also, $\pi^0 \rightarrow e^+e^-\gamma$ is a source of leptons in hadronic environments, meaning knowledge of this process may be important in understanding background at the LHC since the Dalitz decay could fake exotic signatures. Finally, the measurement of $B(\pi^0 \rightarrow e^+e^-\gamma)/B(\pi^0 \rightarrow \gamma\gamma)$ has not been improved in 25 years. The quality of the KTeV detector and the accuracy of the simulation combined with the vast amount of data recorded during the experiment provide an opportunity to improve on previous measurements.

Before discussing our measurement of $B(\pi^0 \rightarrow e^+e^-\gamma)/B(\pi^0 \rightarrow \gamma\gamma)$ using KTeV data, it will be useful to have a basic understanding of the theoretical calculations of the decay rate as well as a general idea of experimental approaches used in past measurements. After a brief introduction to the neutral pion in Section 1.2, a review of the theoretical work on this subject is given in 1.3, and a description of previous experimental work is in Section 1.4.

1.2 The Neutral Pion: Properties and Decays

The neutral pion is a spinless pseudoscalar meson that was discovered by Jack Steinberger in 1950 [2, 3]. In the quark model, the neutral pion is composed of up and

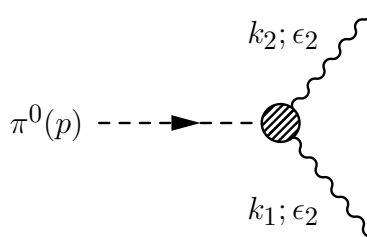


Figure 1.1: The Feynman diagram for the most common decay mode of the neutral pion, $\pi^0 \rightarrow \gamma\gamma$. k_1 and k_2 are the momenta of the photons; ϵ_1 and ϵ_2 are the polarizations.

down quarks:

$$\pi^0 = \frac{1}{\sqrt{2}} (u\bar{u} - d\bar{d}). \quad (1.1)$$

The π^0 decays electromagnetically, the dominant decay mode being $\pi^0 \rightarrow \gamma\gamma$ with a branching ratio of $(98.798 \pm 0.032)\%$ as of the 2006 listings of the Particle Data Group [4]. The next most common decay is the Dalitz decay, $\pi^0 \rightarrow e^+e^-\gamma$, which has a branching ratio of $(1.198 \pm 0.032)\%$. The Dalitz decay rate is usually reported as a fraction of the $\pi^0 \rightarrow \gamma\gamma$ rate, that is, $B(\pi^0 \rightarrow e^+e^-\gamma)/B(\pi^0 \rightarrow \gamma\gamma)$, which is $(1.213 \pm 0.033)\%$ currently [4].

Both decays proceed via the pion coupling to a quark loop, which can then emit real and/or virtual photons; the case where both are real photons is dominant, and is shown in Fig. 1.1. The Dalitz decay occurs when one of the photons is virtual (γ^*) and internally converts to an electron-positron pair directly at the point of the pion decay. The Dalitz decay is thereby distinguished from the conversion of a real photon in material (called external conversion), in which the e^+e^- pair is emitted away from the primary decay point after the photon has travelled some distance. The Dalitz decay is shown in Fig. 1.2.

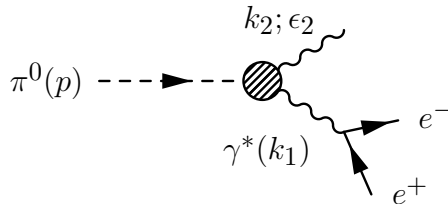


Figure 1.2: The Feynman diagram for the π^0 Dalitz decay, $\pi^0 \rightarrow e^+e^-\gamma$. The virtual photon, γ^* , immediately internally converts to the e^+e^- pair.

1.3 Theoretical Predictions

1.3.1 $B(\pi^0 \rightarrow \gamma\gamma)$ and the $\pi^0\gamma\gamma$ Form Factor

We begin with the decay $\pi^0 \rightarrow \gamma\gamma$ because it is so closely related to the Dalitz decay. If the pion were a point-like particle, its electromagnetic decay would be fully described by quantum electrodynamics (QED); however, because the pion has an internal quark structure, an electromagnetic transition form factor comes into the amplitude at the $\pi^0\gamma\gamma$ vertex [5]. (For a general review of form factors, see [6].) Since neutral pions cannot couple to a single photon due to charge conjugation invariance, the simplest electromagnetic vertex contains two photons, as given in the diagram for $\pi^0 \rightarrow \gamma\gamma$, shown in Fig. 1.1. The matrix element that describes this diagram is:

$$\left\langle \gamma(k_1, \epsilon_1), \gamma(k_2, \epsilon_2) | T | \pi^0(p) \right\rangle, \quad (1.2)$$

where (k_1, ϵ_1) and (k_2, ϵ_2) are the momenta and polarizations of the two photons, and p is the momentum of the pion. This matrix element can be rewritten as

$$\frac{F}{m_\pi} f \left(\frac{p^2}{m_\pi^2}, \frac{k_1^2}{m_\pi^2}, \frac{k_2^2}{m_\pi^2} \right) \times \epsilon_{\mu\nu\rho\sigma} \epsilon_1^\mu \epsilon_2^\nu k_1^\rho k_2^\sigma, \quad (1.3)$$

where F is a dimensionless constant, m_π is the mass of the π^0 , and $f\left(\frac{p^2}{m_\pi^2}, \frac{k_1^2}{m_\pi^2}, \frac{k_2^2}{m_\pi^2}\right)$ is the form factor of the π^0 . The case of two real photons ($k_1^2 = k_2^2 = 0$) is used to normalize the form factor:

$$f(1, 0, 0) = 1. \quad (1.4)$$

Together, Eq. 1.3 and Eq. 1.4 give

$$\Gamma_0 = \Gamma(\pi^0 \rightarrow \gamma\gamma) = \frac{m_\pi |F|^2}{64\pi}. \quad (1.5)$$

We can use this result to normalize the branching ratio of the Dalitz decay.

1.3.2 $B(\pi^0 \rightarrow e^+e^-\gamma)$ at Leading Order

For $\pi^0 \rightarrow e^+e^-\gamma$, one photon is real and one is virtual, so the $\pi^0\gamma\gamma$ form factor becomes $f\left(1, \frac{k_1^2}{m_\pi^2}, 0\right)$, which is sometimes shortened to $f\left(\frac{k_1^2}{m_\pi^2}\right)$. In the $m_e = 0$ limit, $k_1^2 = E_{\gamma^*}^2 - \vec{k}_1^2 \approx 4E_+E_- \sin^2(\theta/2)$ is the virtual photon mass squared. E_+ is the energy of the positron, E_- is the energy of the electron, and θ is the angle between the electron-positron pair. Note that the virtual photon mass squared is equivalent to the e^+e^- mass squared, and in the analysis, we will usually use the latter name to refer to this quantity.

We can write the $e^+e^- (\gamma^*)$ mass squared as a fraction of the π^0 mass squared:

$$x = \frac{k_1^2}{m_\pi^2}, \quad (1.6)$$

where

$$r = \frac{4m_e^2}{m_\pi^2} \leq x \leq 1 \quad (1.7)$$

is the range for x . For the decay to proceed, the virtual photon mass must be at

least twice the electron's rest mass (since we have an e^+e^- pair in the final state) and cannot be greater than the invariant mass of the π^0 , its parent particle. The differential rate for the π^0 Dalitz decay (per $\pi^0 \rightarrow \gamma\gamma$ event) is, in terms of x :

$$\frac{d\Gamma}{dx} = \left(\frac{d\Gamma}{dx}\right)_{QED} \times |f(x)|^2, \quad (1.8)$$

where (again, per $\pi^0 \rightarrow \gamma\gamma$ event)

$$\left(\frac{d\Gamma}{dx}\right)_{QED} = \frac{2\alpha}{3\pi} \frac{1}{x} (1-x)^3 \left(1 + \frac{r}{2x}\right) \left(1 - \frac{r}{x}\right)^{1/2}. \quad (1.9)$$

Given the current experimental precision, the form factor is usually represented as a function of a single parameter, a : $f(x) = (1 - ax)^{-1}$. Furthermore, for small a , we can use the linear approximation, $f(x) \approx (1 + ax)$, where a is the π^0 slope parameter [7]. The calculation of a is model-dependent, and has been done in several frameworks, including vector meson dominance, fermion loop models, and lattice QCD. Most models predict small values of a , in the range $0.02 - 0.04$ [8]. Note that the differential decay rate is strongly peaked at small x , while the effect of a is the greatest for large x . Therefore, for the commonly accepted range of a values, the form factor has a small ($\sim 0.2\%$) effect on the total (integrated) decay rate [9, 10].

The tree-level branching ratio, $B(\pi^0 \rightarrow e^+e^-\gamma)/B(\pi^0 \rightarrow \gamma\gamma)$, was first calculated in 1951 by Dalitz in the same paper in which he proposed the existence of the decay mode (hence the nomenclature – e^+e^- pairs from internal photon conversions are dubbed Dalitz pairs, and decays which involve these pairs are called Dalitz decays) [1]. He integrated $\left(\frac{d\Gamma}{dx}\right)_{QED}$ from Eq. 1.9, and found that internal conversion should occur with probability $\sim \frac{1}{160}$ for one photon, or $\sim \frac{1}{80}$ for either photon from the pion decay.

His result can be expressed as

$$\frac{\Gamma(\pi^0 \rightarrow e^+e^-\gamma)}{\Gamma(\pi^0 \rightarrow \gamma\gamma)} = \frac{\alpha}{\pi} \left\{ \frac{4}{3} \ln \frac{m_\pi}{m_e} - \frac{7}{3} + \frac{a}{3} + O\left(\left(\frac{m_e}{m_\pi}\right)^2\right) \right\}, \quad (1.10)$$

where the first two terms are from the QED calculation, the third involves the strong interaction parameter a (from the $\pi^0\gamma\gamma$ form factor), and the fourth is due to next-to-leading order (radiative) corrections as well as higher order terms in the form factor expansion. Numerically, the first two terms give the leading order (QED) result of $\frac{B(\pi^0 \rightarrow e^+e^-\gamma)}{B(\pi^0 \rightarrow \gamma\gamma)} = 1.185\%$.

In 1955, Kroll and Wada reproduced this leading order QED calculation and included predicted distributions of $B(\pi^0 \rightarrow e^+e^-\gamma)/B(\pi^0 \rightarrow \gamma\gamma)$ as a function of kinematic variables such as energy and angle [5]. They write the probability of $\pi^0 \rightarrow e^+e^-\gamma$ (normalized to $\pi^0 \rightarrow \gamma\gamma$) as a function of x and y , where x is essentially the same as in Eq. 1.6 and y is the energy partition between the electron and positron:

$$y = \frac{|E_+ - E_-|}{|\vec{q}_1 + \vec{q}_2|}. \quad (1.11)$$

We have denoted the electron and positron momentum vectors as \vec{q}_1 and \vec{q}_2 . The possible values of y are between 0 and 1. Note that in the e^+e^- rest frame, $y = -\beta \cos(\theta)$, where $\beta = \sqrt{1 - \frac{r^2}{x}}$ is the velocity of the electrons in this system and θ is the angle between the momentum of the positron and the pion. In this frame, the range for y is $-\beta \leq y \leq \beta$.

Kroll and Wada note that x is an invariant, and therefore independent of the motion of the π^0 , and y is essentially independent of the motion of the π^0 as long as the electron and positron are both highly relativistic and the angle between them is small. We can see that this is generally the case: If the virtual photon's momentum is

large compared to the electron mass, the energy of the intermediate state (containing the virtual photon) is very close to the energy of the final state. Because this scenario has a small energy denominator, it is favored, and the emitted pairs do tend to have small transverse momenta (and small angle between them) [5].

This tendency towards small angles between the electron and positron is an important point for this analysis, because it means that the electron and positron trajectories will be nearly parallel (until they are bent in the magnet between the drift chambers); therefore, the track separation in the first two drift chambers (before the magnet) will tend to be small. Accurately simulating the drift chamber inefficiency for close tracks is a challenge in the analysis, and will be discussed in several contexts later (see Sections 2.4 and 6.1, among others).

1.3.3 Radiative Corrections to $B(\pi^0 \rightarrow e^+e^-\gamma)$

The first computation of the electromagnetic radiative corrections (of order α relative to the leading order calculation) to $B(\pi^0 \rightarrow e^+e^-\gamma)/B(\pi^0 \rightarrow \gamma\gamma)$ was done in 1960 by Joseph as his thesis at the University of Chicago, working under Dalitz himself [11]. He numerically calculated those corrections that would contribute significantly at second order in α . The correction to the total rate was only about 1% of the leading order result:

$$\left(\frac{B(\pi^0 \rightarrow e^+e^-\gamma(\gamma))}{B(\pi^0 \rightarrow \gamma\gamma)} \right)_{rad} = 0.0105\%. \quad (1.12)$$

Combining this contribution from radiative corrections with the leading order result of 1.185%, Joseph's result for the total rate (at order α^2) is:

$$\frac{B(\pi^0 \rightarrow e^+e^-\gamma(\gamma))}{B(\pi^0 \rightarrow \gamma\gamma)} = 1.196\%. \quad (1.13)$$

The first semi-analytical calculation of radiative corrections was done in two related papers; the first was by Lautrup and Smith in 1971 [10] and the second was a follow-up paper by Mikaelian and Smith in 1972 [12]. In describing radiative corrections to the π^0 Dalitz branching ratio, we focus on these papers for two reasons. First, KTeV's Monte Carlo Dalitz decay generator was based on the 1972 paper which, in addition to giving an analytic calculation of radiative corrections to the total decay rate for the π^0 Dalitz decay, provides a table of numerical values for the radiative corrections to the differential decay rate. Second, although these authors calculate only those radiative corrections that are most significant at order α^2 , subsequent papers (such as [13] and [14]) have evaluated corrections neglected by these authors, and confirmed that they have a negligible effect on the total decay rate.

The main contributions to the lowest order radiative corrections to the tree-level diagram involve two types of corrections: virtual and real corrections. Virtual corrections arise from the interference of the lowest order diagram with the one-photon exchange diagrams (one-loop electromagnetic corrections to the virtual photon line and photon exchange between the electron and positron lines – see Fig. 1.3). Real corrections involve one of the electrons emitting a real photon (see Fig. 1.4). Both of these corrections are essentially independent of the hadronic structure of the pion, and hence computable in QED. Other corrections, which depend heavily on the pion structure, require a model of strong interactions and are difficult to compute. An example of this type of correction is that due to the interference of one-photon and two-photon exchange diagrams (essentially $\pi^0 \rightarrow e^+e^-$ with bremsstrahlung). Because the two-photon exchange diagrams have a virtual loop involving two off-mass-shell photons, they require a model of the pion form factor for k_1^2 and k_2^2 both nonzero. Fortunately, this contribution is not significant except possibly at high e^+e^- -mass, where the overall rate is suppressed. Lautrup and Smith drew on the work of Brown [15] to

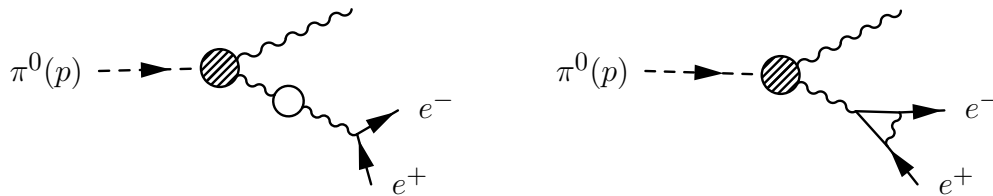


Figure 1.3: The Feynman diagrams for the virtual corrections to π^0 Dalitz decay, $\pi^0 \rightarrow e^+e^-\gamma$. The left diagram represents an electromagnetic loop correction to the virtual photon line, and the right diagram shows photon exchange between the e^+ and e^- lines.

justify neglecting this contribution.

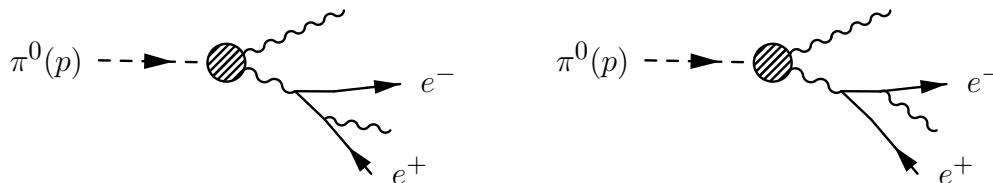


Figure 1.4: The Feynman diagrams for the real (bremsstrahlung) corrections to π^0 Dalitz decay, $\pi^0 \rightarrow e^+e^-\gamma$. Each of these counts twice, since there are two other identical diagrams with the radiative and decay photons interchanged.

Theorists debated the importance of the two-photon exchange diagrams to the radiative corrections during the 1980s [8, 9]. Lambin and Pestieau claimed they are suppressed by a factor of $\frac{m_e^2}{m_\pi^2}$ [16], but this was disputed by Tupper, et al. [17] and also by Beder, whose approximate calculations suggested these contributions are completely negligible [18]. In any case, these contributions can only be important for relatively large values of the e^+e^- -mass ($x \geq 0.6$), where we have very few events in this analysis ($\sim 1\%$ of our data).

Lautrup and Smith analytically compute the radiative corrections to the total rate at second order in α in the 1971 paper to obtain a correction of 1.05×10^{-4} , in agreement with Joseph's previous numerical calculation. This gives the total result, including electromagnetic corrections, in Eq. 1.13. The lowest order differential decay

rate,

$$\frac{1}{\Gamma_0} \frac{d^2\Gamma(\pi^0 \rightarrow e^+e^-\gamma)}{dxdy} = \frac{\alpha}{\pi} |f(1, x, 0)|^2 \frac{(1-x)^3}{4x} \left(1 + y^2 + \frac{r^2}{x}\right) \quad (1.14)$$

is also computed. To evaluate the radiative corrections to the differential decay rate, the authors write

$$\frac{d^2\Gamma^{rad}}{dxdy} = \delta(x, y) \frac{d^2\Gamma}{dxdy}, \quad (1.15)$$

where $\delta(x, y) = \delta_{virtual} + \delta_{real}$. In the calculation of the real corrections, δ_{real} , they use the soft-photon limit, in which a maximum energy is imposed on the radiated photon. This result cannot be used for small values of x , and therefore, they cannot integrate their result over x to find the total corrected decay rate. It is clear that using the soft-photon limit is not acceptable because the corrections they obtain are negative for all values of x , but the total correction to the rate is known to be positive (recall Eq. 1.12). To get the correct result, they know they must do the calculation for all radiated photon energies, thus making their evaluation of radiative corrections to the differential decay rate valid over the entire x range.

The work of Mikaelian and Smith in the 1972 paper does just this [12]. They rework the calculations with no restriction on the radiated photon energies and find that the corrections are small and positive for low x and large and negative for high x ; since most of the events are at low x , the small positive correction in that region has a significant impact on the overall correction. Integrating their result yields a correction to the total rate of 0.95×10^{-4} . The slight disagreement with the previous result of 1.05×10^{-4} is due to the numerical inaccuracy of computing a three-dimensional integral which is badly behaved for small x .

The main result of the Mikaelian and Smith paper that is important for this

analysis is a table giving the numerical values of the radiative corrections $\delta(x, y)$ for x and y values over the whole kinematic range for each variable. The calculations used to produce this table were repeated to produce a very finely binned (in x and y) table of corrections for generating the π^0 Dalitz decay in the KTeV Monte Carlo. The Monte Carlo will be discussed in Chapter 4, with the mechanics of the Dalitz decay event generation described in Section 4.9.2.

Recently, a group of theorists has revisited the radiative corrections to the π^0 Dalitz decay [13, 14]. They have done some of the previously neglected calculations that depend on the pion structure using Chiral Perturbation Theory. They compute the contributions from two-photon exchange diagrams (which are corrections to $B(\pi^0 \rightarrow e^+e^-\gamma)/B(\pi^0 \rightarrow \gamma\gamma)$ at order α^2 , but which had been assumed to be negligible because they are proportional to $\frac{m_e^2}{m_\pi^2}$) as well as corrections of order α^4 . They find these contributions do have some impact on the corrections to the differential decay rate, but are only significant at large x , as expected. Significantly, they find that the impact on the total rate is negligible, and they agree with the previous results (Eq. 1.13) for the corrected decay rate.

1.4 Previous Measurements of $B(\pi^0 \rightarrow e^+e^-\gamma)/B(\pi^0 \rightarrow \gamma\gamma)$

The 2006 PDG average for the π^0 Dalitz branching fraction is $\frac{B(\pi^0 \rightarrow e^+e^-\gamma)}{B(\pi^0 \rightarrow \gamma\gamma)} = (1.213 \pm 0.030)\%$. It has a 2.5% uncertainty, and it is based on three measurements, the most recent of which is 25 years old. The PDG listing [4] of these measurements follows.

- $(1.25 \pm .04)\%$ Schardt 1981, $\pi^-p \rightarrow n\pi^0$ [19]
- $(1.166 \pm .047)\%$ Samios 1961, 3071 events, $\pi^-p \rightarrow n\pi^0$ [20]

- $(1.17 \pm .15)\%$ Budagov 1960, 27 events [21]

The earliest measurements of the Dalitz decay were done using π^- beams and hydrogen targets. The two most probable reactions in this set-up are:

$$\pi^- p \rightarrow n\pi^0 \rightarrow n\gamma\gamma \quad (1.16)$$

$$\pi^- p \rightarrow n\gamma \quad (1.17)$$

After Dalitz's observation that, in addition to $\pi^0 \rightarrow \gamma\gamma$, the decay $\pi^0 \rightarrow e^+e^-\gamma$ was also possible, the process in Eq. 1.16 could be used to look for that new decay [20]. First observations of a few events came in emulsions [22, 23, 24] and then via counter techniques where a γ and an electron were detected in coincidence [25]. Following that, two cloud chamber experiments yielded around 30 events each [21, 26]. One of these is the Budagov measurement in the PDG listing. Although it had only 27 events (and, therefore, large uncertainties), this result was significant because it showed general agreement with the angular and energy distributions predicted by Kroll and Wada (see Section 1.3.2). In particular, Budagov found an x distribution peaked at small values of e^+e^- mass (corresponding to small angles between the electron and positron) and a y distribution that showed a flat energy partition between the electron and positron [21], both as predicted.

Experimental advances came with the advent of the hydrogen bubble chamber. In 1961, Samios was able to gain a factor of 100 in event statistics using a negative pion beam and a hydrogen bubble chamber, allowing more meaningful comparison with predictions. The experimental result was $\frac{B(\pi^0 \rightarrow e^+e^-\gamma)}{B(\pi^0 \rightarrow \gamma\gamma)} = (1.166 \pm 0.047)\%$, in agreement with the predicted value of 1.196%. The angular and energy distributions also coincided with theoretical predictions.

It was 20 years before another dedicated measurement of $\frac{B(\pi^0 \rightarrow e^+e^-\gamma)}{B(\pi^0 \rightarrow \gamma\gamma)}$ was made by Schardt [19]. The $\pi^- p \rightarrow n\pi^0$ reaction was again used; this time, a π^- beam and a CH_2 target were used with a shower counter and a magnetic spectrometer, where coincidences of a photon and an e^+e^- pair were required. To generate Dalitz decays, the Monte Carlo used the same calculations of electromagnetic radiative corrections that the KTeV Monte Carlo uses (based on the 1971 Lautrup and Smith paper and the 1972 Mikaelian and Smith paper, both described in Section 1.3.3). The Schardt result of $\frac{B(\pi^0 \rightarrow e^+e^-\gamma)}{B(\pi^0 \rightarrow \gamma\gamma)} = (1.25 \pm 0.04 \pm 0.01)\%$ was limited by statistics.

In the analysis of KTeV data, we find 63,693 $K_L \rightarrow 3\pi_D^0$ decays in KTeV data (a gain of a factor of ~ 20 in event statistics over the last experiments), and normalize to $K_L \rightarrow 3\pi^0$ (of which we find 3,529,065), to extract $\frac{B(\pi^0 \rightarrow e^+e^-\gamma)}{B(\pi^0 \rightarrow \gamma\gamma)} = (1.1559 \pm 0.0046 \pm 0.0107)\%$. The statistical error is 0.40% and the systematic error is 0.93%, giving a total relative uncertainty of 1.01%.

1.5 Overview of this Dissertation

We have now discussed the motivation for studying the π^0 Dalitz decay, as well as the previous results from both theory and experiment. In the rest of this dissertation, we will give a new result for this decay mode based on data from the KTeV experiment. The next chapter describes KTeV's experimental technique and its detectors, with emphasis on those components most important for this analysis. Chapter 3 gives an overview of the measurement technique, discusses the data samples used, and explains the analysis and event selection criteria. The measurement technique relies on a detailed simulation of the detector; this Monte Carlo simulation is the subject of Chapter 4. Next, we will give the results of the analysis and simulations in Chapter 5, followed by a discussion of the systematic uncertainties on the mea-

surement in Chapter 6. We performed several cross-checks to test our result; these are described in Chapter 7. Finally, we discuss the importance of this new result and other measurements that are affected by it in Chapter 8.

Throughout the remainder of this document, the intention is not only to make the analysis conceptually clear to a broad audience of physicists, but also to include enough specific details to enable someone familiar with KTeV to understand how the analysis was actually carried out. This means that KTeV jargon and variable names from KTeV analysis code have been included in some places, along with descriptions of what the terms mean. It is the author's hope that this will help those interested in the details of the analysis without distracting or confusing the more casual reader.

CHAPTER 2

THE KTeV DETECTOR

This measurement of $B(\pi^0 \rightarrow e^+e^-\gamma)/B(\pi^0 \rightarrow \gamma\gamma)$ uses data from the KTeV experiment at Fermi National Accelerator Laboratory (FNAL) in Batavia, Illinois. A fixed-target experiment at the Tevatron, KTeV has two distinct operational modes which use slightly different hardware and software: E799 searches for CP-violating rare decays of the K_L , while E832 was designed to measure the direct CP violation parameter, $\text{Re}(\epsilon'/\epsilon)$ [27]. Data-taking periods for these two experiments were interleaved, and took place during 1996, 1997, and 1999.

2.1 Overview of the Detector

For the $\text{Re}(\epsilon'/\epsilon)$ analysis, which was the focus of E832, the experiment was designed to produce two K_L beams, one of which went through a regenerator (it was called the regenerator beam to distinguish it from the other beam, called the vacuum beam) to create a beam of particles in linear superposition of K_L and K_S . (In contrast, in the E799 configuration, there is no regenerator, and, therefore, both beams are vacuum beams.)

In addition to measuring $\text{Re}(\epsilon'/\epsilon)$, the KTeV experiment produced many pions as intermediate decay products of the kaons. In particular for this analysis, the vacuum beam is a source of neutral pions, since it is composed of K_L particles, about 19.6% of which decay to three π^0 s [4]. We study this sample of $3\pi^0$ events to measure $B(K_L \rightarrow 3\pi^0 \rightarrow \gamma\gamma \gamma\gamma e^+e^-\gamma)/B(K_L \rightarrow 3\pi^0 \rightarrow \gamma\gamma \gamma\gamma \gamma\gamma)$, which leads directly to a measurement of $B(\pi^0 \rightarrow e^+e^-\gamma)/B(\pi^0 \rightarrow \gamma\gamma)$ after taking into account the different detector efficiencies in each mode and the factor of 3 from the presence of three neutral pions (as explained in Section 5.3). This analysis uses 1999 data from

the E832 configuration, as this is the only configuration and data-taking period which had a suitable trigger and enough statistics for this measurement.

The signal mode (the Dalitz decay) is detected by observing two charged tracks in the spectrometer (four drift chambers and a dipole magnet) and seven electromagnetic clusters in the Cesium Iodide calorimeter (CsI). The normalization mode is detected by observing six photons in the calorimeter. A veto and trigger system help to discriminate these events from other kaon and pion decays.

Several aspects of the KTeV detector are instrumental for making a precision measurement of the Dalitz decay branching ratio. Energies and momenta of electromagnetic particles are measured at the sub-percent level, allowing excellent event reconstruction. The total amount of material upstream of the calorimeter is approximately 4% of a radiation length, reducing particle interactions. The electron and positron in the decay are easily identified due to being separated by a magnet. Finally, years of experience and effort to understand the detector and to create a very accurate simulation make it possible to use data from the KTeV experiment to improve on previous measurements of the Dalitz decay branching ratio.

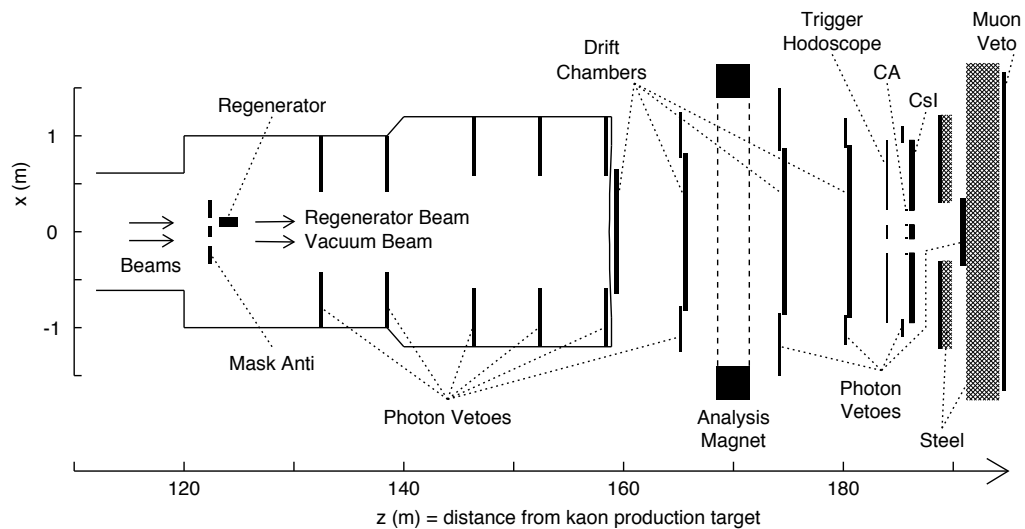


Figure 2.1: The KTeV detector in the E832 configuration, viewed from above.

The E832 configuration of the KTeV detector, shown in Fig. 2.1, has been described in detail in many places [27, 28, 29]; here, we will give a general description of the experimental setup and each detector component, with emphasis on those that are most important for this analysis, while referring the interested reader to other papers and theses for further information where appropriate.

2.2 Beamline and Target

KTeV is a fixed-target experiment located at Fermi National Accelerator Laboratory (FNAL). The FNAL Tevatron’s 800 GeV/ c proton beam is incident on a Beryllium Oxide (BeO) target. The beam operates on a cycle approximately one minute and 20 seconds long, consisting of about 40 seconds when protons are injected and accelerated and about 40 seconds when the accelerated protons are delivered to the target. Protons arrive at the target in 1-2 ns-wide pulses in an “RF-bucket” of 19 ns. During each ~ 40 second “spill”, up to 7×10^{12} protons are delivered. (This is in contrast to the one minute-long beam cycle during the 1997 data-taking periods, in which the spills were ~ 20 seconds.)

The rod-shaped target is 30 cm long (approximately one proton interaction length), and 3×3 mm² in the dimensions transverse to the beam. The RMS size of the beam spot on the target (in the $x - y$ dimensions) is about 250 μm [30]. In order to strike a balance between maximizing the kaon flux and minimizing the neutron to kaon ratio, the proton beam is incident on the target at a downward angle of 4.8 mrad with respect to the line between the target and the center of the detector [27].

2.2.1 *Experimental Coordinate System*

The center of the BeO target is the origin of the KTeV coordinate system. The line from the target to the center of the detector is the positive z -axis, the positive y -axis is up, and the coordinate system is right-handed.

2.2.2 *Purifying and Collimating the Beams*

The beamline is approximately 100 meters long, allowing purification and collimation of the two kaon beams. Other hadrons, muons, neutrons, and photons, along with the remains of the primary proton beam, are removed with a combination of sweeping magnets and lead and beryllium absorbers. For each beam, there is a 1.5 meter long primary collimator at $z = 20$ m and a 3 meter long defining collimator at $z = 85$ m. Each collimator's two square holes are tapered to reduce scattering. Additionally, there is a crossover absorber at $z = 40$ m to prevent kaons that do scatter from crossing into the other beam. The locations of the absorbers and collimators are shown in Fig. 2.2.

After passing through the collimators, the beams contain mostly neutrons and kaons (in a 1.3:1.0 ratio), along with a small contamination (at a level several orders of magnitude smaller than the level of kaons and neutrons) of other neutral particles such as photons, neutral hadrons, cascades, and lambdas. Most of the neutrons do not interact within the detector due to their long lifetimes. The beams pass through holes in the mask anti veto (MA), which is just upstream of the regenerator (see Fig. 2.2). The veto system, including the MA, will be discussed in more detail in Section 2.6.

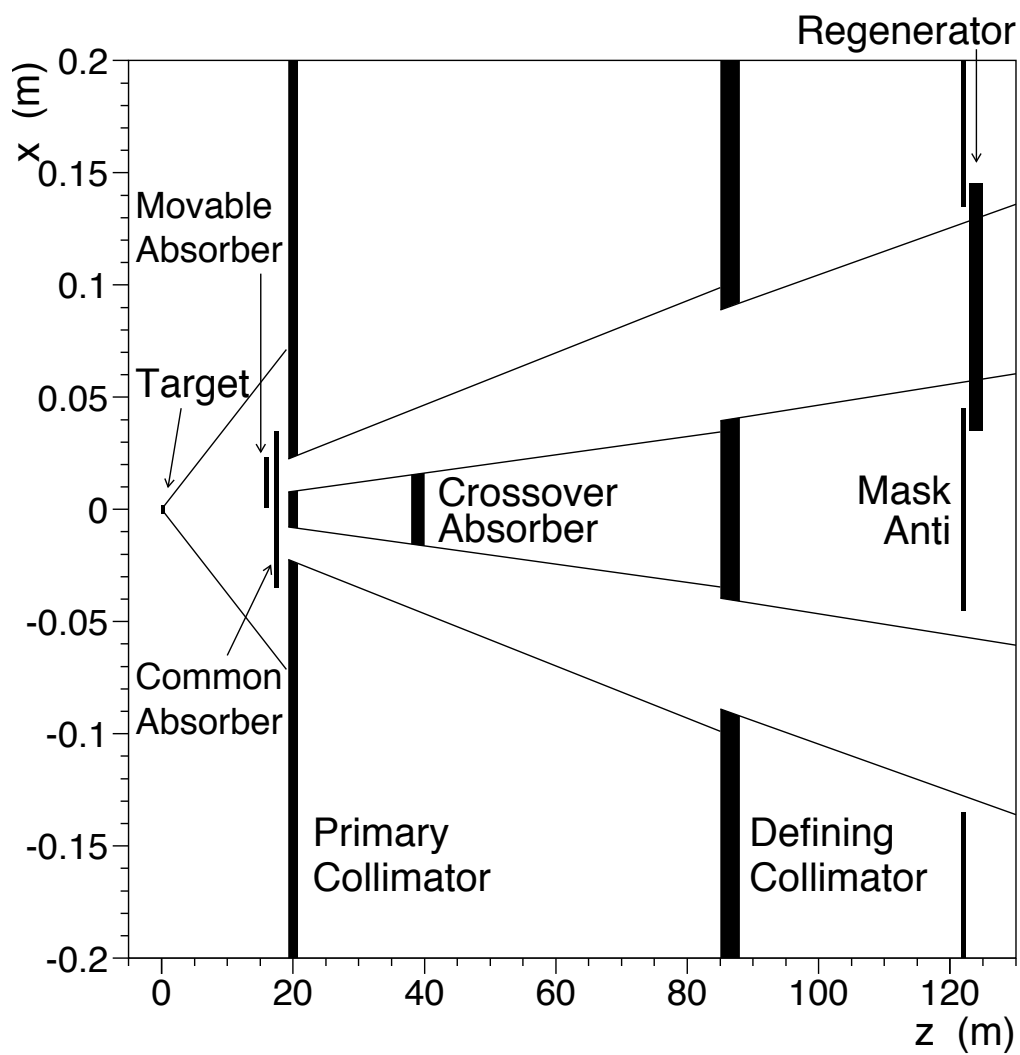


Figure 2.2: The KTeV beamline, as viewed from above. The target is located at $z = 0$.

2.2.3 Accidental Counters

A set of counters are used to trigger on primary beam activity uncorrelated with activity in the detector. (For a discussion of the trigger system, see Section 2.7.) This accidental activity is recorded during data-taking and is later used in the Monte Carlo to create a realistic simulation of underlying detector activity. The main set of accidental counters are three counters that make up the 90° target monitor, so-called due to their right-angle orientation with the primary beam at a small hole in the target pile.

2.3 Decay Region: Vacuum and Regenerator Beams

There is an evacuated region from $z = 28$ m to $z = 159$ m, held at 10^{-6} Torr, through which the beams travel. The vacuum reduces interactions between the neutral beams and surrounding matter to a negligible level, and suppresses the scattering of charged decay products. The detector reconstructs decays downstream of the defining collimator (at $z = 85$ m). A vacuum pipe surrounding the evacuated volume increases in diameter to 243.84 cm at the vacuum window, which seals the vacuum region at $z = 159$ m. The window is made of kevlar and mylar and is 0.14% radiation lengths [27]. The window is 7.6 mm thick, supports a force of 222 kN, and deflects by almost 15 cm at its center under this force [28].

Although the regenerator beam is not used as a source of physics in this analysis, the regenerator is used to determine the energy scale to apply to the data. This will be described in Section 3.5.4. The regenerator is the source of K_S particles in the $\text{Re}(\epsilon'/\epsilon)$ analysis, via coherent conversion of K_L particles to K_S particles. The regenerator is composed of 84 scintillator modules, as shown in Fig. 2.3, and is located from about $z = 123.8$ m to $z = 125.5$ m. To reduce systematic biases in the $\text{Re}(\epsilon'/\epsilon)$

analysis, the regenerator was moved from one beam to the other every few minutes during data-taking. This means that each event must be identified in the analysis as coming from the vacuum or regenerator beam based on event reconstruction.

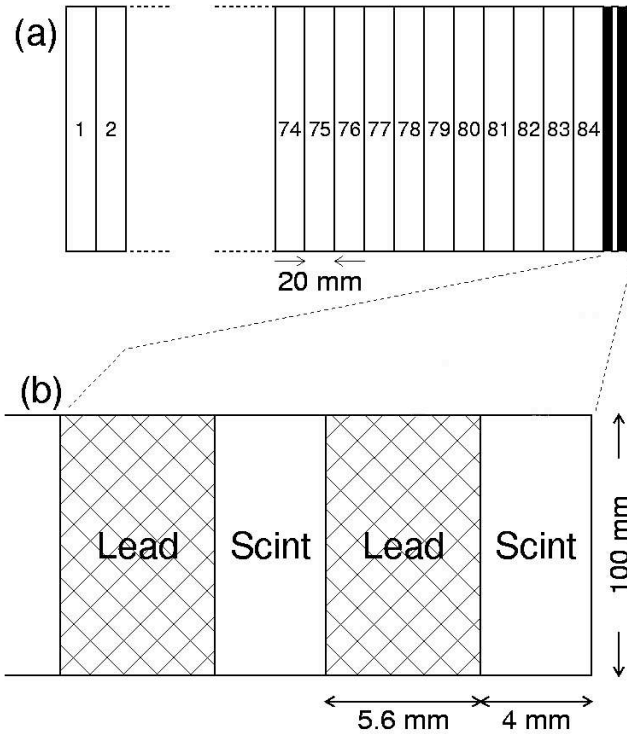


Figure 2.3: (a) Diagram of the regenerator, and (b) detailed view of the downstream end of the regenerator. The kaon beam enters from the left.

To reduce interactions from the neutral beams and to reduce multiple scattering and photon conversions of decay products, Helium fills the space between detector components downstream of the vacuum window ($z = 159$ m). Additionally, there is very little material (4% of a radiation length) between the vacuum window and the calorimeter, most of which (60%) is in the trigger hodoscope (see Section 2.7.1) and 10% of which is upstream of the first drift chamber [27].

2.4 Spectrometer

The spectrometer consists of four drift chambers (DCs); one pair is downstream of a dipole magnet and the other pair is upstream of the magnet. The drift chambers measure the x and y positions of the charged particles, and, by bending the charged particle trajectories, the magnet allows us to determine the momentum of the particle using the x and y slopes of the trajectories in both pairs of drift chambers. The z positions (distance from the target) of the spectrometer components are given in Table 2.1.

| Chamber | Distance from target (m) |
|---------|--------------------------|
| DC1 | 159.44 |
| DC2 | 165.59 |
| magnet | 170.00 |
| DC3 | 174.61 |
| DC4 | 180.51 |

Table 2.1: z -positions of the midplanes of the four drift chambers and the analysis magnet.

2.4.1 Analysis Magnet

The analysis magnet between the upstream and downstream pairs of drift chambers (at $z = 170$ m) is a dipole magnet with a 3×2 m² aperture and a current of 1600 A [30]. While the experiment was running, the field produced was uniform to better than 1%, and provided a 0.41 GeV/ c momentum kick in the horizontal plane. Even the small deviations in the field uniformity were studied and mapped, so that the momentum of tracks traversing the field at different locations could be precisely determined. The magnet polarity was reversed every 1-2 days during data-taking runs to reduce systematic biases relating to the field orientation [27]. We return to this point briefly as part of our cross-checks in Section 7.6.

The field falls from a maximum field of 3000 Gauss to 60 Gauss at the location of DC2 (4.4 m from the center of the magnet). This “fringe field” extending past DC2 and DC3 slightly displaces the hit positions in these chambers. The magnitude of the fringe field is measured using data, and a correction is applied in the tracking algorithm (described in Section 3.4.1) to obtain the correct hit positions.

2.4.2 Drift Chambers

Each drift chamber is composed of four planes of sense wires. There are two planes with horizontal wires to measure y hit positions (called the y -view) and two planes with vertical wires to measure x hit positions (called the x -view). Interleaved between layers of sense wires are layers of field-shaping wires. There are also field wires at each drift chamber window so that the sense plane nearest the window is fully surrounded by field wires.

The $x - y$ size of the drift chambers increases as one goes downstream; DC1 is $1.26 \times 1.26 \text{ m}^2$ in the transverse dimensions, while DC4 is $1.77 \times 1.77 \text{ m}^2$. The number of sense wires increases with the size of the chambers. DC1 has 101 sense wires per plane, while DC4 has 140 sense wires per plane [27].

Each plane has a hexagonal cell geometry resulting from the six field-shaping wires that surround each sense wire. Shown in Fig. 2.4, each cell is 6.35 mm wide and the drift velocity is about $50 \text{ } \mu\text{m}/\text{ns}$ in the equal parts argon-ethane gas. The “in-time” window is 150 ns, corresponding to the maximum drift time across a cell [27]. The two planes of sense wires in each view (x and y) are offset from each other by half a cell to resolve the left-right ambiguity. In order to reconstruct tracks, the x and y hit positions in the four chambers must be combined with energy and position information from the calorimeter.

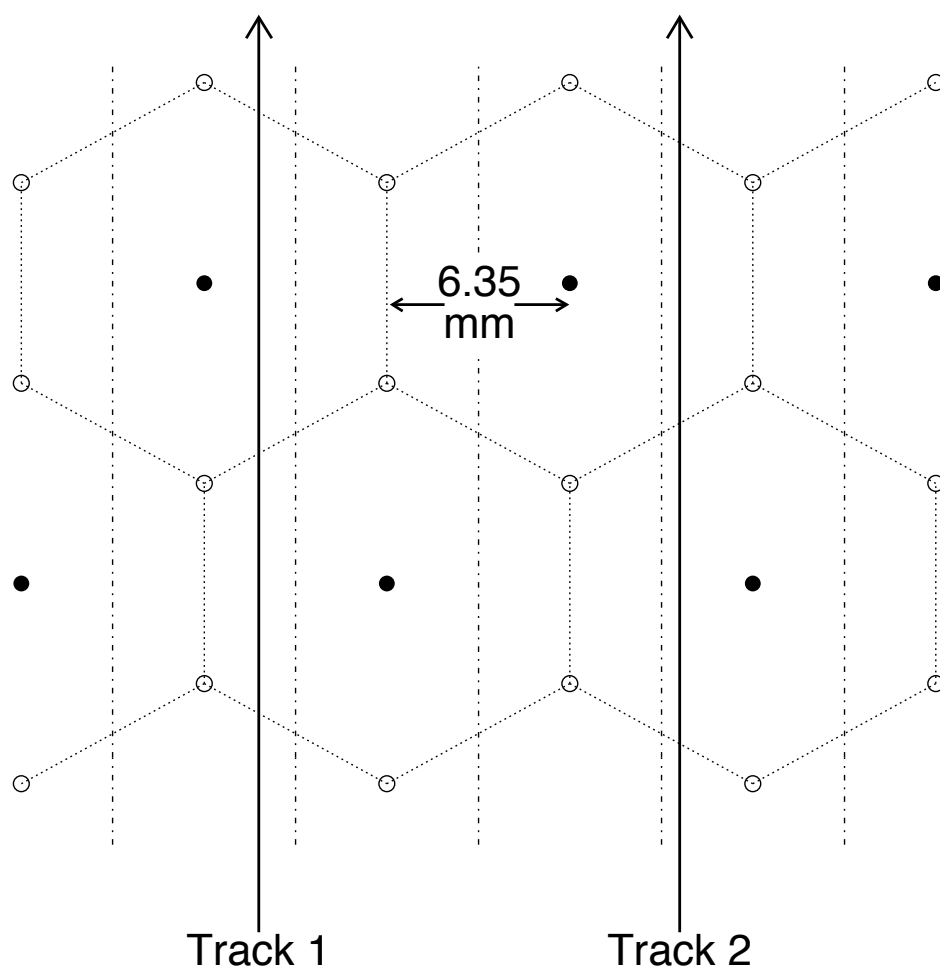


Figure 2.4: The drift chamber cells are formed by the six field wires (open circles) around each sense wire (black dots). The vertical dashed lines are the boundaries of the off-set cells, formed by the other plane in the same view.

When a charged particle goes through a drift chamber, it ionizes atoms in the gas mixture. The resulting electrons are accelerated by the electric field toward the anode sense wires. As the ionization electrons gain energy, they ionize more and more gas atoms, eventually creating an avalanche. When this avalanche of electrons reaches a sense wire, it creates a current, as shown in Fig. 2.5. The wire-positions and timing of these “hits” can be used to reconstruct the charged particle’s track. The hits in the two x planes (or two y planes) are called a “hit-pair.” For a track that is perpendicular to the drift chamber, perfect resolution would mean that the sum of drift distances (SOD) from each hit pair should be exactly the width of a cell (6.35 mm). An angular correction is applied for tracks that are not perpendicular to the chamber. To be used in the track reconstruction, a hit-pair must have a SOD within 1 mm of the cell width. The SOD resolution is $150\ \mu\text{m}$, resulting in a typical single-hit position resolution of $110\ \mu\text{m}$ and a hit-pair resolution of $80\ \mu\text{m}$ [27]. The track reconstruction algorithm will be described in more detail in Section 3.4.1, and the tracking inefficiency will be discussed in Section 6.1.

Lecroy 3373 multi-hit time-to-digital converters (TDCs) measure the drift times relative to the Level 1 trigger (see Section 2.7.2). The TDC time window is 2.5 times longer than the in-time window and is centered around the in-time window. For track reconstruction, only the earliest in-time hit on each wire is used, although hits before the in-time window are recorded as early hits. Note that the TDC resolution is 0.25 ns, resulting in a $13\ \mu\text{m}$ contribution to the position resolution [27].

Calibration of the drift chambers is a complex process. It is described in summary here, with much more detail available in [28]. First, raw hit-times in a given plane are aligned by determining a timing offset for each wire. Then, $x(t)$ maps are used to convert each drift time, t , into a drift distance, x . The time to distance calibration is measured for each of the 16 planes using the assumption that the tracks uniformly

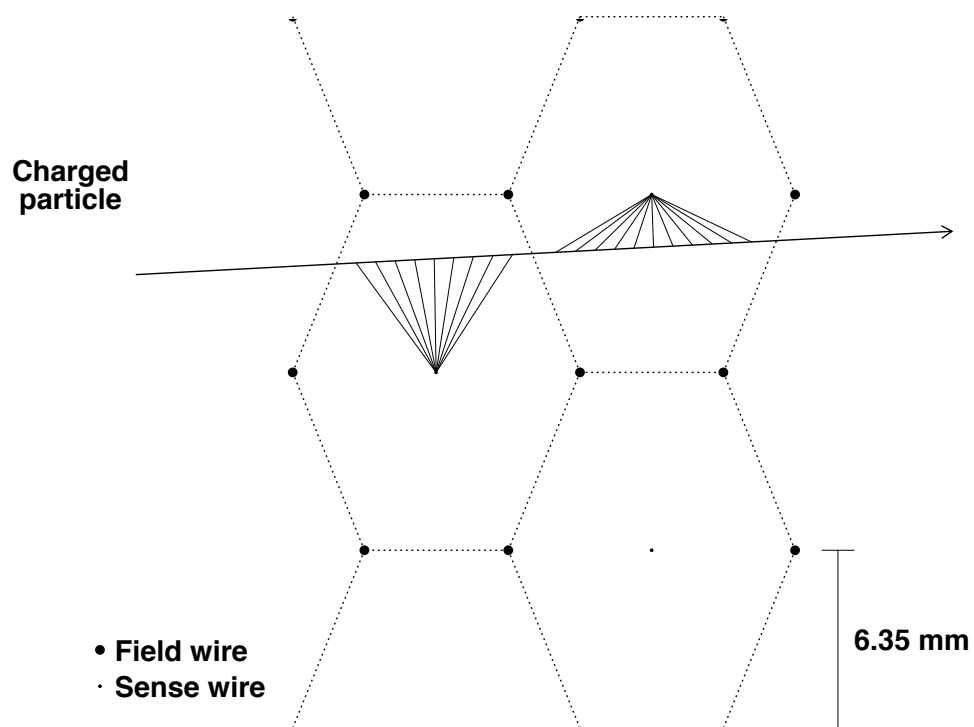


Figure 2.5: A typical charged particle track through a drift chamber. The thin lines are the drift paths of the ionization electrons towards the sense wires.

illuminate each cell. This method assumes that the earliest TDC hits come from positions closest to the sense wire, that the latest TDC hits come from positions at the edge of the cell, and that larger times correspond to larger distances. The $x(t)$ calibrations were performed every 1-2 days, when the magnet polarity was being reversed.

The position of each drift chamber relative to everything else in the experimental setup is very important for accurate reconstruction of tracks. DC alignment measurements were made every 1-2 days, when the magnet polarity was being reversed, using dedicated high-intensity muon runs with no magnetic field. The transverse position of the target relative to the drift chambers is found using $K \rightarrow \pi^+\pi^-$ decays in the vacuum beam; the reconstructed kaon trajectory is projected back to the target. Measurement of the CsI position relative to the drift chambers uses $K_L \rightarrow \pi^\pm e^\mp \nu$ decays [27].

After all calibration and alignment, the drift chambers measure x and y positions with a resolution of about $110 \mu\text{m}$ and track momentum with a resolution of 0.4% at $36 \text{ GeV}/c$.

2.5 The CsI Calorimeter

The electromagnetic calorimeter is used to measure energies and positions of electromagnetic decay products. For the $\text{Re}(\epsilon'/\epsilon)$ measurement, the calorimeter needed to have excellent energy resolution and linearity as well as good position resolution and fast signals. It also needed to be able to stand up to fairly high doses of radiation without serious degradation. Because scintillating crystals met all of these requirements, they were chosen for the calorimeter, despite several drawbacks. The crystals are susceptible to bending and scratching and require a dry environment for

handling and storage. Careful handling and specially built dehumidified rooms were the solutions to these issues.

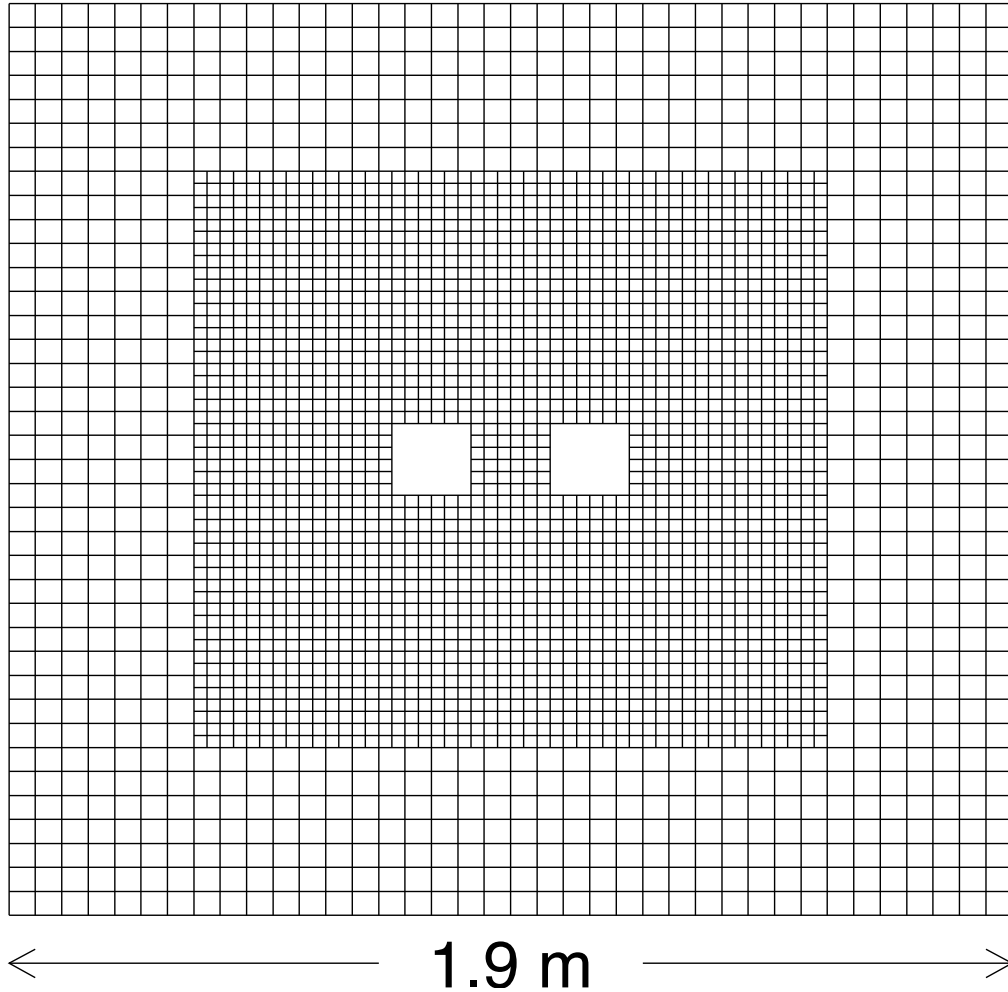


Figure 2.6: Transverse view of the CsI calorimeter. There are 868 $5.0 \times 5.0 \text{ cm}^2$ outer crystals and 2232 $2.5 \times 2.5 \text{ cm}^2$ inner crystals. The beam holes are $15 \times 15 \text{ cm}^2$ each and are 30 cm apart from center to center.

As seen in Fig. 2.6, the calorimeter is composed of 3100 pure Cesium Iodide (CsI) crystals (also called blocks). In overall dimensions, it is $1.9 \times 1.9 \text{ m}^2$ by 50 cm deep. The 868 outer crystals are each $5.0 \times 5.0 \text{ cm}^2$, and are each viewed by a 3.8 cm Hamamatsu R5330 photomultiplier tube (PMT). The 2232 inner crystals

are each $2.5 \times 2.5 \text{ cm}^2$, and are each viewed by a 1.9 cm Hamamatsu R5364 PMT. The smaller crystals allow for finer position resolution in the central region of the calorimeter where most of the interactions take place. Each crystal is 50 cm long; this corresponds to 27 radiation lengths for electromagnetic particles – therefore, the energy from photons and electrons is virtually entirely contained in the calorimeter. The calorimeter’s better than 1% electromagnetic energy resolution was attained by individually wrapping, testing, and calibrating (see Section 2.5.2) each crystal for longitudinal uniformity. Two square holes made of carbon fiber allow the neutral beams to go through the calorimeter without hitting any material. Each beam hole is $15 \times 15 \text{ cm}^2$. For more information about the properties and characteristics of the calorimeter, see [28].

2.5.1 Digitization

A Schott UV filter between each crystal and its PMT picks out the fast component of the scintillation light; this results in an average light yield of 20 photo-electrons per MeV of energy deposited [27]. Behind the PMTs are digitizers (DPMTs) which integrate the charge from the PMT: the PMT anode is connected by a very short cable to a circuit which digitizes the signal, stores the digitized value, and transmits the signal on demand. Each DPMT records the charge from its PMT in several time slices, providing information about the time profile of the energy deposit in the crystal. Each time slice is equal to three buckets, and the first time slice includes the in-time bucket [30]. For more specifics on these DPMTs, see [31]. The digitizers, which were able to measure energies from a few MeV to 100 GeV, were located directly behind the PMTs to reduce electronic noise to less than 1 MeV.

2.5.2 Energy Calibration

Calibration is required to convert the integrated charge measured by the DPMTs to an energy measurement. First, the DPMT response to its PMT was calibrated with a laser. Laser scans were done approximately once a week throughout data-taking; they revealed deviations from a linear fit of the combined DPMT and PMT response versus light level of less than 0.1% (rms) for each channel. Additionally, the laser was used at 1 Hz at fixed intensity while data was being taken to correct for short-term gain drifts, typically of less than 0.2% per day [27].

Second, the electrons from $K_L \rightarrow \pi^\pm e^\mp \nu$ decays were used to calibrate the energy scale of each channel (that is, to determine the conversion from DPMT counts to energy). Because the electrons are highly relativistic, we expect the ratio of their energy to their momentum (E/p) to be peaked at 1. The momentum measurement is made by the spectrometer; the energy measurement is made by converting the DPMT signals into energies using a rough set of energy calibration constants. The calibration constants are refined offline in several iterations so that the E/p distribution is centered at 1. Figure 2.7 shows this distribution after calibration. Figure 2.8 shows the energy resolution of the calorimeter after subtracting out the momentum resolution (from the drift chambers).

The energy measurements are made using “clusters” of crystals centered on the crystal with the maximum energy (the “seed block”): a cluster is a 3×3 group of large crystals or a 7×7 group of small crystals. The energy is corrected for the shower leakage outside the cluster crystals, leakage at the beam holes and calorimeter edges, and for channels with energies below the 4 MeV readout threshold [27]. The clustering algorithm and corrections to the energy measurement will be described in more detail in Section 3.4.2.

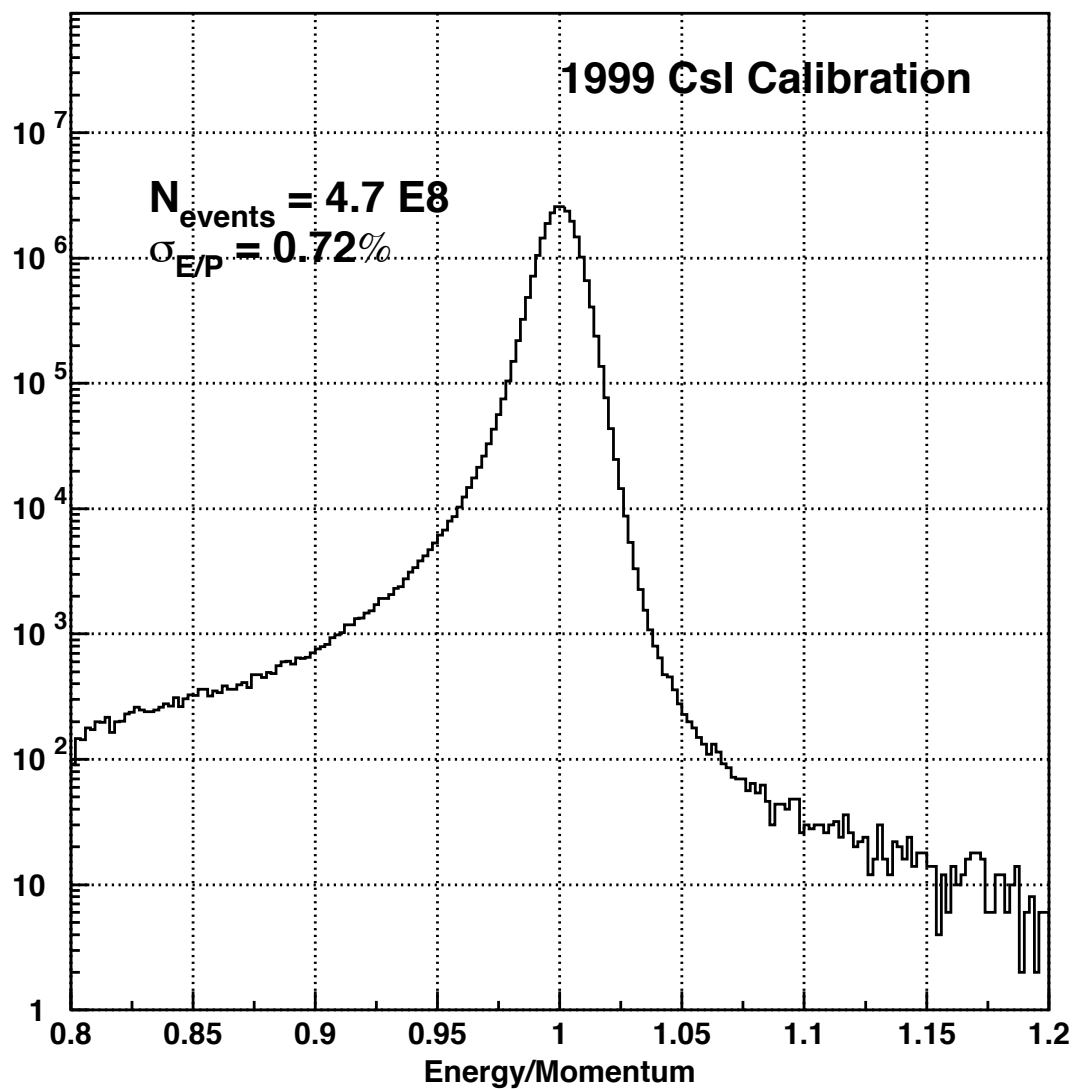


Figure 2.7: CsI calibration using electrons from $K_L \rightarrow \pi^\pm e^\mp \nu$ decays. Figure courtesy of E. Worcester.

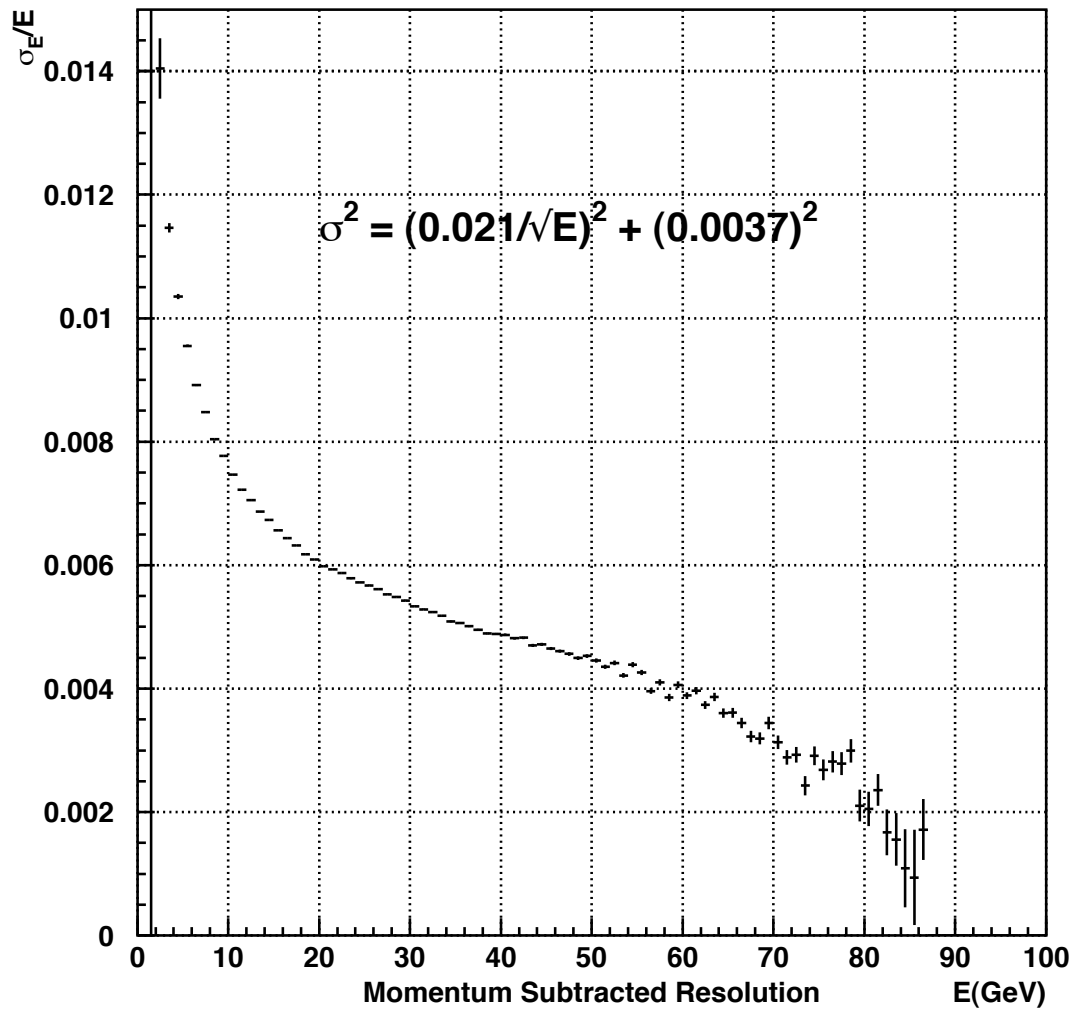


Figure 2.8: Energy resolution of the calorimeter. Figure courtesy of E. Worcester.

2.6 Veto System

A system of veto counters is used to reduce trigger rates and backgrounds, as well as to define apertures and edges that limit detector acceptance. The main vetoes are the photon veto counters (groups of these are in various locations throughout the detector), the mask anti (MA), the collar anti (CA), the hadron anti (HA), the back anti (BA), and the muon vetoes. The placement of these detectors is shown in Fig. 2.9. Each is briefly discussed below. For each veto counter, a signal above a certain threshold generates a digital pulse which is sent to the trigger system. The veto involvement in triggering is discussed in Section 2.7.

2.6.1 Photon Veto Counters

There are several sets of photon veto counters at various places in the detector configuration; a different name refers to each set, and their locations are given in Table 2.2. Five circular ring counters (RCs) directly surround the vacuum decay pipe (upstream of the vacuum window) to detect photons that leave the decay region; Fig. 2.10(a) shows a ring counter. Each RC is made of 24 alternating layers of lead and scintillator, totalling 16 radiation lengths.

| Veto Counter | Distance from target (m) |
|--------------|--------------------------|
| RC6 | 132.60 |
| RC7 | 138.60 |
| RC8 | 146.60 |
| RC9 | 152.60 |
| RC10 | 158.60 |
| SA2 | 165.12 |
| SA3 | 173.99 |
| SA4 | 180.02 |
| CIA | 185.19 |

Table 2.2: Z -positions of the photon veto counters: ring counters (RCs), spectrometer antis (SAs), and Cesium Iodide anti (CIA).

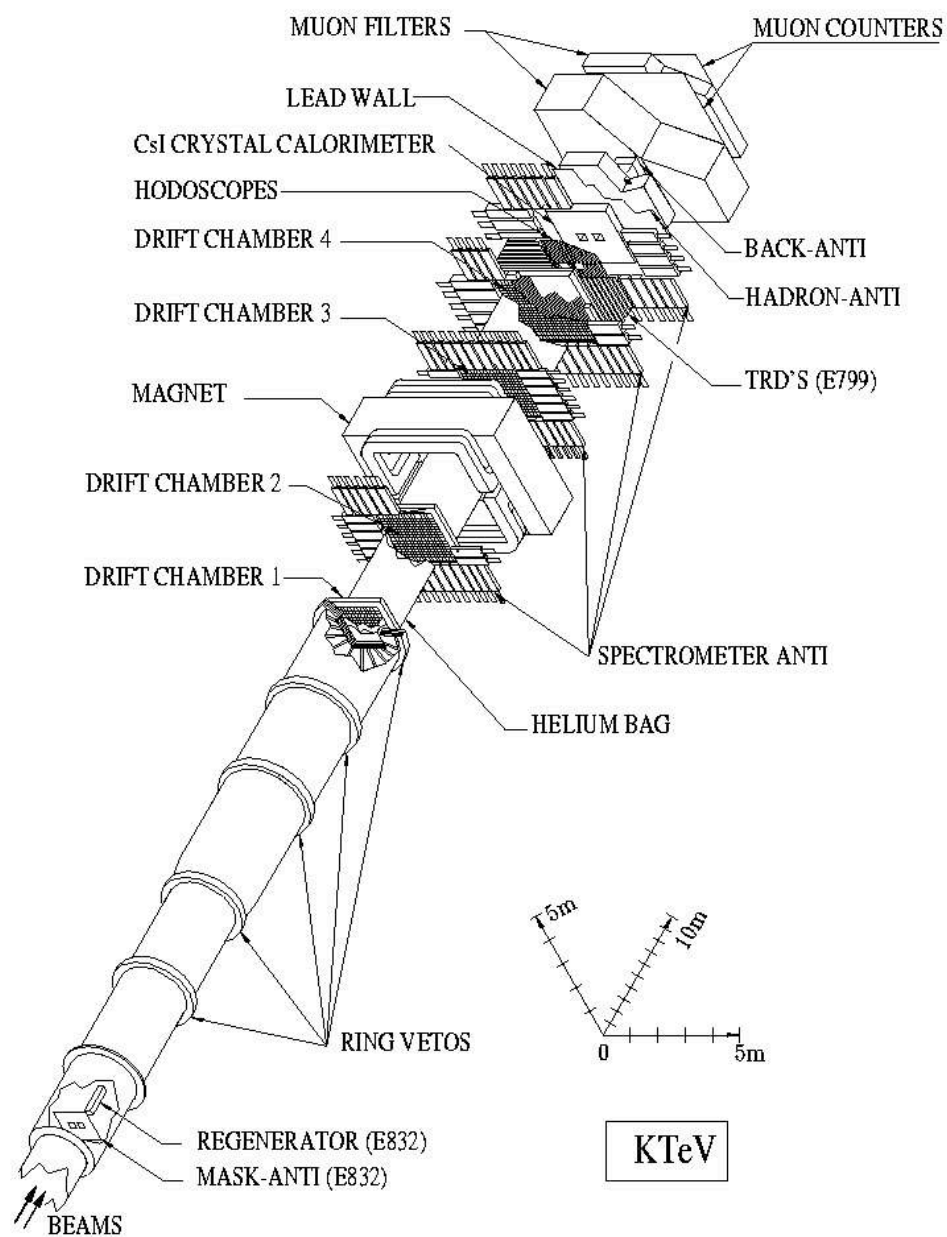


Figure 2.9: Three-dimensional cut-away view of the KTeV apparatus. The components that differ between E799 and E832 are labelled; recall that this analysis uses the E832 configuration. Figure courtesy of E. Pod.

Three spectrometer antis (SAs) are just upstream of drift chambers 2, 3, and 4, again, to detect photons that are leaving the detector's fiducial region as well as to define the chamber apertures. The SAs detect stray photons down to energies of 100 MeV [32, 33].

The Cesium Iodide anti (CIA) is a photon veto counter around the outer edge of the calorimeter. Analogous to the SAs, the CIA is just upstream of the calorimeter, and detects photons that would escape the calorimeter. The missing energy due to this photon leakage would cause misreconstruction of events. The CIA covers half a crystal on the perimeter of the calorimeter.

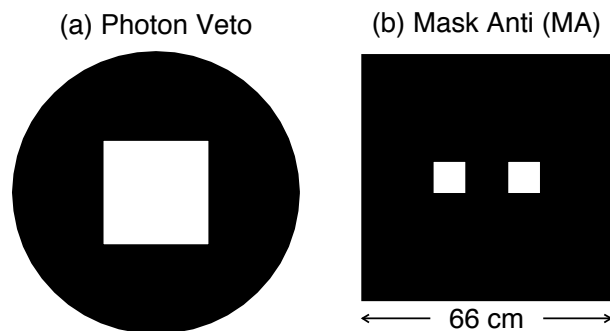


Figure 2.10: (a) Transverse view of a ring counter photon veto detector. Five of these are between the regenerator and the vacuum window. The square hole is approximately 1 meter. (b) Mask anti (MA) photon veto detector at $z = 123$ m. The beam holes are 9×9 cm², and they are separated by 20 cm from center to center. The black areas represent the active veto region on both diagrams. The PMTs are located at the outer edges of the two detectors.

2.6.2 The Regenerator

Inelastic interactions in the regenerator contaminate the K_S beam; to eliminate these events, the regenerator PMT signals are part of the veto system. The inelastic interactions leave deposits of a few MeV to 100 MeV from the recoil nuclear fragments. Therefore, a signal of 8 MeV or more from any scintillator element in the regenerator

causes the event to be rejected.

2.6.3 *The Mask Anti*

The mask anti (MA), as mentioned in Section 2.2.2, is just upstream of the regenerator at $z = 123$ m. The MA aperture is slightly smaller than the regenerator to eliminate beam particles that would miss the regenerator. The MA has two 9×9 cm² holes through which the beams pass. Figure 2.10(b) is a diagram of the MA.

2.6.4 *The Collar Anti*

The two beam holes in the calorimeter are surrounded by the collar anti (CA), shown in Fig. 2.11, which is just upstream of the CsI. The CA defines the beam hole apertures

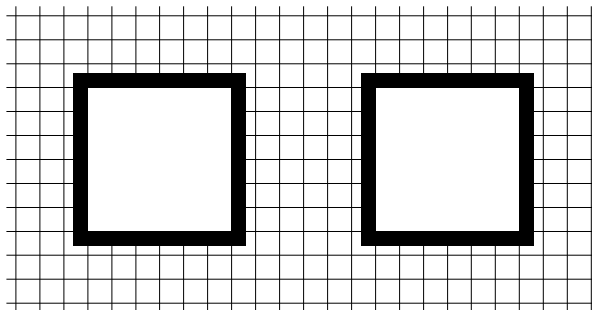


Figure 2.11: The collar anti (CA) is the dark square surrounding each of the calorimeter's beam holes. The inner 1.50 cm (60%) of the crystals around each beam hole are covered by the CA. The beams travel into the page. Wavelength-shifting fibers transmit signals to the PMTs at the outer edges of the calorimeter.

by detecting photons that hit a beam-hole-edge of the calorimeter and rejecting those events due to the energy leakage into the beamhole. Made of three layers of tungsten and scintillator, the CA signals are transmitted by fibers to PMTs on the outer edge of the calorimeter.

2.6.5 *The Hadron Anti and Back Anti*

The hadron anti (HA) and back anti (BA) are behind the calorimeter, downstream of a 15 cm thick wall of lead bricks. Although the CsI is 27 electromagnetic radiation lengths, it is only 1.4 hadronic interaction lengths, meaning that pions and other hadrons may not shower in the calorimeter. The lead wall absorbs any leftover electromagnetic energy in addition to inducing any pions which did not shower in the CsI to shower. These hadronic showers are then detected by the HA, and vetoed.

The lead wall and the HA each have a hole in them through which both beams pass; the beams then go through a hole in a 1-meter thick steel wall, which is part of the muon veto system (see Section 2.6.6). Behind this steel wall, the beams are dumped into the BA. The steel wall between the HA and the BA prevents any back-splash from the beam dump from producing signals in the HA. The positions of the lead wall, HA, BA, and steel wall are given in Table 2.3.

2.6.6 *Muon Veto Counters*

| Detector Element | Distance from target (m) |
|--------------------|--------------------------|
| Lead Wall | 188.53 |
| HA | 188.97 |
| Steel Filter (MF1) | 189.09 - 190.09 |
| BA | 191.09 |
| Steel Filter (MF2) | 191.74 - 194.74 |
| MU2 | 194.83 |
| Steel Filter (MF3) | 195.29 - 196.29 |
| MU3 | 196.36 |

Table 2.3: Z -positions of the detector components downstream of the calorimeter.

The muon veto system is a series of steel walls and muon counters downstream of the calorimeter. The first element, as was described in Section 2.6.5, is a 1 meter thick steel wall (MF1) between the HA and the BA, used to shield the HA from

the beam dump. Another steel wall, MF2, constitutes the neutral beam dump; it is 3 m deep, 3.4 m high, and 4.3 m wide. Following this is MU2, a hermetic veto of 56 overlapping counters which helps identify events with muons in the final state. Another 1 meter thick filter wall of steel (MF3) and another set of counters (MU3) are behind MU2. MF3 is intended to stop any remaining non-muonic activity (a 20 GeV/ c pion has only a 0.5% chance of getting past MF3), while allowing most muons to make it through and be identified (muons with momenta down to 7 GeV/ c will reach the MU3 counters). The positions of the elements of the muon system are given in Table 2.3.

2.7 Trigger System

Kaon decays occur at such a high rate that it is impossible to record every event to tape. In order to make efficient decisions about which events to record and which ones to throw out, KTeV uses a three-level trigger system. A data acquisition system (DAQ) manages the actual event recording. Since only a small fraction of the kaon decays are interesting, the three levels of the trigger become progressively more detailed in the signals they look at, as well as more time-consuming in their decision-making process.

Levels 1 and 2 of the trigger system are hardware stages, while Level 3 is a software stage. An online data split places all events that fall under a particular physics category onto one set of tapes. Finally, a data crunch is done as a first pass to filter through the events on a certain set of tapes to further narrow the sample for a particular analysis. Below is a brief description of the way the trigger works; for a more complete explanation, see [34]. In Section 3.2, we discuss the trigger and veto requirements specific to this analysis.

2.7.1 *Trigger Hodoscope: VV' Counters*

The so-called “trigger hodoscope” consists of two 0.95 m square banks of scintillator counters called VV' , viewed from the top and bottom by PMTs attached to lucite light guides. The banks are located just upstream of the calorimeter, with the V bank at $z = 183.90$ m and V' at $z = 183.95$ m. Because drift chamber signals are delayed (due to the drift times of the electrons), the VV' banks provide fast Level 1 trigger information on charged particles. Each of the 1.0 cm thick banks has vertical scintillator paddles; the two banks are overset by half of a paddle to reduce the possibility of missing a track through a gap between paddles. Tracks are bent in the x plane by the analysis magnet; the hodoscope’s vertical paddles allow for quick determination of the number of tracks in an event. As seen in Fig. 2.12, there are beam holes in each bank to avoid radiation damage to the calorimeter from interactions in the hodoscope.

2.7.2 *Level 1 Trigger*

The first level of the trigger system must make very fast decisions about whether an event might be of interest by evaluating the state of the detector for each RF bucket. It uses fast signals (Boolean “sources”) synchronized to the Tevatron beam structure and simple logic to do basic pattern identification in each of the 19 ns buckets. Level 1 either decides the event is uninteresting or accepts the event for further consideration, which begins the digitization of the detector. Importantly, Level 1 operates without any deadtime, ensuring all events are looked at on the first pass.

Each source is either ‘on’ or ‘off’, depending on the signal from a particular detector component. For instance, one source indicates whether there are at least two counters hit in the V bank of the trigger hodoscope (another source operates anal-

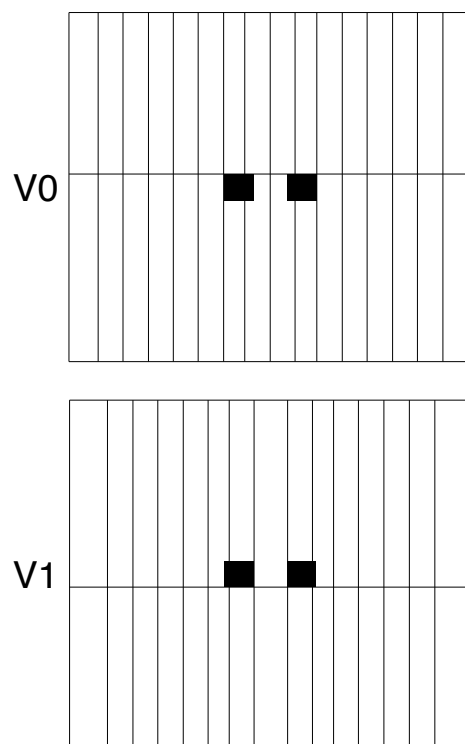


Figure 2.12: Diagram of the V and V' (also called V0 and V1) banks that make up the trigger hodoscope. The V counters are offset from the V' counters by half a paddle to minimize the possibility of missing a charged particle. The dark squares are the beam holes.

ogously for the V' bank). Another source, called “Energy-Total” (ET), indicates whether there is at least 24 GeV of energy in the calorimeter, based on an analog sum of PMT outputs. There are also sources corresponding to each veto detector. The information provided by the sources is combined in logical requirements, reducing the trigger rate. The raw Level 1 rate is 60 kHz, with no deadtime.

2.7.3 Level 2 Trigger

An accept decision by Level 1 begins the digitization of the detector in the form of ADCs, TDCs, and latch modules, in addition to storing the continuously digitized calorimeter information in the first-in-first-out buffers (FIFOs). The Level 2 trigger uses custom electronics to do more complicated pattern recognition than Level 1, using information from individual DC wires and calorimeter channels.

For charged triggers, Level 2 looks for hits in the y -view of the drift chambers, as described in [28]. Only the y -view is used in hit-counting because the $\text{Re}(\epsilon'/\epsilon)$ analysis is very sensitive to systematic biases between the vacuum and regenerator beams; since the wires in the y -view run in the x direction, events coming from both beams will use the same wires (whereas events from one beam will preferentially use the x -view’s vertical wires that are on the same side of the drift chambers as that beam). It takes ~ 800 ns to make a hit-counting decision. For some charged-mode triggers, the y Track Finder (YTF) then determines whether the hits are consistent with two straight tracks coming from a common vertex in the y -view; this typically takes a few hundred ns.

For both charged and neutral triggers, Level 2 uses the Hardware Cluster Counter (HCC), which counts isolated clusters of energy in the calorimeter. As described in Section 2.5, a cluster is a set of contiguous channels with at least 1 GeV of energy.

(Channels which touch only at a corner are not considered contiguous.) The HCC takes each channel's 'on' or 'off' signal from the ET board and looks at the crystals surrounding the channels that are 'on' to form a cluster. The Dalitz decay trigger requires seven or more "hardware clusters," since the final state has seven decay products. The algorithm for finding clusters is described in [28]; cluster-counting is the most time-consuming part of the Level 2 decision, taking $1.5 \mu\text{s}$ on average.

If Level 2 issues an accept decision, digitization of the detector continues and the detector is read out into VME buffers. If the event fails Level 2, the detector's front-end modules are cleared and the trigger system is re-set. The Level 2 rate is 10 kHz, and the fractional deadtime is 35% (coming from 2-3 μs for a Level 2 decision and $\sim 15 \mu\text{s}$ for readout on a Level 2 accept). There is enough memory to store the data from the entire spill, which is then used in Level 3 to make a final decision to accept or reject the event.

2.7.4 *Level 1 and 2 Trigger Definitions*

The Level 1 and 2 trigger definitions for 1999's 14 physics triggers are in a text file that specifies the logic that the sources have to satisfy for each trigger. The prescales are also kept in this file; some decays such as $K_L \rightarrow 3\pi^0$ are so numerous that we do not want to keep all of them, so the hardware prescale of 2 tells the $K_L \rightarrow 3\pi^0$ trigger (trigger 6) to keep only one of every two events that pass the hardware trigger requirements. Prescaling common decay modes saves valuable disk space and processing time for more rare events that are the objects of study.

The beam triggers include those for the $\text{Re}(\epsilon'/\epsilon)$ analysis ($K \rightarrow \pi^+\pi^-$ and $K \rightarrow \pi^0\pi^0$), those for studying trigger inefficiencies, and those for studying rare kaon decays. Additionally, there are beam triggers that record accidental activity

from the accidental counters used later in the Monte Carlo to realistically simulate underlying detector activity. There is also a set of calibration triggers, used to monitor detector performance, such as the trigger for the laser calibration of the calorimeter discussed in Section 2.5.2. Most of the calibration triggers are taken in the ~ 40 seconds between spills, although some are taken continuously. Each of the triggers has its own Level 1, 2, and 3 requirements; the requirements for a single trigger are the same for both beams (vacuum and regenerator) and both regenerator positions (left and right). For a detailed description of each of the various triggers, see [34].

2.7.5 Level 3 Trigger and Online Data Split

The Level 3 trigger decision is made in software by the data acquisition (DAQ) system. If data from a spill has been written to memory, Level 3 has until the next spill to make its decision before incurring deadtime. The system consists of 24 CPUs running in parallel on four SGI Challenge servers, and does basic reconstruction with very loose kinematic requirements to make a final accept or reject decision. Because Level 3 reconstruction is happening in real-time, it uses online calibration constants. These constants are refined later for the final analysis. Each of the four SGI servers is referred to as a “DAQ plane.” Planes 1, 2, and 4 were used in a round-robin manner to filter physics events while plane 3 was reserved for detector monitoring and calibration triggers. We will return to the DAQ planes briefly in Section 3.3.

Very generally, for charged events, if the Level 3 software identifies a vertex candidate, it unpacks the calorimeter information and looks for clusters that match the tracks. For neutral events, it looks for clusters that match the ones found by the HCC. A fraction of all input events are tagged as “random accepts,” and kept regardless of the Level 3 decision. Events are tagged according to which data sample(s)

they belong to, and are written either to tape (for more common decay modes) or to a large array of disks such that each disk holds events of like type based on the tag. When a disk became full, it was spooled to an output tape. The split tapes for a particular type of decay can then be used as a starting point for an analysis. It is still time-consuming to read through an entire set of tapes corresponding to the decay under study, so a crunch of those tapes is used to loosely filter through the events, eliminating ones that are clearly not candidates for a specific analysis. This reduces the number of events on which the final analysis code must be run.

Further prescales may also be applied at this time to reduce the rate for very common decay modes; for instance, trigger 6 (the $K_L \rightarrow 3\pi^0$ trigger) has a software prescale of 5/2. Combining this with the hardware prescale of 2 (see Section 2.7.4) gives trigger 6 an overall prescale of 5; that is, one in every five accepted events is kept.

CHAPTER 3

DATA ANALYSIS

This chapter describes the data analysis necessary for the measurement of $B(\pi^0 \rightarrow e^+e^-\gamma)/B(\pi^0 \rightarrow \gamma\gamma)$. Starting with the signal and normalization mode event samples provided by the requirements of two of the E832 triggers, we progressively exclude more and more candidate events through a check of data-sample integrity, basic track-finding and clustering algorithms, reconstruction of the decay vertex and parent particle invariant mass, and a series of selection criteria. These steps result in refined event samples for both the normalization mode and the signal mode that can then be used to make the $B(\pi^0 \rightarrow e^+e^-\gamma)/B(\pi^0 \rightarrow \gamma\gamma)$ measurement.

3.1 Overview of Analysis Technique

The signal decay mode is $K_L \rightarrow 3\pi^0$ with one π^0 decaying to $e^+e^-\gamma$ and the remaining two π^0 s each decaying to $\gamma\gamma$, denoted $K_L \rightarrow 3\pi_D^0$, and the normalization mode is $K_L \rightarrow 3\pi^0 \rightarrow 6\gamma$. Ideally, both signal and normalization samples would come from the same trigger to reduce systematic errors associated with relative trigger inefficiencies. However, the only trigger that would have been suitable for this, trigger 6, requires exactly six clusters at Level 3, while Dalitz decays produce seven clusters in the calorimeter. Thus, trigger 6 (with a hardware prescale of 2, a software prescale of 5/2, and an analysis prescale of 10) is used for $K_L \rightarrow 3\pi^0$, the normalization mode. Trigger 14 (with no prescale), which requires seven or more hardware clusters, is used for $K_L \rightarrow 3\pi_D^0$. (As a historical note, the original motivation behind trigger 14 was to study the CsI energy reconstruction for close electrons; however, insufficient statistics prevented such a study from being completed.) Trigger definitions for both triggers are given below. Systematic errors associated with using two different triggers are

discussed in Sections 6.5, 6.6, and 6.7.

3.2 Trigger and Veto Requirements

The detector sources discussed in Section 2.7.2 are combined in specific ways to form the hardware (Level 1 and 2) trigger requirements for triggers 6 and 14. Below are the logical trigger definitions (where * indicates the logical AND, and ! indicates the logical NOT), followed by an explanation of each element in the definitions.

$$\text{Trigger6} = \text{SPILL} * \text{ET_NEUT} * \text{VETO_NEUT} * \text{!CA} * \text{HCC_GE6}$$

$$\text{Trigger14} = \text{SPILL} * \text{2V} * \text{DC12} * \text{ET_NEUT} * \text{VETO_CHRG} * \text{!HA_PION} * \text{!CA} * \text{HCC_GE7} * \text{1HCY}$$

Both VETO_NEUT and VETO_CHRG are formed out of basic veto sources:

$$\text{VETO_NEUT} = \text{!SA2} * \text{!SA3} * \text{!SA4} * \text{!CIA} * \text{!REG} * \text{!HA_NEUT}$$

$$\text{VETO_CHRG} = \text{!SA2} * \text{!SA3} * \text{!SA4} * \text{!CIA} * \text{!REG} * \text{!MU2}$$

3.2.1 Trigger Elements Common to Both Modes

The trigger and veto elements required by both trigger 6 and trigger 14 and a brief explanation of each are below.

- **SPILL:** Information regarding detector problems during data-taking was stored in a database, where individual spills could be marked “bad” for various reasons; both triggers require that none of the bad spill bits is on.
- **ET_NEUT:** As discussed in Section 2.7.2, this source indicates whether an analog sum of the calorimeter PMT signals shows an in-time energy deposit of at least 24 GeV in the CsI.

- !CA: There is one CA source for each of the two beamholes; if any of the CA's PMTs registers greater than 14 GeV of energy, the corresponding source turns on, vetoing the event.
- HCC_GE6(7): This requires that the HCC found at least 6(7) clusters in the CsI.
- !SA2(3,4): None of the photon vetoes around the three downstream drift chambers can have more than a 500 MeV energy deposit.
- !CIA: The photon veto around the outer edge of the calorimeter is required to have less than 500 MeV of energy.
- !REG: The sources corresponding to the regenerator veto should not be on.

3.2.2 *Trigger Elements Unique to Signal Mode*

Trigger 14 has additional requirements associated with identifying charged events. These requirements are summarized below.

- 2V: This is shorthand for the requirement of two hits in one view and one hit in the other view for the VV' banks. This somewhat loose requirement allows for the possibility that one of the tracks may have gone through a crack in one of the banks (see Section 2.7.1).
- DC12: This is shorthand for the requirement that there are hits in three of the four views in the first two drift chambers. This helps to eliminate cases where the kaon decays downstream of the drift chambers, leaving hits in VV' , but no tracks in the spectrometer.

- 1HCY: There must be at least one hit in every drift chamber y -view. As discussed in Section 2.7.3, only the y -views are used because events from both beams use the same wires in this view.
- !MU2: To eliminate charged events that produce muons instead of electrons, events with an appreciable amount of energy in a MU2 counter are vetoed.

3.2.3 *Equalizing the HA and MU2 Requirements in the Two Triggers*

The original trigger definitions for triggers 6 and 14 have different veto thresholds for the HA. Trigger 6 includes !HA_NEUT, which vetoes events with more than 14 minimum ionizing particles (MIPS) in the HA. Trigger 14 includes !HA_PION, which has a lower (stricter) veto threshold, at 3 MIPS in the HA. This means that trigger 14 will reject more events than trigger 6 based on the HA information. Since this could bias the analysis, we needed to equalize the HA requirement between the two triggers. This was accomplished by requiring that events in both triggers (both modes) pass the 3-MIP threshold in order to make it into the event samples. It is worth noting that tightening the HA requirement in the normalization mode has a negligible effect on the number of $K_L \rightarrow 3\pi^0$ events in the final sample for this analysis.

Similarly, trigger 14 requires that the MU2 counters not be hit, while trigger 6 does not include this requirement. In order to ensure that this difference does not cause a bias in the analysis, we impose the MU2 requirement in trigger 6. We note that making this change has an effect on $B(\pi^0 \rightarrow e^+e^-\gamma)/B(\pi^0 \rightarrow \gamma\gamma)$ that is smaller than the Monte Carlo statistical uncertainty.

3.2.4 Level 3 Trigger Requirements

The Level 3 requirements for both trigger 6 and trigger 14 are very loose. As discussed in Section 2.7.5, basic kaon mass reconstruction is done. Trigger 6 requires that the reconstructed $6\text{-}\gamma$ mass be between 0.400 and 99.0 GeV/c^2 (recall that the kaon mass is 0.498 GeV/c^2), and that the reconstructed decay vertex be anywhere from $z = 0.0$ to $z = 170.0$ meters from the target. Trigger 14 requires that the E/p of each track be between 0.75 and 1.25, to roughly check that the tracks are consistent with being electrons. Additionally, trigger 14 only processes events which have less than 400 two-track candidates, to eliminate events which would have very long processing times.

3.3 Data Sample Integrity

Triggers 6 and 14 provide the event samples that are the starting point for the analysis. Because the two samples are from different triggers, we need to exclude runs and spills that have events in one mode but not in the other (due to trigger or data tape problems that are not common between the two modes). First we exclude blocks of runs that are on data tapes that fail one of the two crunches; second, we look at the ratio of trigger 6 to trigger 14 events within each run to search for other possible problems. These two steps are described below.

The normalization mode data (from trigger 6) is found on the “QKT” tapes (QKT001-QKT055). The events on these tapes go through a crunch, which looks for events from trigger 6 and writes every tenth event out to a data file. The final analysis will be run on this data. Because KTeV collected so many $3\pi^0$ events, the prescale of 10 included in the crunch allows us to keep plenty of statistics while saving time by not processing every event. Two of the tapes (QKT042 and QKT049) fail in the crunch; we add the runs and spills from those tapes to the bad runs and spills

list, and they are not included in the analysis.

A very similar process is used for the signal mode (from trigger 14). The Dalitz events come from the “QKSM” tapes (QKSM01-QKSM20). The events on these tapes go through a crunch job which looks for trigger 14 events and writes them to a data file. Tapes QKSM01 and QKSM10 fail in the crunch; the runs and spills in those tapes are removed from the analysis for both modes.

The next step in refining these samples is to perform checks on the quality of the data. The data for this analysis comes from the 1999 data-taking run of E832. This data-taking period occurred from mid-June to mid-September in 1999. Within this period, data were collected in “runs,” which lasted up to about eight hours, if the Tevatron was running smoothly. The maximum run length of about eight hours was because a new run needed to be started when the data tapes in use became full. Runs could be stopped at any time for a number of other reasons, such as beam or detector problems.

We have already excluded some runs based on the results of the crunch for each mode. We perform a check to refine the remaining samples by comparing the run-by-run ratios of the number of trigger 6 ($3\pi^0$) events to trigger 14 (Dalitz) events to the average of this ratio over all runs. This is done by looking for individual runs with ratios that are more than four sigma from the average. Eight outlying runs are identified. Two of these runs have spill distributions that are different between signal and normalization mode; the analysis is modified to include only spill ranges that are present in both modes. The other six outlying runs have $3\pi^0$ to Dalitz event ratios that are approximately two-thirds of the average ratio. Further investigation shows that the trigger 6 sample is missing one of the three DAQ planes (see Section 2.7.5) in each of these six runs. This was due to problems during the split. These runs are removed from both modes.

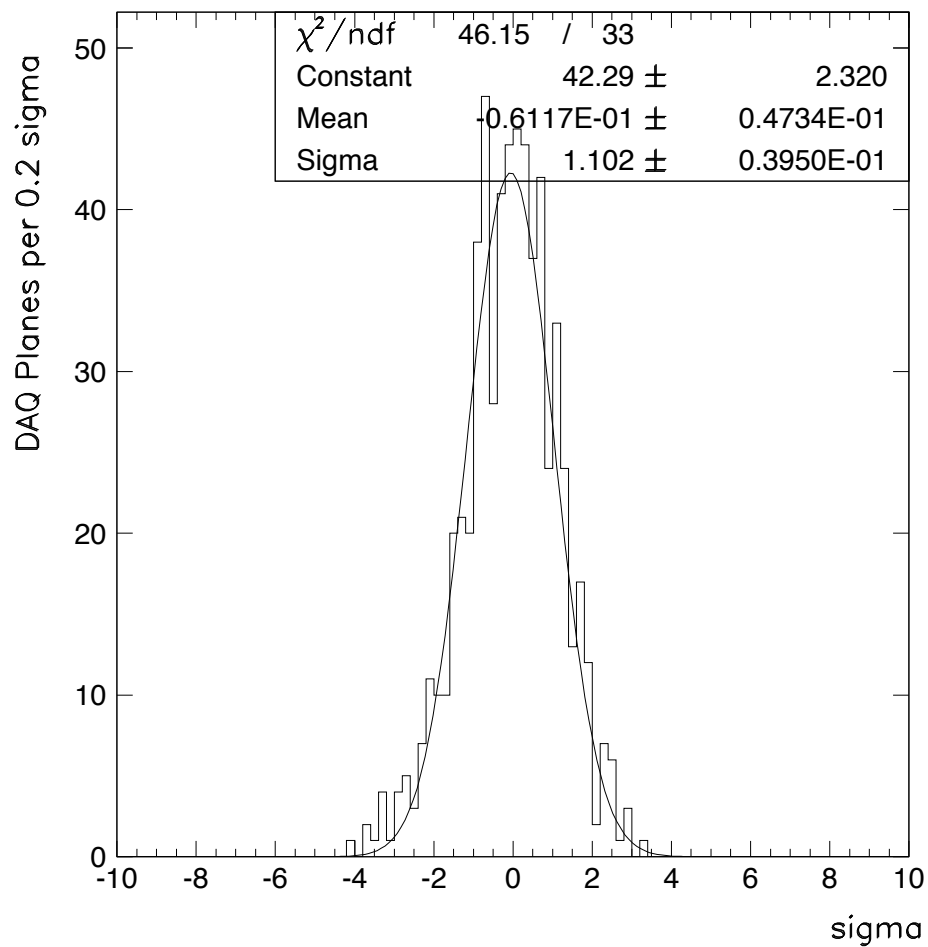


Figure 3.1: The sigma distribution, fit to a gaussian, for the ratio of trigger 6 ($3\pi^0$) events to trigger 14 (Dalitz) events in each DAQ plane in each run, relative to the average ratio over all included runs.

After removing these runs and spills, run ratios are re-evaluated, this time comparing the ratio in each DAQ plane (within each run) to the overall ratio across all planes and runs. The distribution of the number of sigma away from average for each plane’s ratio is shown in Fig. 3.1. Since the sigma distribution is consistent with a gaussian centered at 0 with a width of ~ 1 , this plot suggests that we have eliminated all planes and runs in which problems occurred during data-taking, tape splits, and tape migration.

3.4 Event Reconstruction

Following the data quality checks, the event samples undergo basic event reconstruction, consisting of a track-finding algorithm based on drift chamber information and a clustering algorithm to determine the energies and positions of decay products in the calorimeter. The reconstruction uses final calibration constants that are stored in databases.

3.4.1 Track Finding

The track-finding algorithm begins by unpacking the drift chamber TDC information and converting hit times to drift distances using the $x(t)$ maps described in Section 2.4.2. Only the earliest hit on a wire within the in-time window is counted. Once all the hits are found, the algorithm “walks” across each view in a chamber and looks for pairs of hits on complementary wires and for isolated hits.

Hit pairs are assigned to a quality category based on the sum of drift distances (SOD) for the two wires. Good-SOD pairs are those within 1 mm of the 6.35 mm cell size. Low-SOD pairs, those with SODs below 5.35 mm, can result from two tracks traversing the same cell (so that each sense wire sees the charge from the nearest

track), or from a single track emitting a delta-ray (an energetic electron knocked out of the DC gas starts an avalanche that reaches the sense wire earlier than the electrons from the track itself, causing an early signal and an underestimated drift distance). High-SOD pairs, those with SODs above 7.35 mm, can result from tracks passing too close to a sense wire because the wires do not always register the current from a single drift electron. In the case of a close track, often the first drift electron will reach the wire, but will not induce enough current to constitute a hit; a short time later, enough avalanche electrons reach the wire to produce a signal, but that signal is late, causing the drift distance to be overestimated [30].

Without any inefficiencies or imperfections, a two-track event would leave 32 hits in the chambers (one hit per plane for each track), and pairs of hits in complementary planes would have good-SODs. There is an intrinsic inefficiency of less than 1% for each wire. Because there are various sources of inefficiencies in the chambers, the track-finding algorithm also identifies and considers single hits.

Examples of types of SODs and hits are shown in Fig. 3.2. The event shown would result in the following list of pairs (from left to right).

- Good-SOD pair in cell 2
- Low-SOD pairs in cell 3 (from a combination of other hits) and in cell 4, from a real low-SOD pair
- High-SOD pair in cell 9
- Isolated singles in cell 12

To facilitate track-finding, good-SOD pairs are given a value of 4, low-SOD and high-SOD pairs are given a value of 2, and isolated hits are given a value of 1. For the purposes of forming tracks, pairs of any quality and isolated hits are all referred

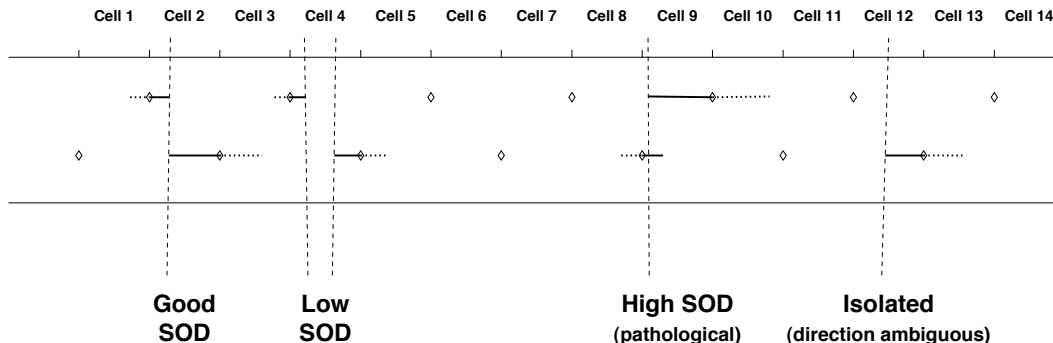


Figure 3.2: Diagram of types of SODs and hits used in the track-finding algorithm. The diamonds are sense wire positions in the drift chamber and the vertical dashed lines are the tracks. The horizontal solid lines are the true drift distances; the horizontal dotted lines show the same drift distance for a track on the opposite side of the sense wire. The pairs that the tracking algorithm would find in this example are described in the text.

to generically as “pairs,” and the algorithm creates a list of pair positions and values for each chamber. Isolated hits are added to the list twice, once for each side of the wire (see Fig. 3.2). Each hit in a low-SOD or high-SOD pair is added to the list separately. Each good-SOD pair is added to the list as a pair.

All x and y track candidates will be required to consist of pairs whose quality values add up to at least 11 (out of a possible 16). This allows the track to contain two low-SOD (or high-SOD) pairs, one isolated hit, or one low-SOD (or high-SOD) pair and one isolated hit.

After hit-pairs have been identified and classified, the algorithm searches for track candidates separately in the two views by looping over all the points in space at which hits have been found, starting with the y -view for simplicity (the analysis magnet bends the trajectories in the x -view, making it slightly more complicated to reconstruct tracks). The track candidates must form a straight line in the y -view. If the algorithm cannot find at least two track candidates in the y -view, the process ends. In the x -view, the upstream and downstream track segments must meet at the magnet

within 6 mm. All track candidates which meet the hit-pair quality requirements are kept. At this stage, track candidates may share hit-pairs.

With the x and y track candidates in hand, the algorithm must rely on information from the calorimeter to match up the x and y coordinates of a single track. The algorithm loops over each possible pair of $x - y$ candidates to see if the track formed by the pair points within 7 cm of a cluster at the calorimeter (more on clustering in Section 3.4.2). Finally, we want to require that the two tracks came from a common decay vertex in the vacuum decay region; because the hit resolution is not perfect, a 2 mm “slop” in the position of each space point is allowed when determining whether two tracks point back to a common vertex. For a given vertex candidate, the two tracks cannot share any hits.

At this point, the algorithm applies a series of corrections to the hit positions (for example, to correct for any drift chamber misalignment and for the finite propagation speed of the signals on the wires). Each pair’s SOD is recalculated, correcting for the track angle. SODs which are low by more than 0.6 mm are assumed to be low due to delta ray emission, and the algorithm chooses a replacement hit which is more consistent with the hits in the other chambers. The fringe magnetic field (see Section 2.4.1) effect is corrected in DC2 and DC3 x -view hits. In the y -view, tracks are refit, this time allowing for bending in the magnet; this is because the three-dimensional magnetic field does actually cause some “vertical focusing” (bending and displacement of charged particles in the y -view). Finally, the track momentum is recalculated using the field integral specific to the location of the track in the magnet.

After all corrections, the track-finding algorithm provides a list of vertex candidates, from which we choose the best candidate, by minimizing a quantity called the vertex χ^2 . The x tracks and y tracks are extrapolated upstream to define an $x - z$ and $y - z$ vertex. The vertex χ^2 is calculated based on the difference between these

two vertices, Δz_{vtx} :

$$\chi^2 = \frac{\Delta z_{vtx}}{\sigma_{\Delta z}}. \quad (3.1)$$

The lower the value of the vertex χ^2 , the more likely it is that the two track candidates came from the same z position. The final determination of which track candidates to use for an event is based on a combination of minimizing the vertex χ^2 , finding the tracks that match best at the magnet, and the number of low-SOD (or high-SOD) and single hits used in the tracks [28].

3.4.2 Clustering

There are photons in the final state in both the signal mode (five photons) and the normalization mode (six photons). The calorimeter is the sole source of information about photon energies and positions. The Level 2 trigger includes the basic requirement that the HCC finds at least seven clusters (five of which correspond to photons) in the signal mode trigger, and at least six clusters in the normalization mode trigger. In our offline analysis, the clustering algorithm refines the measured photon energies and positions.

The cluster-finding algorithm begins by unpacking the calorimeter data and getting the energy in each channel. The DPMTs provide the integrated charge in each time slice from each PMT. The laser calibrations and electron studies from $K_L \rightarrow \pi^\pm e^\mp \nu$ decays (described in Section 2.5.2) are used to convert this charge to an energy.

In Level 2 of the trigger, the HCC finds crystals with at least 1 GeV of energy and turns on the HCC bit for those channels. From the channels whose HCC bits are ‘on,’ we need to determine which ones are “seed” blocks. A block is a seed block if none of its neighbors has an HCC bit set, or if it has the highest energy of its

neighbors which have their HCC bits on. Requiring seed blocks to have their HCC bits on helps to verify the trigger, and helps to reduce contamination by accidental hits by ensuring that the particles are in-time. Around each seed block, a 3×3 (large blocks) or 7×7 (small blocks) cluster is defined. The raw energy of the cluster is the sum of the block energies, and the x (y) position of the cluster is determined by summing the energies in each column (row) of the cluster and comparing the ratios of column (row) energies against look-up tables from a sample of real photons. The x and y position resolutions are approximately 1 mm in the small blocks and 1.8 mm in the large blocks (after all corrections).

Clusters found by the HCC during Level 2 of the trigger are referred to as hardware clusters. A second round of clustering is performed during the software analysis. Any crystal (which is not part of a hardware cluster) with greater energy than its neighbors is a seed block for the purposes of software clustering. Software clusters, formed in the same manner as the hardware clusters, are additional low-energy clusters. Although we do not explicitly use software clusters in the event reconstruction in this analysis, the distribution of software clusters is sensitive to both accidentals and radiative corrections, making it useful for systematic studies (see Section 6.2 and Section 6.4).

A number of corrections are applied to the raw cluster energies and positions. The “uniformity correction” is necessary because the light collection along the length of a crystal is intrinsically nonuniform. The corrections for each crystal were determined with studies using cosmic ray muons. A cluster near a beam hole or near the edge of the calorimeter may be missing blocks in its 3×3 or 7×7 grid; the energy that would have been in these blocks is estimated (using a look-up table) and included in the cluster energy. The “overlap correction” is done for clusters that share some blocks using an iterative procedure for dividing the energy in the common channels. Another correction is done for blocks which are close to another cluster (but do not overlap);

some of the cluster’s energy may have leaked into these blocks. Samples of electrons were used to study the response of the calorimeter as a function of various factors. These studies reveal that the calorimeter response varies as a function of transverse position within a crystal; the response can be lower by a few percent at the edges of the crystal relative to the response at the center. The “intra-block correction” takes care of this. Calorimeter variations with temperature and with time (due to crystal degradation from radiation damage) were also measured and corrected. Much more information on each of these corrections is available in [29].

3.5 Reconstructing the Decay Vertex

The basic method of identifying candidate events in the analysis is to reconstruct the kaon’s decay position (z -distance from the target). Recall that in each mode, the kaon decays into three pions, each of which then decays into the final state particles that we observe in the detector. Information about the final state particles allows us to determine where each pion decays; because the π^0 lifetime is extremely short ($c\tau \approx 25$ nm), the pion decay position can be considered to be that of the kaon decay. Reconstructing the kaon decay position is similar for both modes; however, since the normalization mode is slightly simpler, we describe it first.

3.5.1 *Vertex z Position: Normalization Mode*

In the normalization mode, we search for three π^0 s, each of which decays to two photons. Our normalization mode event sample contains events with six hardware clusters in the calorimeter, due to the requirements of trigger 6. We need to determine which clusters (photons) came from which π^0 ; this amounts to determining the correct pairing of the photons out of the 15 possible pairings. (There are $6!$ ways to order

the photons, but the order of each pair does not matter, so divide by 2 for each pair, and the order of the three pairs does not matter, so divide by 3! to get $\frac{6!}{8 \times 6} = 15$.) This is done (in a KTEVANA routine called KTPAIRS) by looping over all possible pairings and calculating the z positions of the three pions, assuming the pion mass. To see how this is done, consider one pair of photons. Let the four-momenta of the photons be p_1 and p_2 . We have

$$m_\pi^2 = (p_1 + p_2)^2 = (E_1 + E_2)^2 - (\vec{p}_1 + \vec{p}_2)^2 \quad (3.2)$$

$$m_\pi^2 = E_1^2 + E_2^2 + 2E_1E_2 - |\vec{p}_1|^2 - |\vec{p}_2|^2 - 2\vec{p}_1 \cdot \vec{p}_2. \quad (3.3)$$

Since the photon is massless, $E_i^2 - |\vec{p}_i|^2 = 0$, and $|\vec{p}_i| = E_i$ where E_i is the photon energy. Then,

$$m_\pi^2 = 2E_1E_2(1 - \cos(\theta_{12})) \quad (3.4)$$

$$m_\pi^2 = 4E_1E_2 \sin^2\left(\frac{\theta_{12}}{2}\right), \quad (3.5)$$

where θ_{12} is the angle between the photons and we have used a trigonometric identity. Assuming this angle is small (justifiable, since the distance the photons must travel to reach the calorimeter is large relative to the transverse size of the calorimeter), we can use the small-angle approximation ($\sin(\alpha) \approx \alpha$ for small α), and also approximate:

$$\theta_{12} \approx \frac{r_{12}}{z_{12}}. \quad (3.6)$$

Here, r_{12} is the distance separating the two photons at the calorimeter and z_{12} is the distance between the pion decay position for this photon pair and the calorimeter,

the quantity of interest. We have

$$z_{12} \approx \frac{r_{12}}{m_\pi} \sqrt{E_1 E_2}. \quad (3.7)$$

This z calculation is used to determine the best pairing of the six photons, as described next.

3.5.2 Pairing χ^2

The best pairing of the six photons is the one which results in consistent z positions for the three π^0 s, since all the pions should have decayed at the same place (at the kaon decay position). For the more simple case of two pions, Fig. 3.3 shows the three possible pairings of the four final state photons. In our six photon case, for each pairing, a χ^2 is formed based on the three reconstructed pion z distances from the calorimeter, the uncertainties on those positions (σ_z), and the weighted average of the three z distances (\bar{z}). If z_a (σ_{z_a}), z_b (σ_{z_b}), and z_c (σ_{z_c}) are the z positions (uncertainties) calculated for a particular pairing of the six photons, the χ^2 for that pairing is

$$\chi^2 = \frac{(z_a - \bar{z})^2}{\sigma_{z_a}^2} + \frac{(z_b - \bar{z})^2}{\sigma_{z_b}^2} + \frac{(z_c - \bar{z})^2}{\sigma_{z_c}^2}. \quad (3.8)$$

The best pairing is the one which has the smallest pairing χ^2 ; Fig. 3.4 shows the χ^2 distribution of the best pairing for each event in data. The distance between the calorimeter and the reconstructed kaon vertex is \bar{z} , the average z associated with the best pairing. Since the target is at $z = 0$ in the experimental reference frame, to get the z position of the kaon decay vertex, we subtract the vertex distance to the CsI (\bar{z}) from the z position of the mean photon shower depth in the CsI. This reconstructed kaon vertex position allows us to construct the four-momenta of the

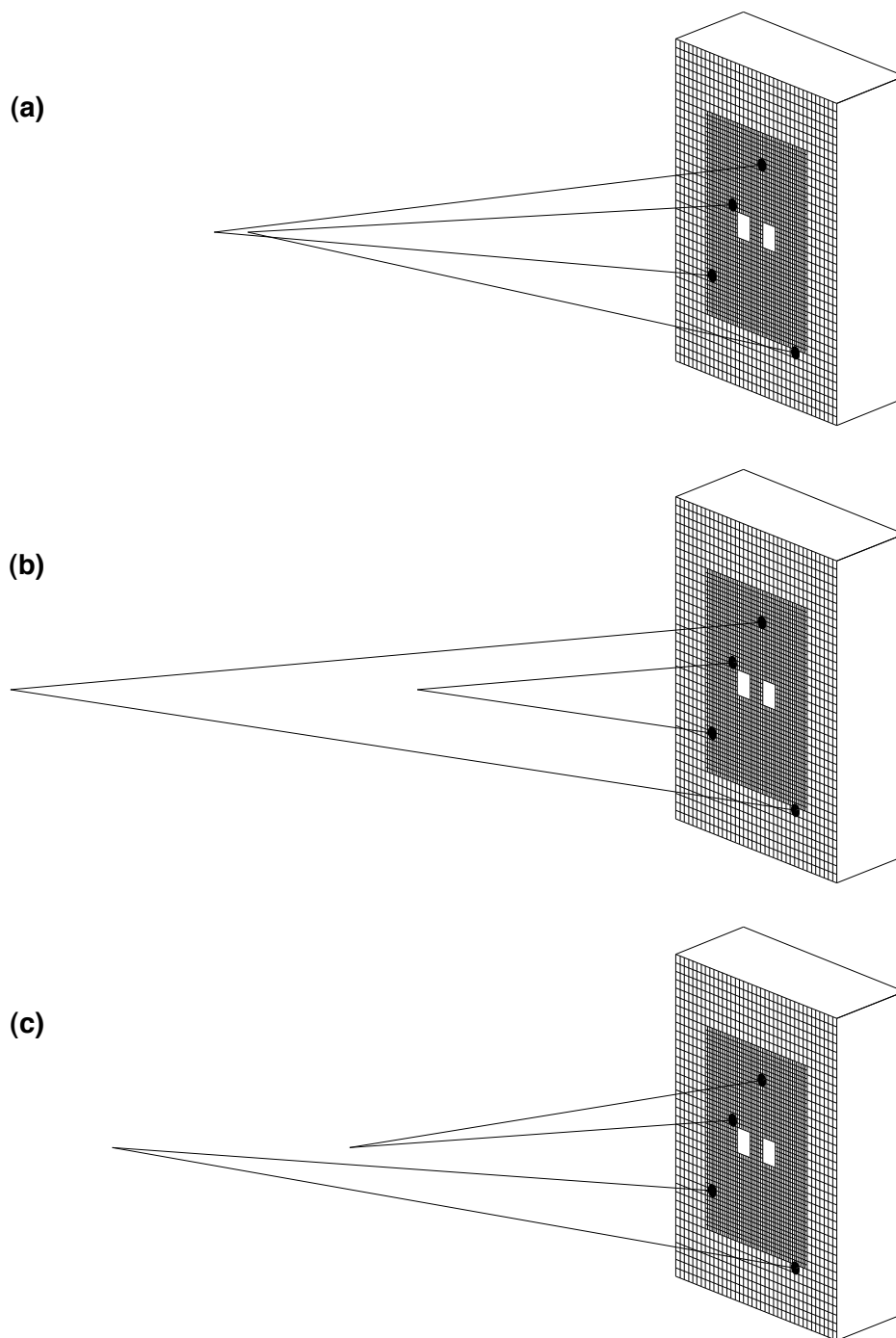


Figure 3.3: The three ways to pair four photons to make two π^0 s. Pairing (a) is the best pairing, since the two vertices are at the same position, within reconstruction uncertainties. Both modes in this analysis have more possible pairings (15 each) since there are more than four photons in the final states, but this diagram illustrates the basic idea of reconstructing the π^0 s by looking at all possible pairing combinations.

six photons, from which we reconstruct the $3\pi^0$ invariant mass; this procedure will be described in Section 3.6.

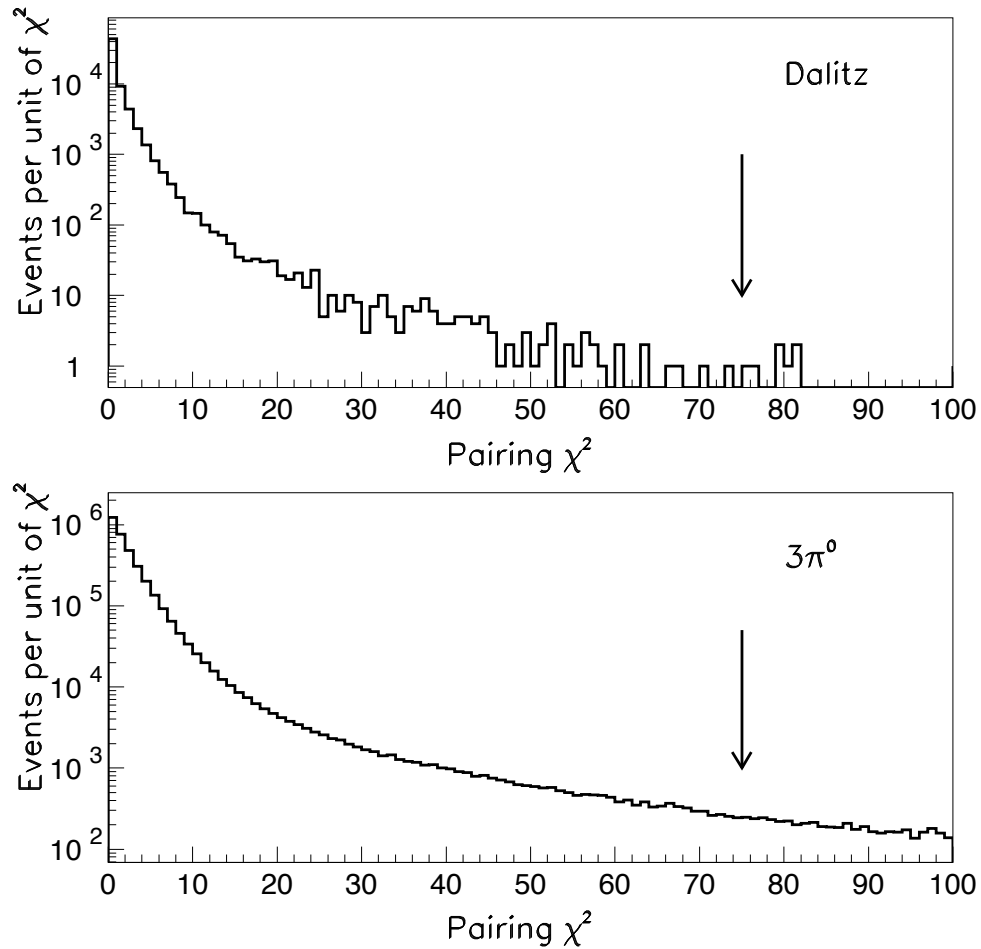


Figure 3.4: The pairing χ^2 distributions in the data for both the signal and normalization mode samples. The arrow indicates the analysis requirement that the pairing χ^2 be less than 75 in each sample in order to reduce cases of mispairing.

3.5.3 Vertex z Position: Signal Mode

In the signal mode, we require seven hardware clusters in the calorimeter and two reconstructed tracks. After matching two of the clusters with the tracks, the best

pairing of the five remaining “neutral” clusters (to make two π^0 s) is determined using the method described in Sections 3.5.1 and 3.5.2. (Again, there are 15 possible pairings, since there are now $5!$ ways to order the photons, but the order within the two pairs does not matter nor does the order of the two pairs, so we have $\frac{5!}{4 \times 2} = 15$.)

The two z distances from the calorimeter are calculated for each pairing using Eq. 3.7, and a pairing χ^2 is formed for each combination using the two pion z distances (as in Eq. 3.8, modified for only two π^0 s). The pairing which minimizes this χ^2 is chosen. Figure 3.4 shows the χ^2 distribution of the best pairing for each event in data. The corresponding weighted average distance (\bar{z}) is subtracted from the z position of the mean photon shower depth in the CsI to obtain the reconstructed kaon decay position. The leftover neutral cluster which does not belong to either pair is tagged as the photon coming from the Dalitz decay, $\pi^0 \rightarrow e^+e^-\gamma$, and is ‘paired’ with the two tracks.

Recall that the tracking algorithm described in Section 3.4.1 finds the vertex corresponding to the two tracks. The vertex z position based on tracking should be consistent with that from the pairing χ^2 based on the neutral clusters. As discussed in Section 1.3.2, the Dalitz decay tracks tend to be very close together, making them more difficult to reconstruct than well-separated tracks. Therefore, the vertex based on the tracks has a much larger uncertainty than the “neutral vertex,” based on the photon pairing, (~ 80 cm versus ~ 25 cm) and is not used.

3.5.4 *The Energy Scale*

The reconstruction of the kaon decay vertex depends on the measured photon energies (see Eq. 3.7). Recall that electrons are used to calibrate the calorimeter’s energy response (see Section 2.5.2). The combination of the small difference in the shower

profiles of electrons versus photons in the CsI blocks and the non-uniformity of the light collection in a crystal results in a slightly different calibration for photons than for electrons.

To measure the difference in the calorimeter's response to photons (relative to the response to electrons), we use decays in the regenerator beam near the downstream edge of the regenerator (as mentioned in Section 2.3). Because the effect we are measuring is small, we use the high statistics sample of $K_L \rightarrow 3\pi^0$ decays to study it. Using the surveyed position of the regenerator and the calorimeter's simulated response to photons, our Monte Carlo (described in Chapter 4) predicts the reconstructed z position of the decays; this distribution turns on sharply at the regenerator edge, as shown in Fig. 3.5. Comparing this distribution in data and Monte Carlo will reveal any remaining energy scale problem with the data calibration.

Figure 3.5 (a) shows that, initially, the regenerator edge is shifted between data and Monte Carlo. This shift corresponds to an energy scale of 0.15%; this means that for photons, the measured energy needs to be multiplied by 0.9985 for proper calibration. After applying this photon calibration to the neutral clusters in data, the data and Monte Carlo show agreement for the position of the regenerator edge, as shown in Fig. 3.5 (b).

3.5.5 *Vertex x and y Positions*

In order to reconstruct the invariant mass of the final state particles, we need to determine a four-vector for each one. With the energies and vertex z position in hand, we only need to find the x and y coordinates of the vertex. In the normalization mode, $K_L \rightarrow 3\pi^0$, this is done by assuming that the vertex is along the line between the target and the center of energy at the calorimeter. The x (y) location of the center of

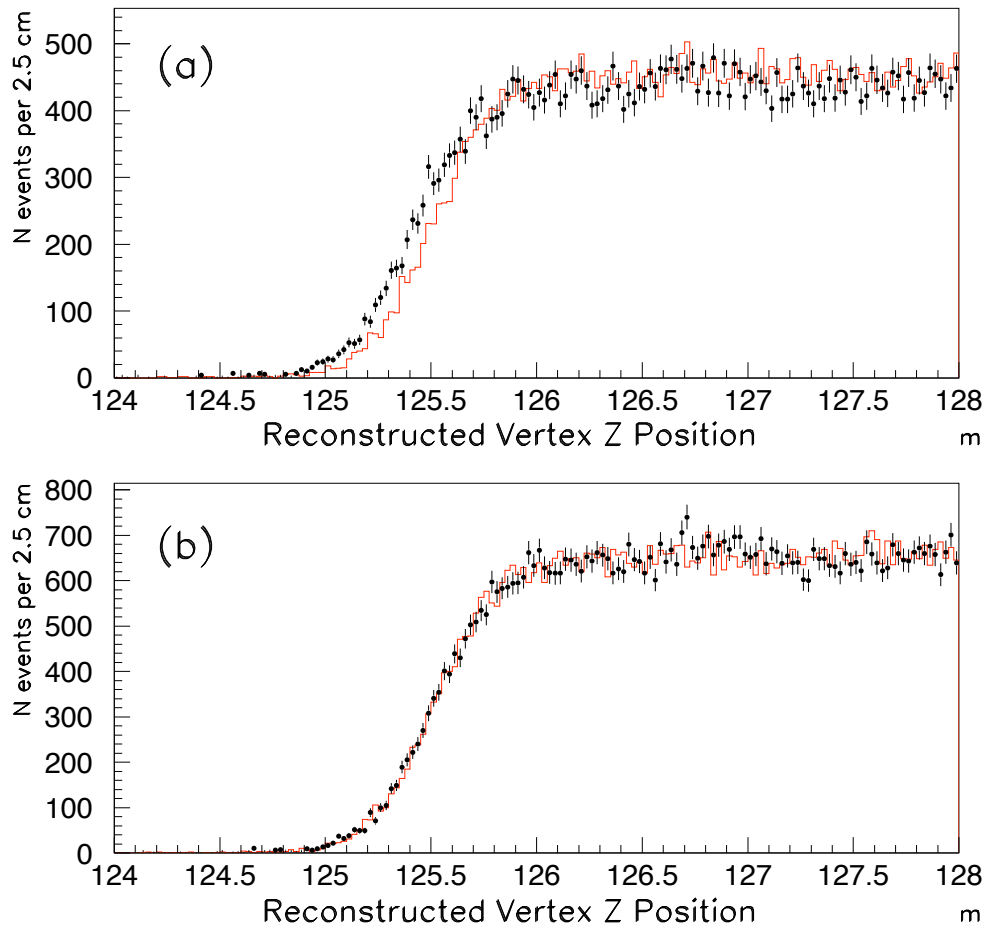


Figure 3.5: The reconstructed vertex z position for $K_L \rightarrow 3\pi^0$ decays in the regenerator beam. The dots are data and the solid histogram is Monte Carlo. The downstream end of the regenerator is located at about $z = 125.5$ m. In (a), the energy scale has not been applied, and the data-Monte Carlo mismatch is clear. In (b), an energy scale of 0.9985 has been applied to the data, and the data and Monte Carlo agree.

energy is just the average x (y) position of all the clusters, weighted by their energies. The known z position of the vertex, combined with the slope of the line between the target and the center of energy, yields the vertex x and y positions.

As an aside, the x position of the center of energy combined with the known position of the regenerator at the time of an event tells us which beam (vacuum or regenerator) the event came from. Recall that for this analysis, only vacuum beam events are used.

The signal mode, $K_L \rightarrow 3\pi_D^0$, is slightly more complicated because the electrons bend in the magnet; the center of energy at the calorimeter is not what it would have been had all the particles travelled in a straight line from the vertex. To correct for this, the upstream segments of the two tracks (the parts of the tracks found in DC1 and DC2, before bending occurs) can be projected to the calorimeter, to see where the electrons would have been had they travelled in a straight line. Replacing the true positions of the charged clusters with these two projected positions allows us to do the same weighted average of cluster positions that was done in the normalization mode to find the x and y center of energy at the calorimeter. The x and y vertex positions are found using the known z position and the center of energy, as above.

Just as the tracks can be used to find the vertex z position in the signal mode (see Section 3.5.3), the tracking algorithm also returns the x and y vertex positions. To maintain consistency between the signal and normalization modes, the x and y positions based on neutral information are used in both modes.

3.6 Reconstructing the Mass

The track-finding algorithm assumes the electron mass in order to calculate the energy-momentum four-vectors for the two tracks. The cluster energies, photon pair-

ing, and vertex position, allow us to form the four-vector for each photon. Adding the four-vectors and squaring gives the $3\pi_D^0$ and $3\pi^0$ invariant mass (squared) in the signal and normalization modes, respectively.

3.7 Selection Criteria

After vertex position and mass reconstruction, a series of quality criteria are used to select the final data samples in each mode. These criteria are listed in Table 3.1 and are described below. For quantities that exist in both signal and normalization modes, selection requirements are as similar as possible so that uncertainties associated with making the requirements largely cancel in the ratio of the two modes. This is confirmed by varying these cuts in both modes and seeing that the ratio of branching ratios does not change significantly (see Section 6.11 for a discussion of the systematic uncertainty associated with the selection requirements). For requirements on quantities appearing only in the signal mode, we vary the cut to see that the Monte Carlo matches the data well in the region of the cut.

3.7.1 Criteria Used in Both Signal and Normalization Modes

The selection criteria used in both modes include requirements designed to avoid event topologies that have poor reconstruction efficiencies and/or that are not well-simulated in the Monte Carlo (see Chapter 4), to reduce background, and to cleanly define the acceptance. We first eliminate events with extra tracks in the signal mode and events with extra hardware clusters (more than 6 or 7, in the normalization and signal mode, respectively). Since it is possible that accidental hits in the detector could have caused an event to pass the trigger requirements, we verify that the reconstructed hits satisfy the Level 1 trigger elements in each mode.

| Quantity | Selection Criteria |
|--|--------------------|
| ***Both Modes*** | Cut Window |
| Reconstructed $3\pi^0, 3\pi_D^0$ Mass (GeV/c^2) | (0.490, 0.505) |
| Reconstructed Vertex z Position (m) | (123.0, 158.0) |
| Reconstructed Kaon Energy (GeV) | (40.0, 160.) |
| Pairing χ^2 | (0.0, 75.0) |
| Shape χ^2 | (0.0, 100.0) |
| Minimum Cluster Energy (GeV) | (3.0, ∞) |
| Minimum Cluster Distance (m) | (0.075, ∞) |
| Maximum Seed Ring | (0.0, 19.0) |
| Minimum Small Ring | (4.0, ∞) |
| Minimum Pipe Fraction | (0.04, ∞) |
| Ring Number (cm^2) | (0.0, 110.0) |
| ***Dalitz Only*** | Cut Window |
| $e^+e^-\gamma$ Mass (GeV/c^2) | (0.115, 0.155) |
| Minimum Track Momentum (GeV/c) | (4.0, ∞) |
| Track E/P | (0.9, ∞) |
| Vertex χ^2 | (0.0, 100.0) |
| Track-MA distance (m) | (.003, ∞) |
| Track- V bank distance (m) | (.002, ∞) |
| Track- V' bank distance (m) | (.002, ∞) |
| Track-CA distance (m) | (.002, ∞) |
| Track-CsI distance (m) | (.029, ∞) |
| Brem- γ Distance at CSI (m) | (0.01, ∞) |
| Cell Separation (cells) | (3.0, ∞) |
| e^+e^- Mass (GeV/c^2) | (0.015, ∞) |

Table 3.1: Selection criteria for signal and normalization modes.

The reconstructed $3\pi^0$ and $3\pi_D^0$ masses are required to be within about $7 \text{ MeV}/c^2$ of the PDG value of the kaon mass, $497.6 \text{ MeV}/c^2$, to reduce combinatoric background (from mispairing the photons). The resolution on the reconstructed $3\pi^0$ ($3\pi_D^0$) mass is about 1 (2) MeV/c^2 . The reconstructed vertex z position is required to be between 123 and 158 meters, so that it is downstream of the MA and upstream of the vacuum window. The only significant background for the Dalitz decay is due to photon conversions in material. There is very little probability of conversion in the vacuum beam, but a relatively significant number of conversions occur in the vacuum window; requiring that the decay occur before the vacuum window essentially eliminates this background. The reconstructed kaon energy must be between 40 and 160 GeV. The lower bound is chosen because the detector acceptance decreases significantly for lower kaon momenta; the higher bound is chosen because it matches the energy window that has been optimized and studied for the $\text{Re}(\epsilon'/\epsilon)$ analysis. The pairing χ^2 is required to be less than 75 in both modes; along with the reconstructed mass requirements, this reduces the number of events where the photons are mispaired. The threshold of 75 removes roughly the same fraction of events in both modes (after all other requirements are applied).

There are several requirements on the clusters in the calorimeter. We want to discriminate between clusters that are photons and clusters that are either hadrons (pions) or that are a “fusion” of two particles. The shape χ^2 is a measure of how close a cluster’s transverse energy profile is to the expected transverse energy distribution for a photon shower. We require the shape χ^2 to be less than 100; this is very loose, due to the fact that the Monte Carlo (described in Chapter 4) does not model this distribution very well, as shown in Fig. 3.6. Each cluster must be greater than 3 GeV in energy, reducing the dependence on the trigger simulation. The minimum distance between any pair of clusters is 7.5 cm. This requirement decreases the sensitivity

to two things: the modelling of the transverse energy distribution and the energy correction for overlapping clusters. The maximum seed ring and minimum small ring requirements reject events where a seed block is at the outer edge of the calorimeter or at either of the beam holes, respectively. For a particle whose seed block borders an inner or outer edge of the CsI, a significant fraction of its energy will not be contained in the calorimeter; to reduce our sensitivity to how well we model this missing energy, we eliminate this type of event. The so-called “minimum pipefrac” requirement is redundant with the minimum small ring cut; the “pipe fraction” refers to the fraction of a cluster’s energy that escapes down the beam pipe for clusters with seed blocks in the first ring of crystals around either beam hole. (Since the minimum small ring requirement rejects exactly these events, we do not expect the pipefrac cut to have any effect in the nominal analysis.) We include it in the analysis to be used as a cross check when we vary the minimum small ring cut.

The x and y positions of the center of energy at the calorimeter (described in Section 3.5.5) can be used to help reduce instances where the kaon may have scattered. If the energy centroid is outside both of the beams, then we can conclude that the kaon scattered before decaying. Each beam is centered on one of the two beam holes, and is 9.3 cm square at the calorimeter. If an event’s energy centroid falls inside an area $\sim 86.5 \text{ cm}^2$ centered on either beam hole, that event is within one of the beams. For any event, we can find the area of the square which includes the center of energy on one of its edges and which is centered on the beam hole nearest that energy centroid. The area of this square is called the ring number. If Δx (Δy) is the horizontal (vertical) distance in meters between the energy centroid and the center of the nearest beam hole, then the ring number (in cm^2) is:

$$\text{ring number} = 40,000 \times \max(\Delta x^2, \Delta y^2). \quad (3.9)$$

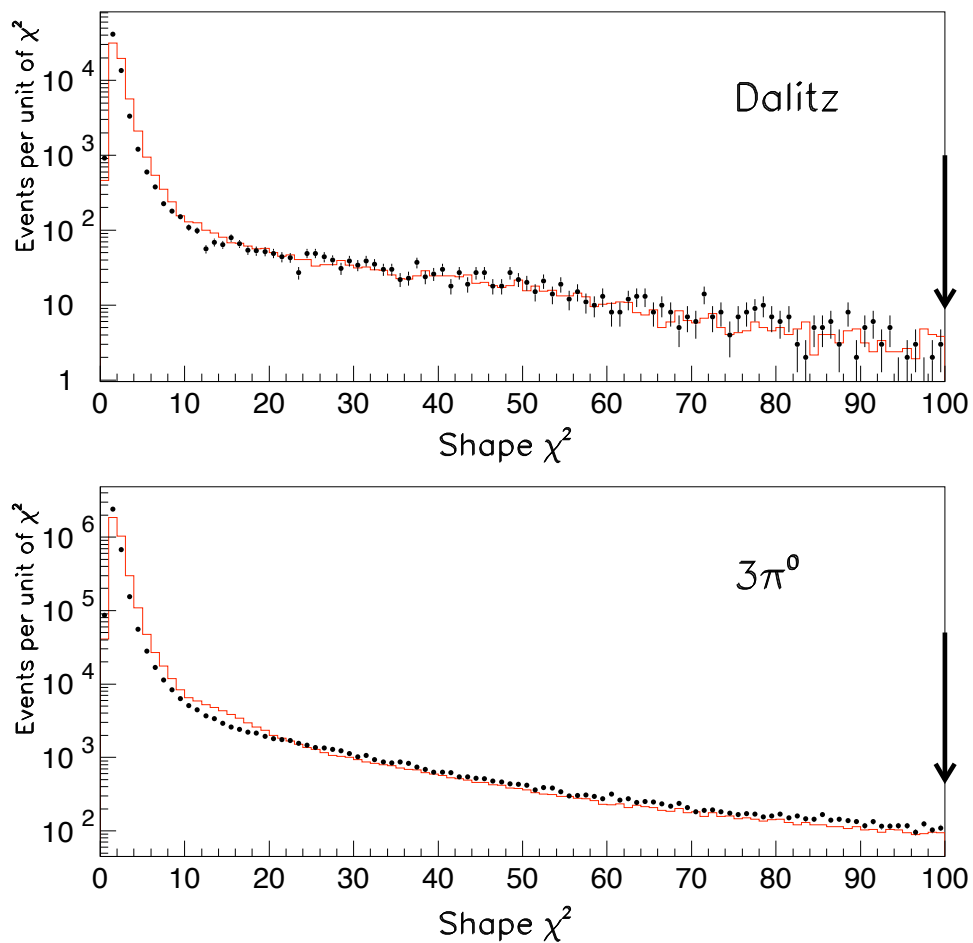


Figure 3.6: The data to Monte Carlo overlay of the shape χ^2 distribution, in both signal and normalization modes. The dots are data and the solid histogram is Monte Carlo. All selection criteria have been applied, except the one on the shape χ^2 . The arrow indicates the selection requirement of a shape χ^2 of 100 or less.

Smearing of the beam (as well as smearing during reconstruction) can result in ring numbers greater than 86.5 cm^2 ; therefore, we allow events with ring numbers up to 110 cm^2 . Although this reduces kaon scatters in our sample, it does not eliminate them; a kaon from the regenerator beam could scatter into the vacuum beam and have a low ring number. This scattering should be the same in signal and normalization modes, and cancel in the ratio. Figure 3.7 shows the ring number distribution in both signal and normalization mode in data.

3.7.2 *Criteria Unique to Signal Mode*

There are additional selection criteria for the Dalitz mode, associated with tracking and with reconstruction of the π_D^0 ($e^+e^-\gamma$). The reconstructed invariant mass of the $e^+e^-\gamma$ is required to be consistent (within $20 \text{ MeV}/c^2$) with the π^0 mass of $135 \text{ MeV}/c^2$. The resolution on the reconstructed $e^+e^-\gamma$ mass is approximately $1.5 \text{ MeV}/c^2$. Along with the requirements on the reconstructed $3\pi_D^0$ mass and the pairing χ^2 described in Section 3.7.1, this requirement reduces photon mispairings.

There are several track-quality requirements. Each track must have a minimum momentum of $4 \text{ GeV}/c$, and an energy to momentum ratio (E/p) greater than 0.9, since we have calibrated such that the E/p distribution for electrons is sharply peaked at 1.0. Figure 3.8 shows the E/p distribution for one of the tracks in data. The vertex χ^2 (see Section 3.5.5) must be less than 100 to reduce events with misreconstructed tracks. This is a fairly loose requirement, as seen in Fig. 3.9.

Additionally, there is a set of fiducial cuts on the tracks; they ensure that neither track passes too close to the MA, the VV' beam holes, the CA, or the CIA. The tracks must be at least 3 mm away from the edges of the MA, at least 2 mm away from the beam holes in the trigger hodoscope, at least 2 mm away from the CA, and

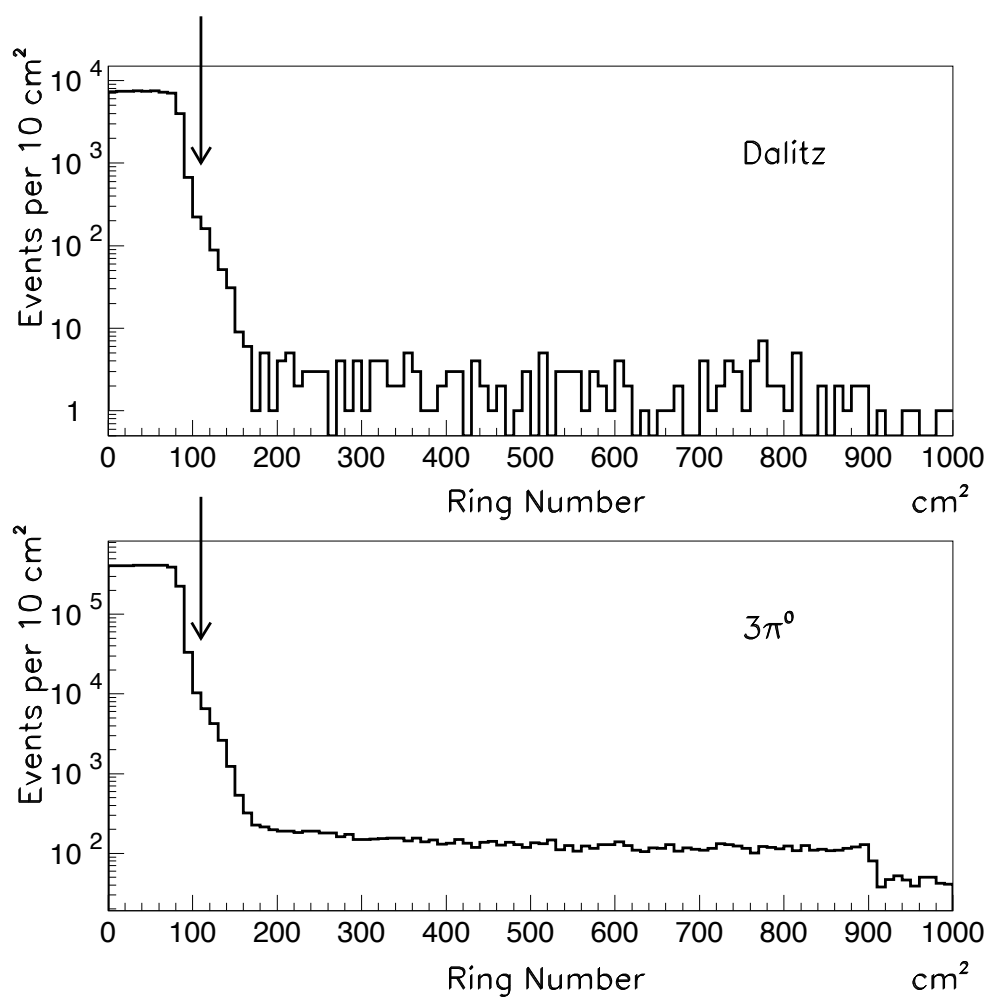


Figure 3.7: The ring number distribution in data, in both signal and normalization modes. All selection criteria have been applied, except the one on the ring number. The arrow indicates the selection requirement of a ring number of 110 or less.

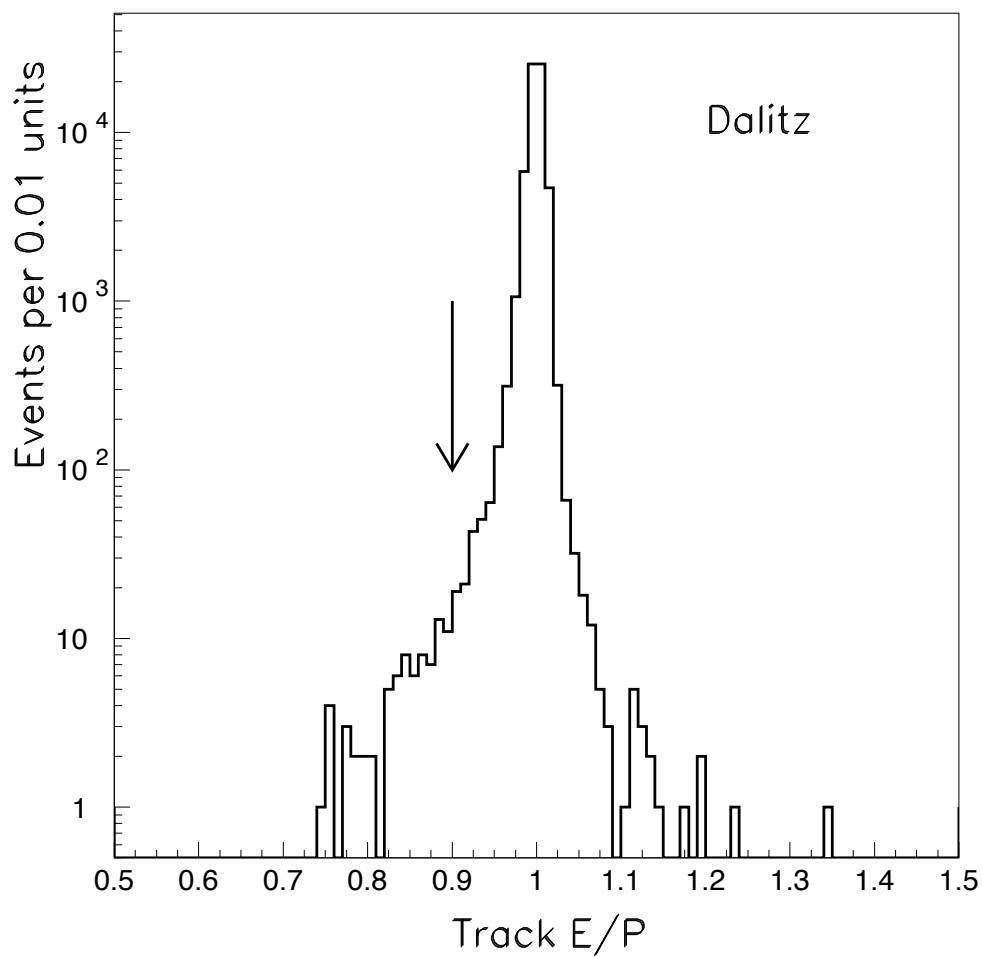


Figure 3.8: The E/p distribution for the track with the higher momentum. All selection criteria have been applied except the requirement that E/p be greater than 0.9. The arrow indicates where this cut is.

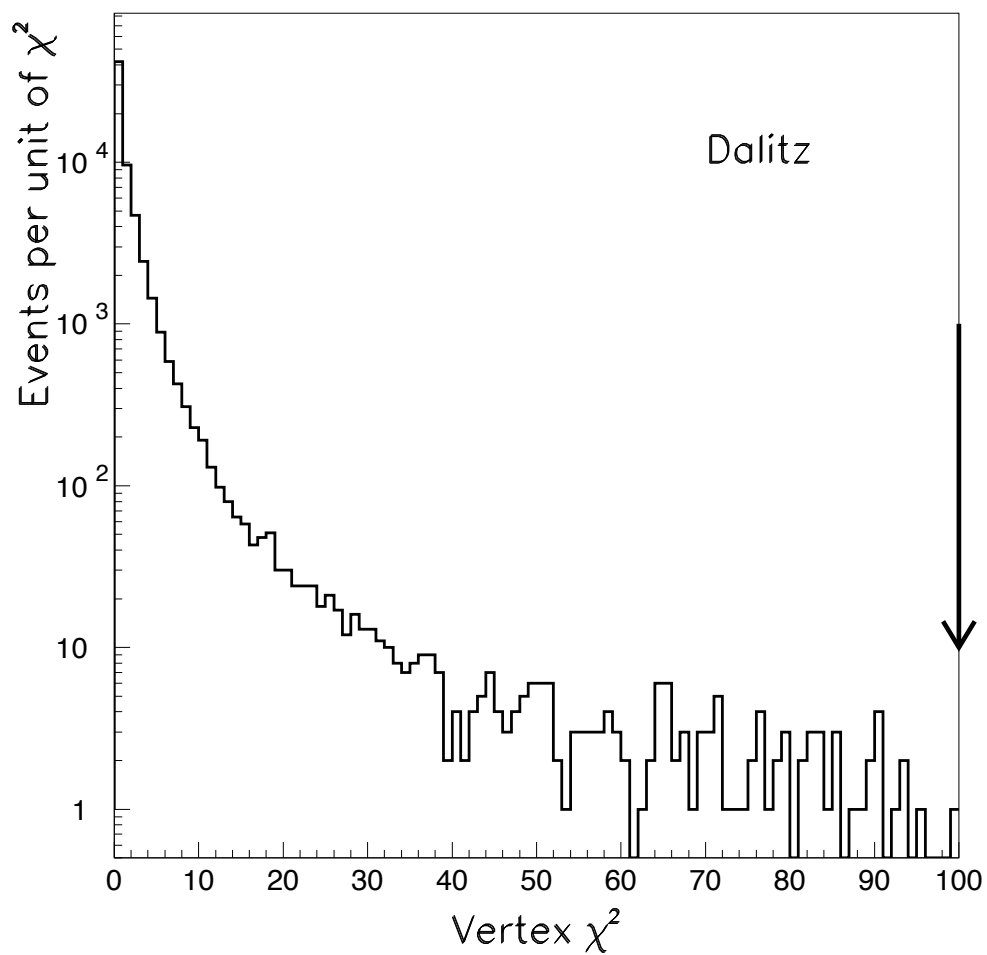


Figure 3.9: The vertex χ^2 distribution in data. All selection criteria have been applied except the requirement that the vertex χ^2 be less than 100. The arrow indicates where this cut is.

at least 2.9 cm away from the outer edges of the calorimeter [30]. These requirements reduce our sensitivity to how well we know the physical locations and dimensions of these detector components.

It is possible for an electron to emit a bremsstrahlung photon as it bends in the magnet. This “brem” photon changes the electron momentum, and can be confused with one of the final state photons, resulting in misreconstruction. To reduce these effects, we need to identify and eliminate events with a brem photon. The brem photon is typically emitted parallel to the original direction of the electron (prior to bending in the magnet); we project the upstream segment of each track to the calorimeter and find the distance to the closest photon cluster. This distance is referred to as the “brem- γ distance,” and the distribution is shown in Fig. 3.10. If the nearest photon is within 1 cm of the upstream track projection, it is likely that that photon is a brem photon and not one of the original decay products. Thus, we require the brem- γ distance to be less than 1 cm.

The final two selection criteria are related; they are the cell separation requirement and the e^+e^- mass requirement. The former requires that the tracks be separated by more than three cells in the first and second drift chambers. Each cell is 6.35 mm centered around a sense wire as shown in Fig. 3.11, so the distance requirement is around 2 cm. If two tracks are in the same drift chamber cell or in adjacent cells, then a hit from one track can obscure a hit from the other track on the same wire. This alone will not cause the tracking code to fail, unless the tracks are this close in at least three chambers or are less than 1 mm apart in any one chamber [30]; however, modelling the combination of close tracks with other complications in the drift chambers (such as accidental hits, delta rays, and high-SOD pairs) is difficult. Requiring a separation greater than three cells in the first two chambers reduces our sensitivity to the tracking simulation. Although this cut eliminates approximately

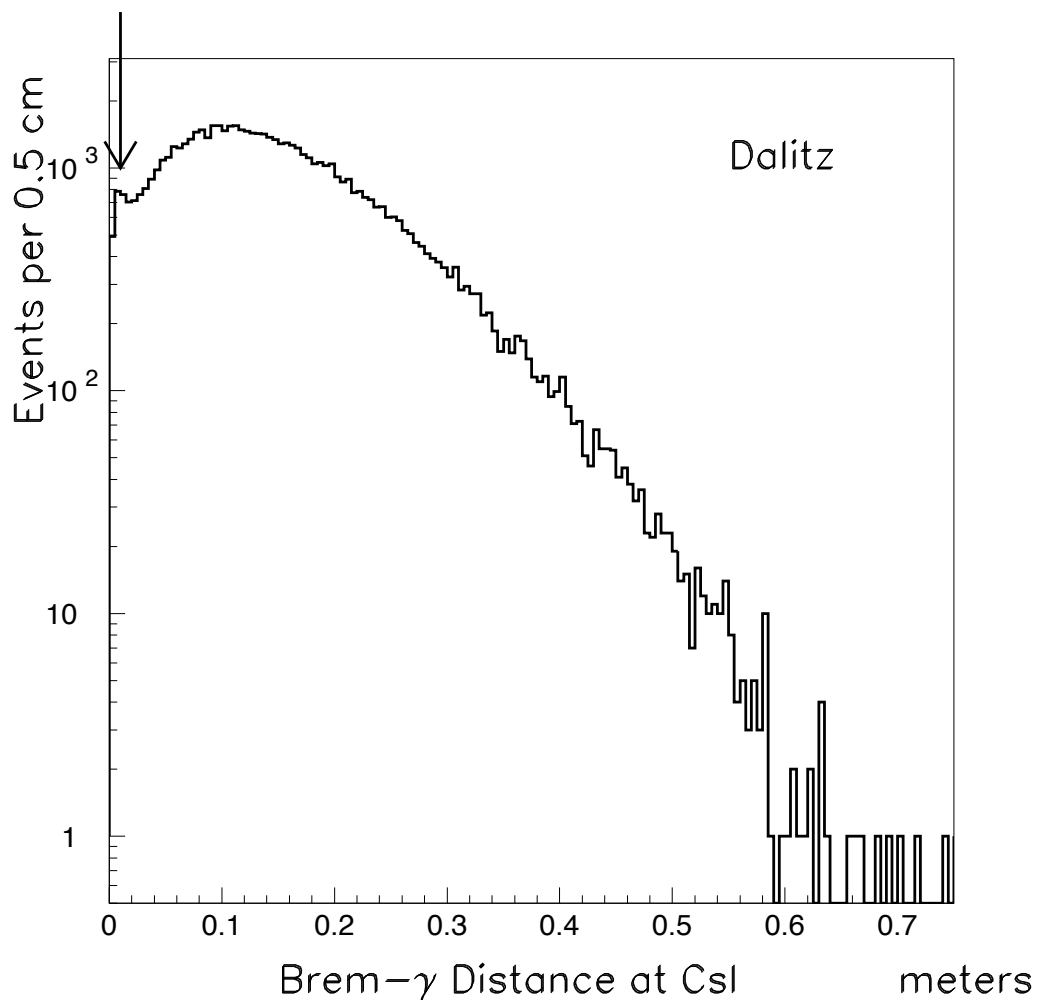


Figure 3.10: The brem- γ distance in data. The brem- γ distance is defined as the distance between the projection of the upstream track segment at the CsI and the nearest neutral cluster. All selection criteria have been applied except the requirement on the brem- γ distance; that requirement is that the brem- γ distance must be more than 1 cm, as indicated by the arrow.

Recall from Section 1.3.2 that the e^+e^- mass can also be thought of as the mass of the virtual photon in the Dalitz decay. Small values of e^+e^- mass correspond to close tracks; thus, the cell separation requirement described above eliminates most of the events with an e^+e^- mass less than $\sim 10 \text{ MeV}/c^2$. Figure 3.12 shows how the cell separation requirement affects the e^+e^- mass distribution. The analysis cut at $15 \text{ MeV}/c^2$ cleanly defines the kinematic region of our measurement, by excluding the region where the acceptance is very small.

Additionally, the low e^+e^- mass region is more sensitive to the real and virtual radiative corrections than the region above $15 \text{ MeV}/c^2$. Measuring $B(\pi^0 \rightarrow e^+e^-\gamma)/B(\pi^0 \rightarrow \gamma\gamma)$ for e^+e^- masses above $15 \text{ MeV}/c^2$ reduces our sensitivity to the theoretical predictions in the low e^+e^- mass region, and allows our measurement to be updated in the future for new predictions for radiative corrections in the low e^+e^- mass region.

3.8 Final Data Samples

Applying all of the requirements discussed in Section 3.7 leaves us with refined event samples in the signal and normalization modes. We will use these data samples, along with samples of simulated events (discussed in Chapter 4), to calculate $B(\pi^0 \rightarrow e^+e^-\gamma)/B(\pi^0 \rightarrow \gamma\gamma)$ in Chapter 5.

To “see” our final data samples, reconstructed mass plots are shown in Fig. 3.13 and Fig. 3.14 for the Dalitz and $3\pi^0$ modes, respectively. In each plot, all cuts have been applied except the cut on the quantity plotted.

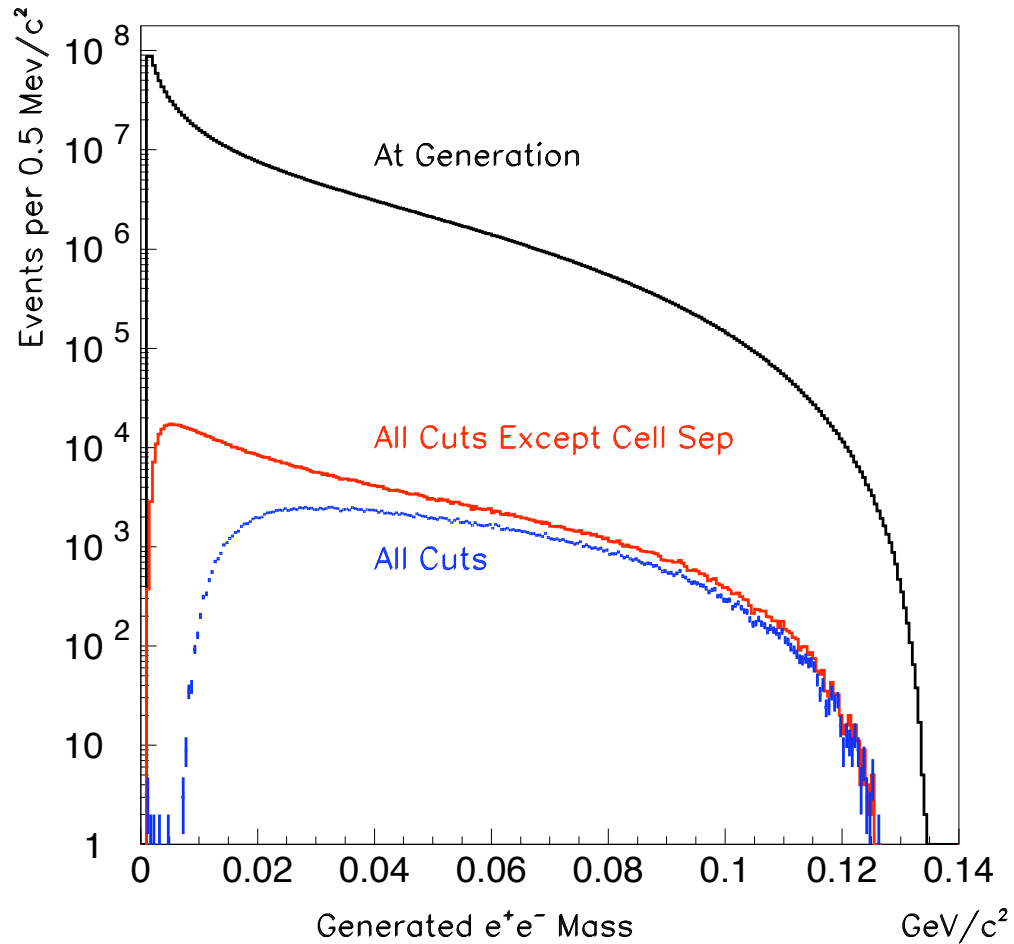


Figure 3.12: The e^+e^- mass distribution. The top line is the distribution for all generated events, the middle line is the distribution with all selection requirements except the cell separation cut (and except the requirement on the e^+e^- mass itself), and the bottom line is the e^+e^- mass distribution with all selection requirements (except that on the e^+e^- mass).

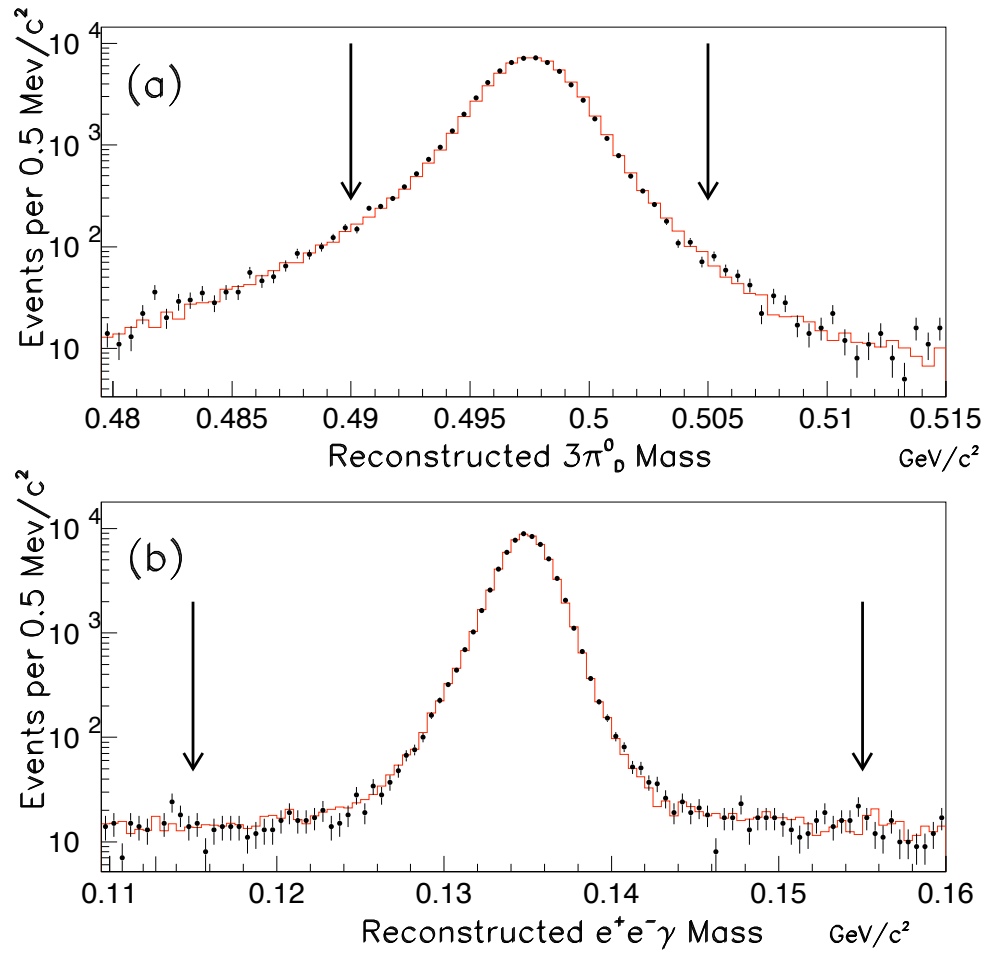


Figure 3.13: (a) The reconstructed $3\pi_D^0$ mass and (b) the reconstructed $e^+e^-\gamma$ mass in the signal (Dalitz) mode. The dots are data, and the solid histogram is Monte Carlo. All cuts have been applied except the cut on the quantity plotted.

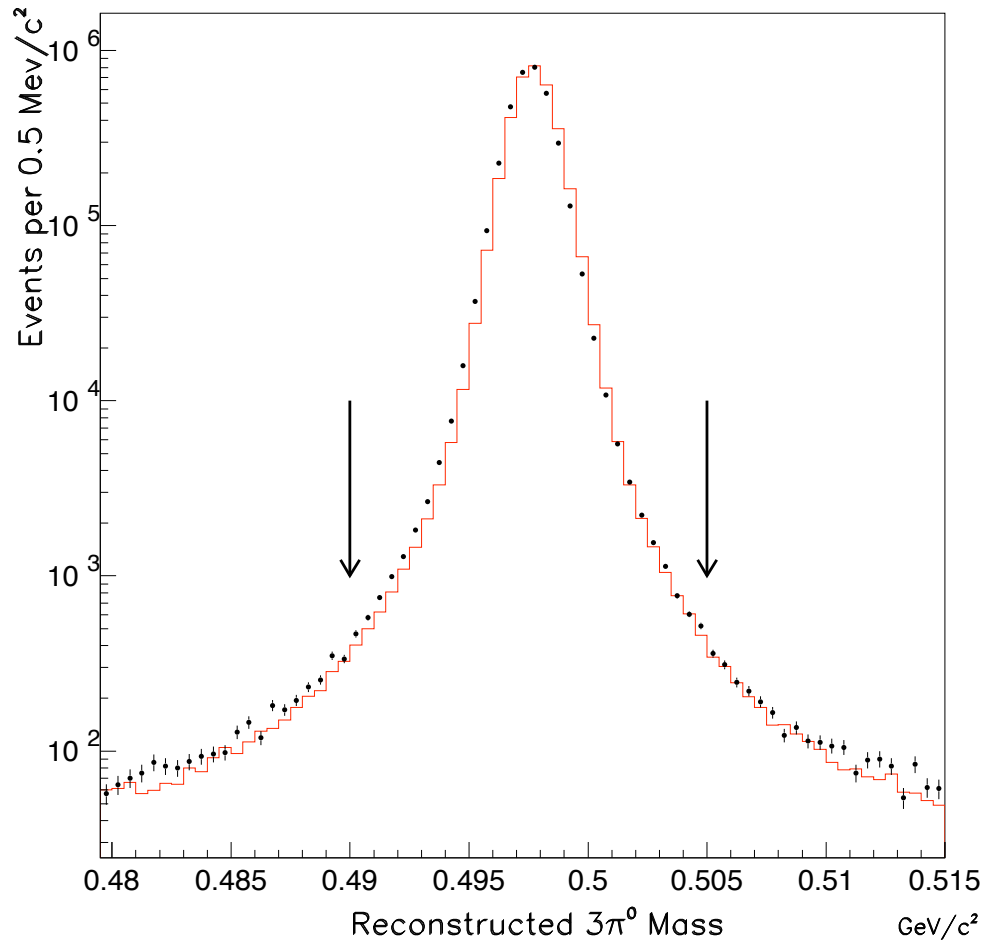


Figure 3.14: The reconstructed $3\pi^0$ mass in the normalization mode. The dots are data, and the solid histogram is Monte Carlo. All cuts have been applied except the cut on the reconstructed $3\pi^0$ mass.

CHAPTER 4

MONTE CARLO SIMULATION

This chapter provides an overview of the KTeV Monte Carlo (MC) event simulation. A more detailed description of the MC can be found in [28, 29].

4.1 Overview of Simulation

Determining a branching fraction from the observed number of events for a certain decay mode requires knowledge of the flux of parent particles as well as knowledge of the acceptance, or fraction of decays that are identified by the detector and reconstructed in the analysis. However, measuring a ratio of branching ratios using a set of data collected all at one time, as in this measurement of $B(\pi^0 \rightarrow e^+e^-\gamma)/B(\pi^0 \rightarrow \gamma\gamma)$, renders the flux of parent particles irrelevant, since it is the same between the signal and normalization modes. The acceptance for the decays $K_L \rightarrow 3\pi_D^0$ and $K_L \rightarrow 3\pi^0$ are quite different, though. We rely on our Monte Carlo simulation to determine the z -dependent acceptance in each mode.

We use version 6.03 of the KTeV Monte Carlo (the same as was used for the recent V_{us} analysis [35]) to generate signal and normalization mode events and to simulate the detector response. The Monte Carlo includes generation and propagation of the kaons; the physics of the signal and normalization mode decays (including radiative corrections for the Dalitz decay); propagation of the decay products through the detector; the detector geometry, efficiency, and response; and the effects of accidental activity in the detector. The simulated event format is essentially the same as that for data, with additional information regarding the “true” (or “generated”) value of many quantities included for studies. The data and MC events are analyzed with the same reconstruction algorithm and selection criteria (the subject of Chapter 3).

4.2 MC Beamline and Detector Geometry

The geometry of the KTeV experimental setup used by the simulation is based on both survey measurements of the physical system as well as data studies. Survey results are used for the transverse dimensions and z positions of beamline and detector components. The relative offsets among the drift chambers and the calorimeter are measured using data (see Section 2.4.2), and the MA and CA aperture locations and sizes are determined with electron samples from $K_L \rightarrow \pi^\pm e^\mp \nu$ decays.

4.3 Kaon Propagation and Decay

For each event, the MC begins by choosing a beam (vacuum or regenerator, and left or right) and an initial kaon eigenstate (K^0 or $\overline{K^0}$). The kaon energy and angle relative to the primary beam are chosen using a parametrization [36] that is adjusted to match KTeV $K \rightarrow \pi^+\pi^-$ data. The MC propagates the K^0 and $\overline{K^0}$ amplitudes along the beamline, accounting for regeneration and scattering in the absorbers and regenerator. The upstream collimators are treated as perfectly absorbing; however, scattering is allowed in the defining collimator and the regenerator, using models based on data studies.

The decay position is based on the calculated z distribution for the initial K^0 or $\overline{K^0}$ state. The range of z positions allowed for the decays is user-specified, and is slightly larger than the z range to be used in the analysis. This method is chosen to reduce CPU time, but introduces complications in the code. Weighting factors must be calculated at the beginning of the simulation to obtain the correct proportions of vacuum beam to regenerator beam coherent decays and scatters from the regenerator and collimator, all of which produce different quantum states at the beginning of the decay region [30].

Each kaon decay mode has a separate subroutine which generates the decay in the kaon rest frame. For kaon decays to π^0 s, as in this analysis, a decay mode can be specified for each π^0 . In addition to the dominant $\pi^0 \rightarrow \gamma\gamma$ decay mode, the user can choose among other options, including the Dalitz decay and rare decay modes. Once the final state particles have been generated, they are boosted into the lab frame for tracing through the detector.

The decay products undergo various interactions as the simulation traces them through the detector. Charged particles receive a transverse momentum kick from the analysis magnet; the magnitude of the kick depends on the field integral at the particle's transverse position at the midplane of the magnet. Charged particles can scatter in the vacuum window and spectrometer material. Electrons can emit bremsstrahlung photons, and photons can convert in material (such as the vacuum window), producing an e^+e^- pair; these secondary particles are also traced through the detector. When a particle hits a photon veto detector or the trigger hodoscope during tracing, the energy deposit in the counter is simulated. Tracing of a particle (except in the case of muons) ceases once it hits a photon veto counter or any passive material, when it leaves the detector volume, or when it finally hits the CsI or BA. Muons are propagated through detector material and through the steel filters and counters in the muon system. The simulation records and saves the particle positions in each drift chamber and in the calorimeter to be used later in simulating the detector response, described in the next several sections.

4.4 Accidental Overlays

Before describing the simulation of the detector response, we briefly discuss the simulation of accidental activity. Due to the high flux of kaons and neutrons, we expect

that events with real kaon decays will also contain a significant amount of unrelated activity in the detector. After the veto requirements, the average accidental energy contained in each CsI cluster is a few MeV, and there are roughly 20 extra in-time DC hits in each event [27]. Using the accidental counters (see Section 2.2.3) and a trigger designed to collect accidental events (see Section 2.7.4), we have samples of accidentals from the data. We can use these accidental samples in the MC, overlaying an accidental event on top of each simulated decay, to study the effect of the underlying activity and to take it into account in the acceptance.

Energy deposits from the accidentals are added to the energy deposits from the kaon decay in the calorimeter and in the veto system. The accidentals' effect in the drift chambers is more complicated. Although merging the hit lists is straightforward, an empirical model is needed to describe the various ways an accidental hit can obscure a signal hit on the same wire (see Section 4.5). The trigger source information is summed, and the trigger is evaluated based on the combined information.

It is important to note that the MC event generation is based on an accidental file; the accidental file specifies the run-range for the simulation and, for each run, points to accidental events collected during that run. In this way, the MC determines how many events to generate in a particular run so that longer runs containing more data will also have more MC events. The MC also decides at what beam intensity the events in a particular run should be produced based on the accidental events since the beam intensity varies over the run range. Further, the accidental event added to a simulated event comes from the same run as that simulated event, ensuring that the intensity-dependence of the underlying activity is simulated. This point is important for studying our tracking inefficiency (see Section 6.1) and for our cross check involving the intensity-dependence of our result (see Section 7.3).

4.5 Simulation of the Drift Chambers

During particle tracing, charged particle positions in each drift chamber are recorded (see Section 4.3). This information is the starting point for the drift chamber simulation. The simulation calculates a hit's distance to the closest sense wire in a given plane (see Section 2.4.2), smearing the distance based on the measured resolution for this plane, and converts the distance to a drift time using the inverse of the $x(t)$ maps (see Section 2.4.2).

Several effects observed in data were added to the MC to model sources of inefficiencies more accurately. These effects include wire inefficiency, high-SOD pairs from delayed hits, accidental hits that obscure signal hits, and low-SOD pairs from delta rays. We briefly describe each of these effects.

Each wire has an intrinsic inefficiency that can result in a missing TDC hit. The inefficiency is measured as a function of position along a wire, and as a function of the transverse distance from the wire. A model of this wire inefficiency is included in the simulation.

Recall that the inefficiency for a wire detecting a single drift electron can result in high-SOD pairs (see Section 3.4.1) because the signal on the sense wire is delayed. If the SOD is more than 1 mm too high, the hit-pair is not accepted. The probability for such a delayed hit varies as a function of transverse location in a chamber, with the highest probability near where the neutral beams pass through the chamber. A map of this spatial dependence is included in the simulation. The delayed-hit probability also depends on the track position within a cell, with higher probability for tracks close to the sense wire. Additionally, the probability changed over time during data-taking. The simulation mimics this variation using the run number of an event.

As noted in Section 4.4, if an in-time accidental hit reaches a sense wire before

the signal hit, the signal hit will not be recorded, since only the first hit in the in-time window is used. This results in underestimation of the drift time, leading to a low-SOD pair. If the SOD is more than 1 mm too low, the hit-pair is not accepted. Early accidental hits on a wire can also affect an in-time signal hit on that wire in two ways. First, the discriminator has a deadtime of 42 ns, during which no hit can be detected. Second, large signals can remain above the discriminator threshold for longer than 42 ns; this effect is modelled and tuned to data.

In Section 3.4.1, we discussed how delta rays can result in low-SOD pairs. The MC simulation creates delta rays in the same cell as the track, and the rate is tuned so that the low-SOD distribution matches data.

4.6 Simulation of the CsI Calorimeter

The CsI calorimeter can measure electromagnetic energies and positions very precisely. In order to take full advantage of this precision, we need to understand the detector's response and possible systematic effects in great detail; this requires a very accurate simulation of the calorimeter. The simulation is especially important to model the energy leakage (in the beam holes and at the outer edge of the calorimeter) and to model the way nearby clusters share energy.

Because electromagnetic showers involve thousands of particles, the time needed to simulate each one every time the MC runs is prohibitive. The simulation therefore relies on a shower library created using the GEANT package [37]. GEANT simulates all relevant processes in the crystals and tracks all shower particles down to a few MeV. The shower library contains photons and electrons generated at six different energies (2, 4, 8, 16, 32, and 64 GeV) and at 325 different positions on the face of the central crystal. For each shower, the library contains the energy deposited in a 13×13

array of small blocks (which can be converted to the equivalent array of large blocks depending on the cluster location in the calorimeter), the longitudinal profile of the energy deposit for the central 7×7 array (collectively), and the longitudinal energy profile for the four blocks with the most energy (individually). There is a separate library of pion showers (which are sometimes just minimum-ionizing energy deposits) generated with GEANT using the FLUKA package for hadronic interactions. The pion showers are not used in this analysis, but they play a role in the tracking efficiency studies discussed in Section 6.1.

For each decay product that hits the CsI, the simulation chooses a shower from the library based on particle type, energy, and position in the central crystal. The simulation “interpolates” between the discrete shower energies available in the library by randomly selecting a shower using weights calculated from the logarithms of the energies. Next, block-by-block scaling is done based on the ratio of the incident particle energy to the shower’s generated energy. Some of the particle’s energy will be outside the 13×13 array of crystals included in each shower. To account for this, a GEANT-based parametrization models energy deposits in a 27×27 array. To reproduce the nonlinearities in the CsI energy resolution, the longitudinal energy profile is convolved with the longitudinal light collection efficiencies for each crystal near the center of the shower.

To simulate digitization, the light output for each crystal is given a time profile and divided into DPMT time slices. The signal in each slice is smeared according to photostatistics, and then digitized with code that mimics the behavior of the DPMTs (using the inverse of the calibrations obtained from data). Just as in data, the sum of four consecutive DPMT time slices must be at least six counts above pedestal in order to be read out [30].

4.7 Simulation of the Veto Counters

As mentioned in Section 4.3, when a particle hits a photon veto detector, the energy deposit is simulated using an energy-dependent Gaussian resolution parametrized from the data. For minimum-ionizing particles, the resolution is fixed, but varies among counters (from 30% to 40%) [30].

In the muon system, muons going through the steel filters lose energy according to Bethe-Bloch ionization loss, with Landau fluctuations from a GEANT-based parametrization. If a muon does not stop in the steel, it will reach the muon veto counters in the simulation.

4.8 Simulation of the Trigger

The Monte Carlo simulates all three levels of the trigger. The gaps between counters in the VV' banks are measured using the $K_L \rightarrow \pi^\pm e^\mp \nu$ sample, to simulate the hodoscope inefficiency for charged modes. Simulation of the hit-counting in the drift chambers (DC12) as well as y track finding (1HCY) (see Section 3.2.2) is based on digital information from the chambers. Simulation of the Energy-Total and HCC systems for the calorimeter information is sensitive to the modelling of the analog turn-on thresholds for HCC bits. We use $K_L \rightarrow \pi^\pm e^\mp \nu$ decays to measure the positions and widths of these thresholds. The Monte Carlo trigger decision uses the same trigger definition files (see Section 2.7.4) as were used during data-taking.

4.9 Aspects of the Simulation Important for this Analysis

The simulation of $K_L \rightarrow 3\pi_D^0$ decays uses the basic MC version 6.03 package, with a few modifications. The “unsmearing” routine developed for version 7.00 of the KTeV

MC was imported and is used to correct the position resolution of neutral clusters. The radiative corrections routines developed by the University of Colorado group (based on [12]) are used in generating the $\pi^0 \rightarrow e^+e^-\gamma$ decay. The following two sections describe the unsmearing routine and implementation of radiative corrections. Additionally, the ring counters (RC6-RC10) were added in veto to the trigger file for the simulation of both modes; since we require these counters to be silent in the analysis, adding them to the trigger saves computing time for the simulation.

4.9.1 Unsmearing the Cluster Positions

Typically, one has to smear simulated quantities to correct for effects that have not been well-modelled so that the MC resolution matches data. In the KTeV Monte Carlo, the simulated position resolution for neutral clusters was found to be worse than the position resolution in data. To fix this, we add an unsmearing routine to make the MC position resolution better, with the unsmearing factor determined by comparison with data.

For MC events, the routine (called SMEAR_MCRECPOS) takes the neutral clusters and first attempts to match up the reconstructed clusters to the generated (true) clusters based on energies and calorimeter positions. If the matching procedure encounters difficulty, the routine returns without changing the cluster positions. If matching is successful, each cluster's x and y positions at the CsI are moved toward the generated position by an amount that depends on the (user-supplied) unsmearing factor. The unsmearing factor is chosen so that the data and Monte Carlo position resolutions agree.

The routine then performs a logical check: if the new position is in a block that is different from the cluster's seed block, the routine returns without doing anything.

The seed is, by definition, the block with the most energy, so logically the cluster position should be within the seed block; we don't want to move the cluster position outside of its seed block. If the new x and y positions are within the cluster's seed block, then we keep these new positions for the cluster. Reconstruction of the vertex z position and mass proceed as usual with these modified positions.

4.9.2 Radiative Corrections to the Dalitz Decay

Simulation of both $K_L \rightarrow 3\pi_D^0$ and $K_L \rightarrow 3\pi^0$ decays begins by producing three pions in the kaon center of mass frame based on a flat three-body phase space and forcing the pions to decay immediately. Two of the π^0 s are allowed to decay into $\gamma\gamma$, while a special routine (PI0DAL) is called for the Dalitz decay of the remaining π^0 . This routine chooses one of three options, depending on user input: $\pi^0 \rightarrow e^+e^-\gamma$ with full radiative corrections (including the real radiative corrections, $\pi^0 \rightarrow e^+e^-\gamma\gamma$), $\pi^0 \rightarrow e^+e^-\gamma$ with no radiative corrections, or $\pi^0 \rightarrow e^+e^-\gamma\gamma$ only. For the nominal analysis, we use the first option to generate $\pi^0 \rightarrow e^+e^-\gamma$ with both real and virtual radiative corrections. The other options are used to study potential systematic effects due to radiative corrections (see Section 6.2).

The Monte Carlo simulation of the $\pi^0 \rightarrow e^+e^-\gamma$ decay with radiative corrections is based on the 1972 Mikaelian and Smith paper [12] discussed in Section 1.3.3. QED processes up to second order in α_{EM} are included in the corrections. This includes the virtual corrections shown in Fig. 1.3 (one-loop terms that interfere with the tree-level diagram) and the real corrections shown in Fig. 1.4.

In the case of real corrections, the radiated photon can, in principle, have any value for its energy. However, for simulation, we need to specify an energy threshold for the real radiated photon. This is achieved by generating real radiative events

($\pi^0 \rightarrow e^+e^-\gamma\gamma$) for $m_{\gamma\gamma}$ greater than 1 MeV. Below this threshold, the real radiative process is indistinguishable (in the KTeV detector) from the tree-level process, $\pi^0 \rightarrow e^+e^-\gamma$. This results in a probability of 16.18% for $\pi^0 \rightarrow e^+e^-\gamma\gamma$ to occur instead of $\pi^0 \rightarrow e^+e^-\gamma$.

The MC simulates a $\pi^0 \rightarrow e^+e^-\gamma\gamma$ decay by choosing $m_{\gamma\gamma}$ and $m_{e^+e^-}$ within kinematic limits, and then choosing whether to continue the simulation of that event based on a calculated phase space weight. If simulation continues, the $\gamma\gamma$ and e^+e^- systems are each given a momentum and a direction. From there, the simulation computes the four-momentum of each photon in the $\gamma\gamma$ frame and the four-momenta of the electron and positron in the e^+e^- frame. Each four-momentum is boosted to the pion center of mass frame. The center of mass vectors are rotated to arbitrary directions, and all decay products are boosted into the lab frame.

In the case of virtual corrections (i.e., the other $\sim 84\%$ of the decays), the simulation chooses values for the Kroll-Wada x and y variables, which are the e^+e^- mass squared as a fraction of the π^0 mass squared and the energy partition between the electron and positron, respectively (recall Eq. 1.6 and Eq. 1.11 from Section 1.3.2). A two-dimensional look-up table binned in x and y contains the correction factor for decays over the range of possible x and y values. This table is based on Mikaelian and Smith's calculations of the radiative corrections to the differential decay rate [12], as discussed in Section 1.3.3, and was implemented in the KTeV MC by the University of Colorado group. The tree-level rate is calculated, and the appropriate radiative correction factor from the table is applied.

Next, the form factor correction is applied. Recall from Section 1.3.1 that the pion's internal structure necessitates an electromagnetic transition form factor to describe the $\pi^0\gamma\gamma$ vertex. Also recall from Section 1.3.2 that, for the Dalitz decay, the form factor only depends on x ($x = m_{e^+e^-}^2/m_{\pi^0}^2$). We can approximate the form

factor as $f(x) \approx (1 + ax)$ where a is the π^0 slope parameter. The MC uses the 2006 PDG [4] average of 0.032 ± 0.004 for the slope parameter. We consider the systematic uncertainty related to the form factor in Section 6.8.

Finally, as in the case of real radiative corrections, the MC chooses whether to continue the simulation of the event based on a phase space weight. If simulation continues, the three decay products are given four-momenta in the pion frame. The center of mass vectors are rotated to an arbitrary orientation and boosted into the lab frame for tracing through the detector.

4.10 Background Simulation

The Monte Carlo is also used to estimate the background levels for this analysis. The only potential background for the Dalitz decay is from photons converting in material to e^+e^- pairs. Since the vacuum window is the only significant source of material in the decay volume, we expect most photon conversion to occur at the vacuum window. Since the z -range in our analysis is 123 to 158 meters, ending 1 meter upstream of the vacuum window (at $z = 159$ m), we expect very little background in our sample.

As noted in Section 4.3, the Monte Carlo can simulate photon conversions. To obtain a sample of background events, $3\pi^0$ events are generated using trigger 14. Because of the tracking requirements and the requirement of seven CsI clusters in trigger 14, the resulting event sample contains $3\pi^0$ events in which one of the photons has converted to an e^+e^- pair. The Dalitz analysis code is used to analyze the event sample. In Section 6.10, we describe how this allows us to estimate how many background events are in our Dalitz sample. In short, this study confirms that conversions produce negligible background, such that background subtraction is unnecessary.

CHAPTER 5

RESULTS

This chapter presents the number of reconstructed events in the signal mode and in the normalization mode in both data and Monte Carlo. The final data samples contain 63,693 Dalitz decays and 3,529,065 $3\pi^0$ decays, and the MC samples contain 265,901 reconstructed Dalitz events and 12,668,419 reconstructed $3\pi^0$ events. Table 5.1 summarizes these findings. We then calculate the acceptance using the MC results and determine $B(\pi^0 \rightarrow e^+e^-\gamma)/B(\pi^0 \rightarrow \gamma\gamma)$.

| Mode | Data Events | MC Reconstructed | MC Generated |
|----------|-------------|------------------|--------------|
| $3\pi^0$ | 3,529,065 | 12,668,419 | 334,675,893 |
| Dalitz | 63,693 | 265,901 | 226,985,152 |

Table 5.1: Number of events reconstructed in data and Monte Carlo and number of events generated in Monte Carlo for both signal and normalization decay modes.

5.1 Monte Carlo Acceptance

The acceptance is defined as the number of simulated events that pass all analysis requirements as a fraction of the number of events generated:

$$\text{acceptance} = \frac{\text{number of events reconstructed}}{\text{number of events generated}}, \quad (5.1)$$

where the only generated events that count are those within our kinematic range. In both decay modes, the kaon z range is (123, 158) meters and the kaon energy range is (40, 160) GeV, as discussed in Section 3.7.1. Additionally, in the signal mode, our kinematic range includes events with e^+e^- masses greater than 15 MeV/ c^2 (see Section 3.7.2).

It is possible for events with a true decay position (or kaon energy) that is just outside the range we select to be reconstructed just within our range, due to resolution effects. This is possible in both the data and in the Monte Carlo. To be sure we simulate this “migration,” we generate events in larger kinematic ranges than the ranges we intend to use, as mentioned in Section 4.3. Specifically, we generate kaons in a z range of (110, 161) meters and an energy range of (35, 165) in both modes; in the signal mode, we generate events with e^+e^- -masses down to 0 MeV/ c^2 . Additionally, the event generation for both modes is based on a single accidental file (see Section 4.4), ensuring that the two MC samples correspond to the same set of runs. The number of events generated in our kinematic range in the $3\pi^0$ simulation is 334,675,893, and the number in the Dalitz simulation is 226,985,152.

The Monte Carlo simulates the physics of the decays and the detector response as described in Chapter 4, and the events are analyzed with the same analysis code as the data as described in Chapter 3. In the normalization mode, 12,668,419 $3\pi^0$ events pass all selection requirements (this is equivalent to ~ 3.6 datasets). In the signal mode, 265,901 Dalitz events (~ 4.2 datasets) pass all selection requirements.

With the relevant numbers in hand, we can now calculate the acceptance in each mode according to Eq. 5.1.

$$\text{acceptance}_{\text{Dalitz}} = \frac{265,901}{226,985,152} = (1.1714 \pm 0.0023) \times 10^{-3} \quad (5.2)$$

$$\text{acceptance}_{3\pi^0} = \frac{12,668,419}{334,675,893} = (3.7853 \pm 0.0010) \times 10^{-2} \quad (5.3)$$

5.2 Corrections to the MC Acceptance

The signal mode acceptance is what allows us to determine the number of Dalitz decays that occurred during data-taking from the number we observe via our detector and reconstruction code. Because we rely on the simulation to measure the acceptance, the acceptance needs to be corrected for any differences between data and Monte Carlo.

As part of our systematic studies (the subject of Chapter 6), we have investigated possible sources of data-Monte Carlo discrepancies. We find two such discrepancies that are significant enough in magnitude to warrant a correction to the acceptance. The first is related to the tracking inefficiency in the signal mode, and the second is related to the relative trigger inefficiencies between the two decay modes; the details of each of these studies are discussed in Section 6.1 and Section 6.5, respectively. Here, we will explain each one conceptually and correct the acceptance in the signal mode for these effects.

5.2.1 Tracking Inefficiency Correction

In order to look for possible data-Monte Carlo discrepancies, we need to use event samples that are separate from our signal and normalization mode samples. Using a sample of $K_L \rightarrow \pi^+\pi^-\pi^0$ decays, we can cleanly identify cases when a track existed in the spectrometer but was not reconstructed by the tracking algorithm. Comparing the frequency of this tracking failure in data to that in Monte Carlo, we find that the Monte Carlo underestimates the tracking inefficiency by 0.68%. Because the Monte Carlo essentially reconstructs tracks too well (compared to data), the acceptance in the simulation is higher than the true acceptance. To correct this, we multiply the MC acceptance for Dalitz events by $(1 - 0.68\%)$, or 0.9932.

5.2.2 *Trigger Inefficiency Correction*

The true acceptance in each mode is sensitive to the trigger efficiency for that mode. Trigger inefficiencies can occur during data-taking due to hardware failures or electronic glitches in the trigger system. If trigger 6 and trigger 14 have different inefficiencies, and if these inefficiencies are not simulated, the ratio of signal to normalization mode acceptances measured in MC will differ from the true ratio.

In order to study relative trigger inefficiencies, we need a sample of events that have a chance of passing both triggers; thus, neither of our nominal samples can be used. However, recall that random accepts are events that are kept during the software stage of the trigger regardless of the Level 3 decision (see Section 2.7.5). We use the sample of random accepts from trigger 6 to measure the relative trigger inefficiency in data by analyzing this sample for Dalitz decays. If any of the trigger 6 random accepts are reconstructed as Dalitz decays, but are not tagged as belonging to the trigger 14 sample, there is a relative trigger inefficiency between triggers 6 and 14. We measure this inefficiency to be 0.14%. (Note that any absolute inefficiency in trigger 6 will also affect our measurement; in Section 6.6, we find the magnitude of this inefficiency to be negligible.)

We find that the Monte Carlo does not mimic the relative trigger inefficiency found in data; therefore, the signal mode acceptance will be too high (if the MC exactly modelled reality, some of the simulated events would have been accidentally thrown out by trigger 14, reducing the final MC sample). To correct this, we multiply the acceptance for Dalitz events by $(1 - 0.14\%)$, or 0.9986.

5.2.3 Corrected Acceptances

Based on these tracking and trigger inefficiency studies, we can correct the Dalitz mode acceptance that we calculated in Section 5.1 by multiplying the raw Dalitz acceptance by the tracking inefficiency correction and the trigger inefficiency correction. We find

$$\text{corrected acceptance}_{\text{Dalitz}} = \left((1.1714 \pm 0.0023) \times 10^{-3} \right) \times 0.9932 \times 0.9986, \quad (5.4)$$

$$\text{corrected acceptance}_{\text{Dalitz}} = (1.1619 \pm 0.0023) \times 10^{-3}. \quad (5.5)$$

Table 5.2 gives the acceptances in the two decay modes, with the Dalitz mode acceptance corrected for the inefficiencies related to the tracking and the trigger. We will use these acceptances in the calculation of $B(\pi^0 \rightarrow e^+e^-\gamma)/B(\pi^0 \rightarrow \gamma\gamma)$.

| Mode | Corrected MC Acceptance ($\times 10^{-2}$) | Error ($\times 10^{-2}$) |
|----------|--|-------------------------------|
| $3\pi^0$ | 3.7853 | 0.0010 |
| Dalitz | 0.11619 | 0.00023 |

Table 5.2: The Monte Carlo acceptances (with uncertainties) for both normalization ($3\pi^0$) and signal (Dalitz) modes. The Dalitz mode acceptance has been corrected for the tracking and trigger inefficiencies as described in the text.

5.3 Calculation of $B(\pi^0 \rightarrow e^+e^-\gamma)/B(\pi^0 \rightarrow \gamma\gamma)$

We now have the observed numbers of events and acceptances for our signal mode, $K_L \rightarrow 3\pi_D^0$, and for our normalization mode, $K_L \rightarrow 3\pi^0$. There are several simple steps to get from these numbers to $B(\pi^0 \rightarrow e^+e^-\gamma)/B(\pi^0 \rightarrow \gamma\gamma)$. We observe (with the detector and our reconstruction) only a fraction of the Dalitz decays that occur during the data-taking period. The acceptance tells us what this fraction is; in fact,

for this reason, the acceptance is often referred to as an efficiency. Then, dividing the number of Dalitz decay events we observe in data by the acceptance we find using our MC gives us the number of Dalitz decays that actually occurred during data taking.

Similarly, we can find the number of $3\pi^0$ events that occurred during data-taking by dividing the number we find in data by the acceptance; however, in this case, one more step is necessary. At both the trigger-level and at the crunch-level, we prescaled the $3\pi^0$ events to avoid analyzing the entire data sample. The trigger prescale was 5 (see Section 2.7.4 and Section 2.7.5) and the prescale in the crunch job was 10 (see Section 3.3). Therefore, our sample contains 1/50 of the $3\pi^0$ events that were produced in the detector during the data-taking period under consideration. Since the simulation does not include any prescales, we need to correct for this by multiplying the number of $3\pi^0$ data events by 50.

The final adjustment we need to make is to translate between the $K_L \rightarrow 3\pi^0 \rightarrow 6\gamma$ decays and $K_L \rightarrow 3\pi^0 \rightarrow \gamma\gamma \gamma\gamma e^+e^-\gamma$ decays in our samples to a measurement of $B(\pi^0 \rightarrow e^+e^-\gamma)/B(\pi^0 \rightarrow \gamma\gamma)$. We only need to note that, in the signal mode, once the kaon decays into three π^0 s, any one of the three pions can undergo the Dalitz decay. Since we care about the probability of a single pion undergoing the Dalitz decay, we need to divide the number of $K_L \rightarrow 3\pi^0_D$ events by 3. In Eq. 5.6, we give the general expression for finding $B(\pi^0 \rightarrow e^+e^-\gamma)/B(\pi^0 \rightarrow \gamma\gamma)$ and, in the following equations substitute the appropriate numbers into the expression to arrive at our result:

$$\begin{aligned} & \frac{B(\pi^0 \rightarrow e^+e^-\gamma, m_{e^+e^-} > 15\text{MeV}/c^2)}{B(\pi^0 \rightarrow \gamma\gamma)} \\ &= \frac{\# K_L \rightarrow 3\pi^0_D \text{ data events}}{\text{acceptance}_{\text{Dalitz}}} \left(\frac{1}{3}\right) \frac{\text{acceptance}_{3\pi^0}}{\# K_L \rightarrow 3\pi^0 \text{ data events}} \left(\frac{1}{50}\right) \end{aligned} \quad (5.6)$$

$$= \frac{63,693}{0.0011619} \left(\frac{1}{3} \right) \frac{0.037853}{3,529,065} \left(\frac{1}{50} \right) \quad (5.7)$$

$$= (3.920 \pm 0.016) \times 10^{-3}. \quad (5.8)$$

We have included the statistical uncertainty of 0.40% from data in the result in Eq. 5.8; the next chapter explores sources of systematic uncertainty.

CHAPTER 6

SYSTEMATIC UNCERTAINTIES

Table 6.1 is a summary of the sources of systematic uncertainty for the measurement of $B(\pi^0 \rightarrow e^+e^-\gamma)/B(\pi^0 \rightarrow \gamma\gamma)$. For each line in the table, there is a subsection below giving more details describing the source of the error and how the estimate of the uncertainty was obtained. Most of the sources of error are related to the uncertainty in our simulation of the relative acceptance. The total systematic uncertainty on the ratio of branching ratios is 0.93%.

| Source of Systematic Error | Level of Uncertainty |
|-------------------------------|----------------------|
| Tracking Inefficiency | 0.68% |
| Radiative Corrections | 0.29% |
| Detector Material | 0.47% |
| Accidentals | 0.13% |
| Relative Trigger Inefficiency | 0.14% |
| Trigger 6 Inefficiency | < 0.01% |
| Trigger 6 Prescale | 0.02% |
| Form Factor | 0.06% |
| Photon Inefficiency | 0.01% |
| Background | < 0.01% |
| Cut Variations | 0.10% |
| e^+e^- mass scale | 0.06% |
| Monte Carlo Statistics | 0.20% |
| Total Systematic Error | 0.93% |

Table 6.1: Summary of systematic errors.

6.1 Tracking Inefficiency

In Section 5.2, we made a correction to the acceptance in the signal mode due to different tracking inefficiencies in data and Monte Carlo. This section describes how we arrive at the correction factor.

In KTeV's V_{us} analysis [35], a data-MC tracking inefficiency difference was measured using $K_L \rightarrow \pi^+\pi^-\pi^0$ decays in 1997 data. Since our measurement uses 1999 data, we repeat the tracking studies using 1999 $K_L \rightarrow \pi^+\pi^-\pi^0$ events. The 1999 sample may have a different inefficiency than the 1997 sample because the two years took data with different beam intensities, and tracking inefficiency varies with beam intensity. Further, two different beam intensities were used in the nominal 1999 data, so we perform the study separately on each of the so-called “medium” and “high” intensity samples.

$K_L \rightarrow \pi^+\pi^-\pi^0$ events are used in the study because it is possible to reconstruct this decay even if some of the tracking information is missing. The data sample is from random accepts in trigger 4 (trigger 4 requires four clusters and has no tracking requirement), and a large MC sample of $K_L \rightarrow \pi^+\pi^-\pi^0$ events is generated for comparison with these data events. The two charged pions should leave two tracks in the detector, but detector inefficiencies or failures of the tracking algorithm can result in single- or double-track loss. We denote the single-track inefficiency η_1 and the two-track inefficiency η_0 .

To measure the single-track inefficiency, η_1 , the $\pi^0 \rightarrow \gamma\gamma$ decay is reconstructed and two hadronic clusters (corresponding to the π^+ and π^-) are required in the calorimeter. The shape χ^2 variable described in Section 3.7.1 is used to distinguish hadronic clusters from photons. One of the hadronic clusters must match a fully-reconstructed track. There are then two possible kinematic solutions for the missing track. The position of the second hadronic cluster discriminates between these two solutions. The single-track inefficiency is measured in data and in Monte Carlo, and is multiplied by 2 since either one of our two tracks could be lost. As shown in Table 6.2, the MC does not fully model the inefficiency observed in data, so we need a correction equal to the difference between the data and MC inefficiencies. (As

described in Section 5.2, this correction will lower the acceptance, since it increases the MC tracking inefficiency to match the data inefficiency.)

Since correlated hit losses within a drift chamber can result in no reconstructed tracks, a separate study analyzes this two-track loss, η_0 . Again, we start with a reconstructed $\pi^0 \rightarrow \gamma\gamma$ and two hadronic clusters in the calorimeter. We look for events where no tracks were fully reconstructed, but where there are two track segments in either the upstream pair of drift chambers or the downstream pair. Finding two track segments in one pair of drift chambers indicates that the tracks were not reconstructed because they were both lost in the other pair of drift chambers. The two-track loss is measured in both data and MC, and is recorded in Table 6.2. The data-MC difference in this inefficiency is added to the difference from the single-track inefficiency, and this is the total correction to the acceptance due to tracking inefficiency.

| | Tracking Inefficiency Medium Intensity | Tracking Inefficiency High Intensity |
|-------------------|---|---|
| Data | | |
| $2\eta_1$ | 3.48% | 4.90% |
| η_0 | 0.19% | 0.21% |
| Total | 3.67% | 5.11% |
| Monte Carlo | | |
| $2\eta_1$ | 2.97% | 4.31% |
| η_0 | 0.05% | 0.09% |
| Total | 3.02% | 4.40% |
| Correction | 0.65% | 0.72% |
| MC no accidentals | | |
| $2\eta_1$ | 0.41% | 0.41% |
| η_0 | 0.00% | 0.00% |
| Total | 0.41% | 0.41% |

Table 6.2: Tracking inefficiencies in $K_L \rightarrow \pi^+\pi^-\pi^0$ data and Monte Carlo, for both medium and high intensity. The correction applied to the acceptance is the difference between the total data inefficiency and the total MC inefficiency. The bottom section of the table gives the inefficiencies for MC events in which no accidentals were included.

The remaining concern regarding the tracking inefficiency is to justify that these studies done with $K_L \rightarrow \pi^+\pi^-\pi^0$ events are also valid for the electron tracks that occur in the Dalitz mode. We suspect that most of the track loss in 1999 is due to accidentals (which increase with beam intensity). We verify this by rerunning the MC portion of the tracking studies without accidentals; these results are shown in the bottom section of Table 6.2. The tracking inefficiencies in MC with no accidentals are much smaller and, as expected, are not intensity-dependent. We conclude that a large fraction of the inefficiency (85% to 90%) comes from accidentals. Systematics associated with accidentals are discussed further in Section 6.4. Since the effect of accidentals cannot distinguish between tracks from electrons and those from charged pions, the tracking loss due to accidentals should be the same for electrons and pions. Therefore, we are justified in applying the results of the $K_L \rightarrow \pi^+\pi^-\pi^0$ track-loss study to the electron tracks in our analysis.

Table 6.2 shows the inefficiencies in data and Monte Carlo in the two intensity samples. The (relative) statistical errors associated with the inefficiencies are at the few percent level. Since the medium and high intensity samples are roughly equal in size, the overall tracking correction is approximately the average of the corrections in the two samples (0.68%). To be conservative, this entire correction is taken as a systematic uncertainty.

6.2 Radiative Corrections

As discussed in Section 4.9.2, the simulation of the Dalitz decay includes radiative corrections up to second order in α_{EM} . This corresponds to the interference between one-loop diagrams and the tree-level diagram (virtual corrections) as well as the radiation of a real photon (real corrections). To determine our sensitivity to radiative

corrections, we generate signal mode Monte Carlo with no radiative corrections to compare to the nominal MC sample. The acceptance increases by $(5.74 \pm 0.28)\%$ when radiative corrections are not included.

The QED calculations that are in the MC are well-understood theoretically, and we have evidence given in the sections below that the simulation of radiative corrections models the data well. Therefore, we assume the radiative corrections included in the MC to be correct to second order, and take a systematic uncertainty due to the higher-order corrections that are not included in the simulation. We can estimate the effect of these higher order corrections, such as two-loop corrections and one-loop corrections to the diagrams with real radiated photons. “Turning on” radiative corrections (that is, going from a simulation based on the tree-level diagram only to a simulation which includes the radiative corrections at second order in α_{EM}) results in a decrease in acceptance of 5.43%. We assume that adding the next order corrections to the simulation would cause a change in acceptance equal to 5.43% of the 5.43%; this would be a change of 0.29% in the acceptance (and correspondingly, in the measurement of $B(\pi^0 \rightarrow e^+e^-\gamma)/B(\pi^0 \rightarrow \gamma\gamma)$). Therefore, we take a 0.29% systematic uncertainty on our result due to the modelling of radiative corrections.

6.2.1 *The Reconstructed $e^+e^-\gamma$ Mass*

We now demonstrate that the simulation’s radiative corrections model the data well. By comparing the data to the nominal MC and to the MC without radiative corrections, we identify several distributions that are sensitive to the modelling of radiative corrections. In each distribution, the nominal MC is consistent with the data, while the MC without radiative corrections disagrees significantly with the data. The first such distribution is the reconstructed $e^+e^-\gamma$ mass, shown in Fig. 6.1. The data

to Monte Carlo overlays show that, without radiative corrections, the MC does not match the low side of the mass distribution.

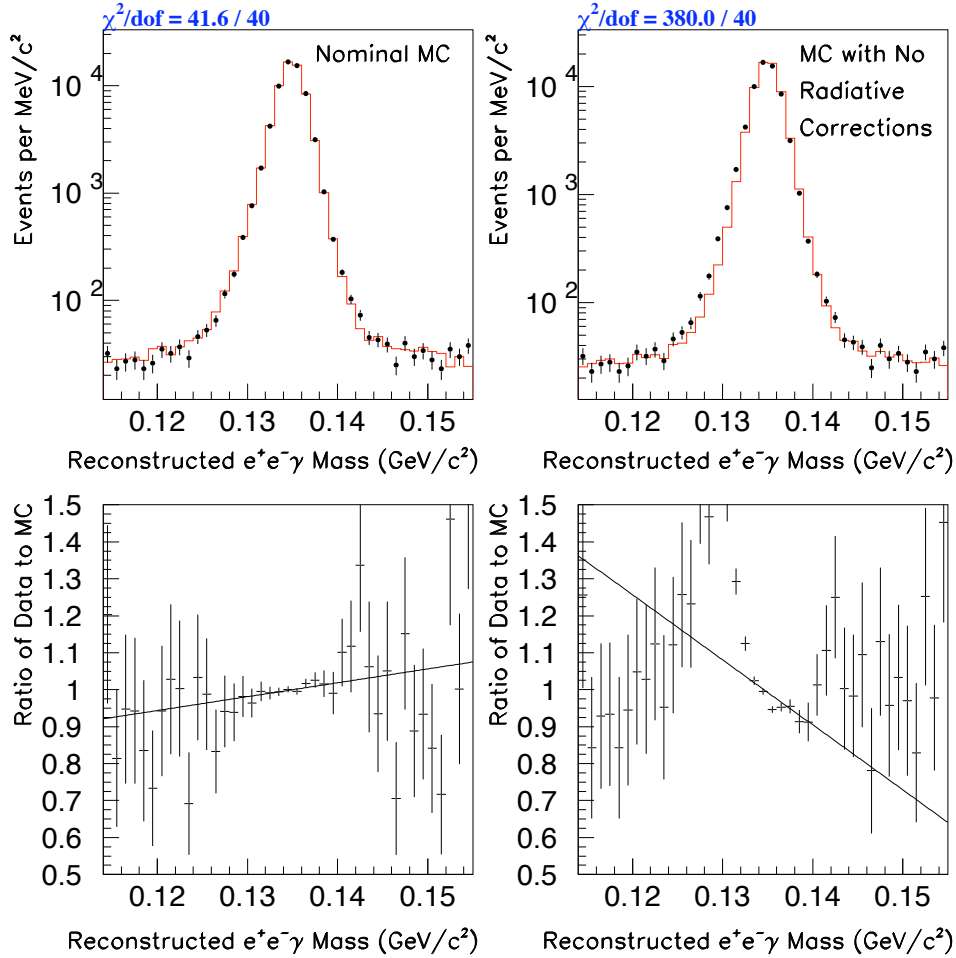


Figure 6.1: The left plots show the data to nominal Monte Carlo overlay and ratio for the reconstructed $e^+e^-\gamma$ mass. The right plots are the overlay and ratio for the reconstructed $e^+e^-\gamma$ mass in data and Monte Carlo with no radiative corrections. All selection criteria have been applied except for the requirement on the reconstructed $e^+e^-\gamma$ mass. The dots are data; the solid histogram is MC.

The width of the $e^+e^-\gamma$ mass peak as well as the χ^2 of the two data to MC overlays help to quantify how poorly the MC without radiative corrections models the data (and thereby give evidence that the simulation models radiative corrections

well.) Table 6.3 gives the width of the $e^+e^-\gamma$ mass distribution (from a gaussian fit) in data and in MC with and without radiative corrections. The width agrees at the 0.2 sigma level between data and nominal MC; there is a 7.5 sigma difference in the width between data and MC with no radiative corrections. Note that the width of the distribution in data gives an $e^+e^-\gamma$ mass resolution of $1.5 \text{ MeV}/c^2$. The χ^2 per degree of freedom for the data to MC overlays is 41.6/40 for nominal MC and 380.0/40 for the MC with no radiative corrections.

| Sample | Width of reconstructed $e^+e^-\gamma$ mass (GeV/c^2) | Error | Number of sigma different from data | χ^2/dof of the overlay with data |
|------------------|---|----------------------|-------------------------------------|--|
| Data | 0.0015088 | 6.2×10^{-6} | - | - |
| Nominal MC | 0.0015074 | 3.3×10^{-6} | -0.2 | 41.6/40 |
| MC no rad. corr. | 0.0014582 | 2.6×10^{-6} | -7.5 | 380.0/40 |

Table 6.3: The width (and error on the width) of the gaussian fit to the reconstructed $e^+e^-\gamma$ mass distribution in data, nominal Monte Carlo, and Monte Carlo with no radiative corrections. The third column gives the data-MC difference in width in terms of the number of sigma, for both nominal MC and MC with no radiative corrections. The χ^2 per degree of freedom of the data to MC overlay is also given.

6.2.2 The Reconstructed e^+e^- Mass

Distributions that are related to the track separation are also sensitive to radiative corrections; this includes the cell separation, the tracks' opening angle, and the e^+e^- mass. This is crucial because, while the $e^+e^-\gamma$ mass distribution is sensitive to both real and virtual corrections, it is more sensitive to the real corrections. Table 6.4 shows that the real and virtual corrections cause the acceptance to change differently, so we need to make sure we are modelling both parts of the radiative corrections correctly.

| Sample | Fraction of Generated Events | Change in Acceptance Relative to No Radiative Corrections |
|---------------------|------------------------------|---|
| Nominal MC | - | -5.43% |
| real corrections | 16.18% | -11.76% |
| virtual corrections | 83.82% | -3.28% |

Table 6.4: The percent change in acceptance resulting from “turning on” radiative corrections (that is, going from MC with no radiative corrections to the nominal MC). The nominal MC sample is broken into subsamples based on whether an event was affected by the real or virtual corrections; 16.18% of generated events have a real radiated photon (that is, they are $\pi^0 \rightarrow e^+e^-\gamma\gamma$ events) and the remaining 83.82% have virtual corrections. The percent change in acceptance is given for each of these subsamples.

Since we expect the e^+e^- mass distribution to be sensitive to the virtual corrections, we generate a MC sample in which only the virtual corrections are turned off, and compare the e^+e^- mass distribution in data and MC. Figure 6.2 confirms that while nominal MC models the e^+e^- mass distribution well, the MC with no virtual corrections does not match the data, especially at low e^+e^- mass. Because the nominal cell separation requirement eliminates most events at low e^+e^- mass (below ~ 10 MeV/ c^2), where the effect of virtual corrections is most prominent, we have included events with a cell separation of one or greater for these plots. The results of our cell separation cross check (see Section 7.1) indicate that $B(\pi^0 \rightarrow e^+e^-\gamma)/B(\pi^0 \rightarrow \gamma\gamma)$ is stable for cell separations below the requirement of three cells, down to and including a cell separation of one.

6.2.3 The Distribution of the Number of Software Clusters

Just as the e^+e^- mass distribution is sensitive mainly to virtual corrections, the distribution of the number of software clusters (see Section 3.4.2) is sensitive to radiative corrections only through the real corrections. The real radiative corrections result in

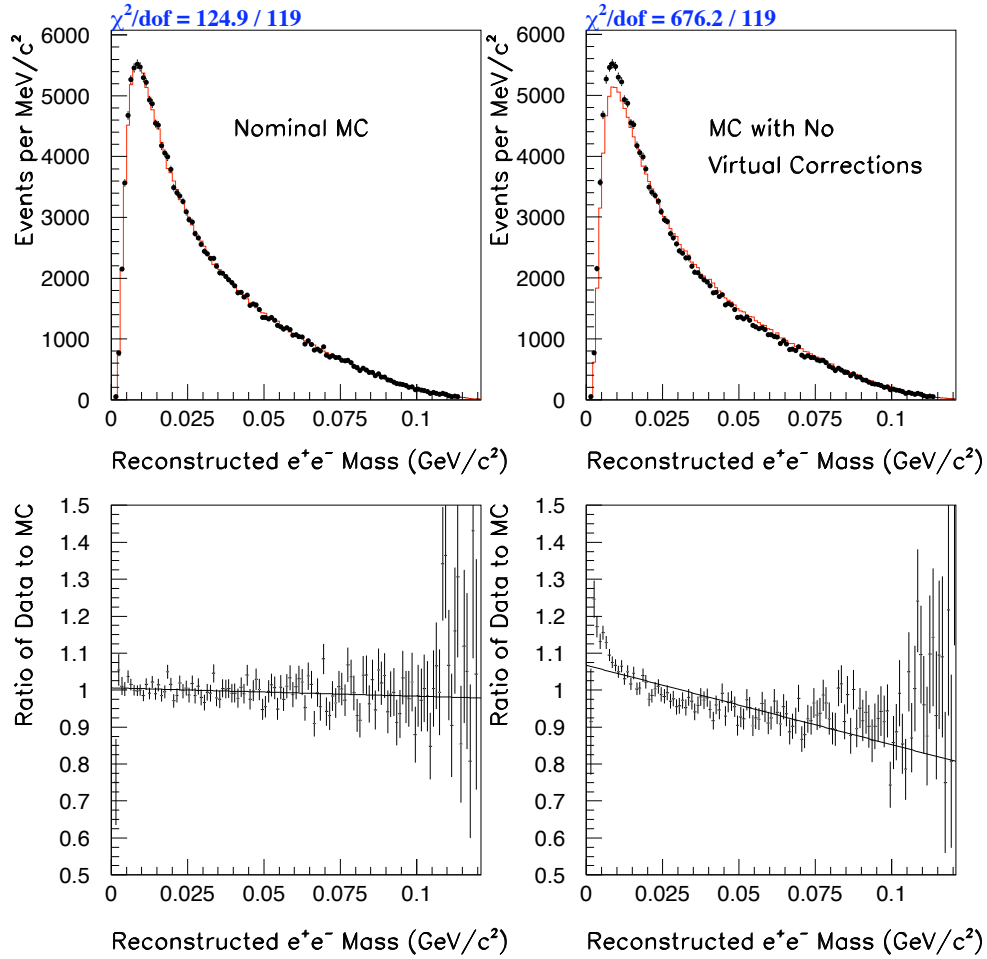


Figure 6.2: The left plots show the data to nominal Monte Carlo overlay and ratio for the reconstructed e^+e^- mass. The right plots are the overlay and ratio for the reconstructed e^+e^- mass in data and Monte Carlo with no virtual corrections. All selection criteria have been applied except the requirement on the reconstructed e^+e^- mass and the cell separation requirement; the sample includes events with cell separation of one and greater (the nominal requirement is cell separation greater than three). The dots are data; the solid histogram is MC.

an extra photon compared to the tree-level Dalitz decay. This photon can sometimes register in the calorimeter as a software cluster, so we expect the distribution of the number of software clusters to be sensitive to the simulation of the real radiative corrections. Figure 6.3 confirms this. Although the agreement is not perfect between data and nominal MC, the agreement is much worse if radiative corrections are not included.

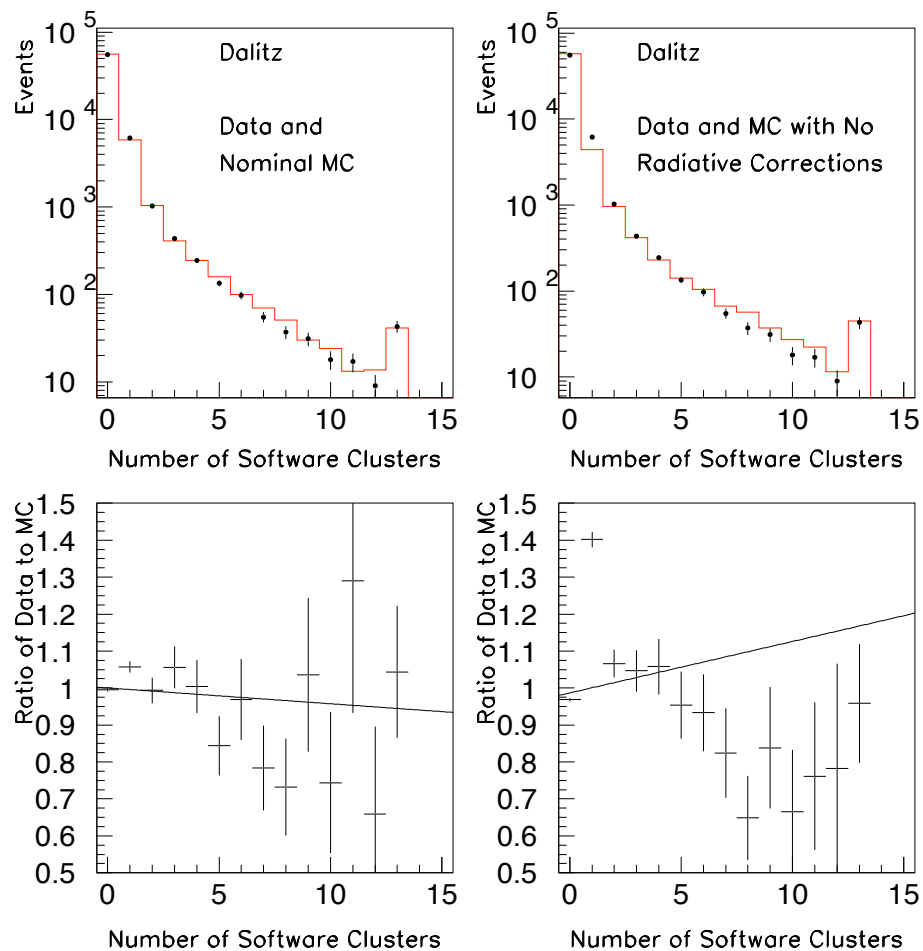


Figure 6.3: Data to Monte Carlo overlays of the number of software clusters in Dalitz mode. The left plots are nominal MC and the right plots are MC with no radiative corrections. The top plots are the overlays and the bottom plots are the data to MC ratios. The dots are data and the solid histogram is MC.

With this evidence that both real and virtual corrections are well-simulated, taking a systematic uncertainty of 0.29% based on the projected effect of the higher-order radiative corrections (that are not included in the MC) on $B(\pi^0 \rightarrow e^+e^-\gamma)/B(\pi^0 \rightarrow \gamma\gamma)$ is justified.

6.3 Detector Material

As mentioned in Section 4.3, the simulation models electromagnetic interactions in the detector material, such as bremsstrahlung. Most particle losses in the reconstruction associated with bremsstrahlung result from interactions upstream of the analysis magnet; the material upstream of the analysis magnet is approximately 0.73% of a radiation length (while the total material through DC4 is 1.18% of a radiation length) [38].

Turning off the simulation of bremsstrahlung in the Dalitz mode Monte Carlo increases the acceptance by $(4.66 \pm 0.27)\%$. As might be expected, turning off the simulation of bremsstrahlung in the normalization mode has a negligible effect – the acceptance decreases by $(0.038 \pm 0.039)\%$. Based on previous studies [38], the Monte Carlo models the detector material at the 5-10% level, so, from the change in acceptance in the signal mode, we assign a conservative systematic error of 0.47% for this.

Turning off the simulation of bremsstrahlung in the Dalitz mode MC also allows us to see how well the effect is being modelled by looking at the distribution of the $\text{brem-}\gamma$ distance (described in Section 3.7.2). Because both bremsstrahlung and radiative corrections affect the shape of this distribution, it is instructive to compare the distribution for various combinations of turning on/off these two effects. Figure 6.4 shows the data to MC overlays for data and nominal MC, for data and MC

with no bremsstrahlung, for data and MC with no radiative corrections, and for data and MC with no bremsstrahlung and no radiative corrections. It is clear that both bremsstrahlung and radiative corrections need to be included in the simulation for this distribution to match the data.

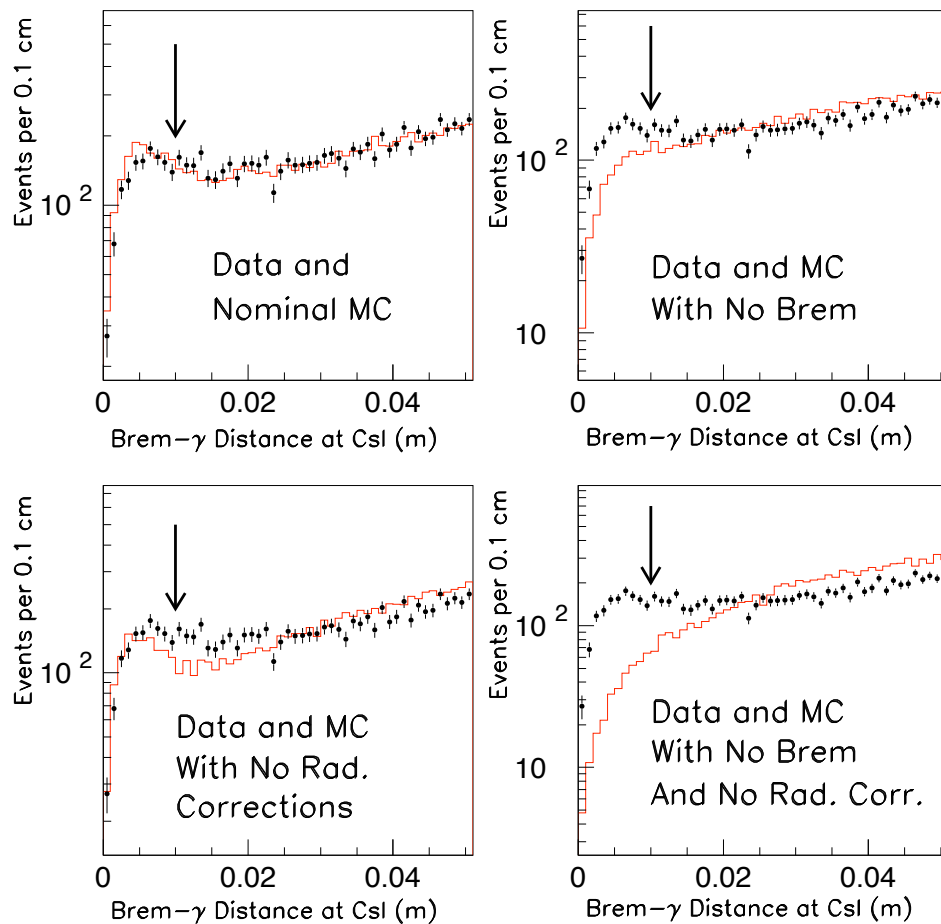


Figure 6.4: Data to MC overlays of the distribution of the brems- γ distance at the calorimeter. The data are compared to nominal MC, to MC with no bremsstrahlung, to MC with no radiative corrections, and to MC with no bremsstrahlung and no radiative corrections. The dots are data and the solid histogram is MC. All selection criteria have been applied except for the requirement on the brems- γ distance; this requirement is that the brems- γ distance be greater than 1 cm, and is indicated by the arrow on each plot.

6.4 Accidentals

To study the effect of accidentals, we generate MC with no accidental overlays. The change in acceptance is large in both modes; the acceptance increases by $(37.11 \pm 0.31)\%$ in the Dalitz mode and by $(31.68 \pm 0.04)\%$ in the $3\pi^0$ mode. Because we are taking the ratio, most of the change in acceptance cancels. The change in the ratio of branching ratios due to these changes in acceptance is $\frac{1.3168}{1.3711} - 1 = -0.0396$; that is, $B(\pi^0 \rightarrow e^+e^-\gamma)/B(\pi^0 \rightarrow \gamma\gamma)$ decreases by 3.96% if accidentals are not included in the simulation.

We can attribute this change in the ratio of branching ratios to two effects: the presence of tracks in the signal mode (and not in the normalization mode) and the presence of one more photon in the normalization mode than in the signal mode. We will consider each of these effects to determine our sensitivity to the modelling of accidentals.

6.4.1 Study Using the SOD Distribution

We can use the drift chamber sum-of-distances (SOD) distributions for the tracks (see Section 3.4.1 and Section 4.5) to measure our sensitivity to changes in the acceptance due to accidentals. Figure 6.5 shows overlays of the SOD distribution between data and nominal MC and between data and MC with no accidentals. The overlay between data and MC without accidentals shows extremely poor agreement. The agreement between data and nominal MC is much better, although it is not perfect.

However, since low SODs come almost entirely from accidentals, we can use the fraction of events in the SOD distribution below -0.2 mm as a measure of how well the accidentals are modelled. This “low-SOD fraction” is well-modelled in nominal MC – it is within about 2.5 sigma of the fraction in data. The fraction of low SOD events

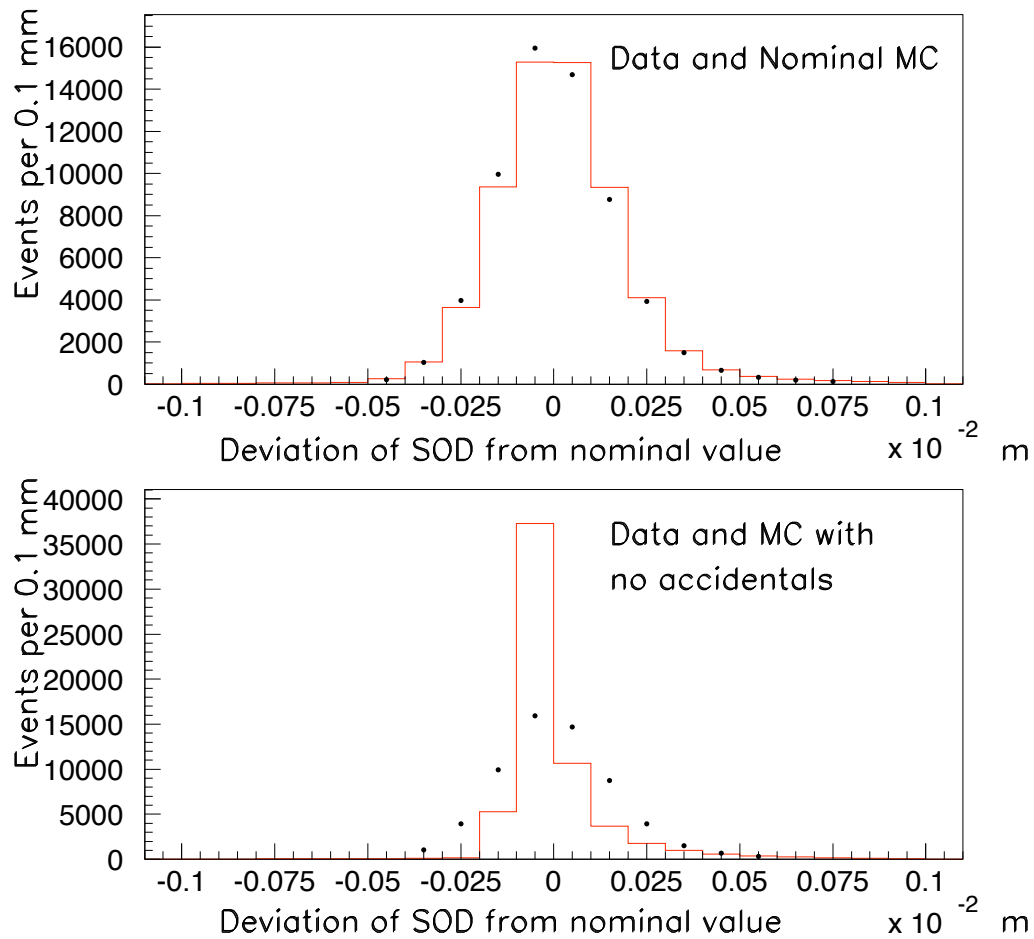


Figure 6.5: Data to Monte Carlo overlays of drift chamber sum-of-distance (SOD) distributions for one of the x tracks in DC1. The top plot is nominal MC and the bottom plot is MC without accidentals. The dots are data and the solid histogram is MC. Deviation between SOD and cell spacing is shown, so zero deviation means SOD=6.35mm, and negative deviations are low SODs.

| Sample | Fraction of events whose SOD is lower than nominal by 0.2 mm or more | Error | Number of sigma different from data |
|--------------------------------------|--|--------|-------------------------------------|
| Data | 0.1174 | 0.0013 | - |
| Nominal MC | 0.1138 | 0.0006 | 2.5 |
| MC no accid. | 0.0280 | 0.0003 | 68.5 |
| MC: 97% nominal 3% no accidentals | 0.1103 | 0.0006 | 5.0 |

Table 6.5: The fraction of events (and the error) whose SOD is more than 0.2 mm lower than the nominal value (6.35 mm). The last column gives the difference in this low-sod fraction between data and Monte Carlo for nominal MC, for MC with no accidentals, and for a combination of the two Monte Carlos.

in the MC sample with no accidentals differs from the fraction in data by about 68.5 sigma (see Table 6.5).

Since the fraction of low-SOD events is very sensitive to accidentals, we can use it to test the modelling of accidental activity in the following way. We create a mixture of MC with and without accidentals by combining a fraction, f , of MC with no accidentals and $(1 - f)$ of nominal MC. We determine at what level we can detect the presence of the MC with no accidentals by monitoring the change in the low-SOD fraction as we vary f . Approximately 3% MC with no accidentals (combined with 97% nominal MC) is needed for the fraction of low-SOD events in the Monte Carlo mixture to be significantly different (~ 5 sigma) from that in data. This means that, from the presence of tracks (and therefore SOD distributions) in the signal mode, we can determine that data and MC are consistent at the $3.96\% \times 0.03 = 0.1188\%$ level.

6.4.2 Study Using Software Clusters

Because we also have one more photon in the normalization mode than in the signal mode, our sensitivity to accidentals in the neutral parts of the two decays does not

entirely cancel in the ratio. The effect of accidentals in neutral mode decays is most obvious in the distribution of the number of software clusters (see Section 3.4.2). The extra energy in the calorimeter from accidental activity is often below the hardware cluster threshold, but is grouped into software clusters during analysis. To study the effect of accidentals on the number of software clusters, we look at the distribution in the $3\pi^0$ mode. Figure 6.6 shows overlays of the distributions of the number of software clusters between data and nominal MC and between data and MC with no accidentals. Without accidentals, the simulated events almost never have extra software clusters.

| Sample | Fraction of events with zero software clusters | Error | Number of sigma different from data |
|--------------------------------------|--|---------|-------------------------------------|
| Data | 0.90250 | 0.00016 | - |
| Nominal MC | 0.90309 | 0.0008 | 3.3 |
| MC no accid. | 0.981045 | 0.0003 | 486.3 |
| MC: 99% nominal 1% no accidentals | 0.1103 | 0.0006 | 8.9 |

Table 6.6: The fraction of events with no software clusters (and the uncertainty on this fraction). The last column gives the difference in this fraction between data and Monte Carlo for nominal MC, for MC with no accidentals, and for a combination of the two Monte Carlos.

Because of this, we use the fraction of events with zero software clusters as a measure of the sensitivity to accidentals. Table 6.6 shows the fraction of events with no software clusters in data, in nominal Monte Carlo, in MC with no accidentals, and in a sample that is a mixture of nominal MC and MC without accidentals. Between nominal MC and data, the fractions are different by about 3.3 sigma; between MC with no accidentals and data, the difference is 486.3 sigma. Using 99% nominal MC with 1% MC with no accidentals gives a significant mismatch with data in terms of the fraction of events with no software clusters (~ 8.9 sigma).

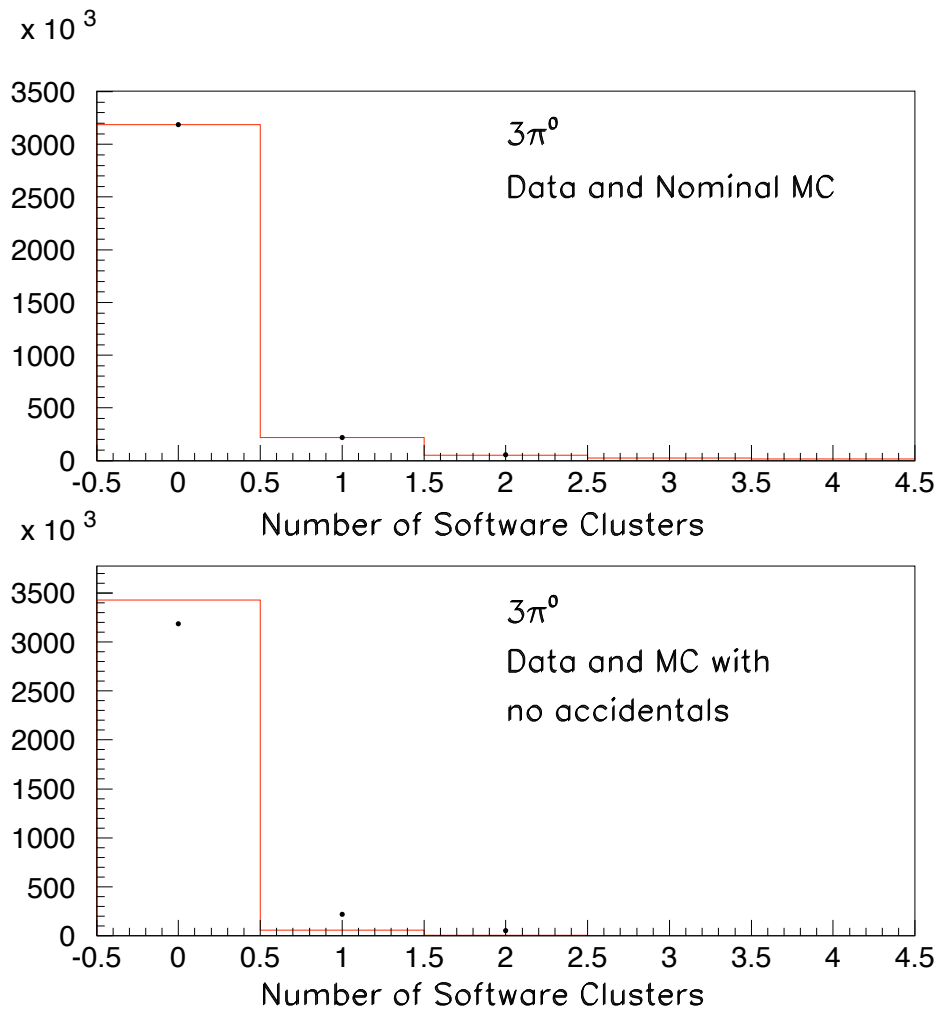


Figure 6.6: Data to Monte Carlo overlays of the distribution of the number of software clusters. The dots are data and the solid histogram is MC. The top plot is the nominal MC and the bottom plot is the MC without accidentals.

Therefore, from the neutral decay products, we are sensitive to changes in the ratio of branching ratios (due to accidentals) greater than $3.96\% \times 0.01 = 0.0396\%$. Combining this systematic error with the systematic error from our sensitivity to accidentals because of the tracks in the signal mode (0.1188%) gives a total systematic uncertainty due to accidentals of 0.125%.

6.5 Relative Trigger Inefficiency

In Section 5.2, we made a correction to the acceptance in the signal mode due to different relative trigger inefficiencies in data and Monte Carlo. This section describes how we arrive at the correction factor.

Since the signal and normalization modes come from two different triggers, we need to measure how well we know the relative trigger efficiency in data and in MC. The $3\pi^0$ s come from trigger 6 and the Dalitz events come from trigger 14. To determine the level of trigger inefficiency in data, we use random accepts from trigger 6 and analyze them with the Dalitz mode reconstruction. The fraction of the events that reconstruct as Dalitz decays but are not tagged as being in trigger 14 is the rate of trigger 14 inefficiency relative to trigger 6.

We find 207 random accepts that pass all Dalitz selection criteria, and all 207 are in trigger 14. To increase statistics for this study, we loosen the selection requirements by removing the cell separation cut. We find 716 events that pass all cuts except the cell separation cut, and 1 of these is not in trigger 14. This is an inefficiency of $1/716 = 0.0014$ in the data.

It is unlikely that the MC has a relative trigger inefficiency since we expect this type of inefficiency to come from electronic glitches or hardware failures that are not simulated. We can perform a check to make sure this assumption is valid. We use

Levels 1 and 2 of trigger 6 to generate Dalitz mode events; since the Level 3 software trigger is not applied, it is possible for Dalitz events to pass the trigger. (Essentially, this procedure replicates the Dalitz events that can be found in the trigger 6 random accepts in data.) As in data, we analyze this sample for Dalitz decays. We confirm that there is no measurable relative trigger inefficiency between trigger 6 and trigger 14 in MC.

Therefore, the relative trigger inefficiency found in data represents a data-MC difference, and it is applied as a correction to the Dalitz acceptance. To be conservative, the entire correction of 0.14% is taken as a systematic uncertainty.

6.6 $3\pi^0$ Trigger Inefficiency

In addition to the relative inefficiency between trigger 6 and trigger 14, we need to measure the absolute inefficiency of trigger 6, the $3\pi^0$ trigger. The measurement of $B(\pi^0 \rightarrow e^+e^-\gamma)/B(\pi^0 \rightarrow \gamma\gamma)$ is sensitive to any trigger 6 efficiency difference in data versus Monte Carlo. By design, there is no trigger 6 inefficiency in the Monte Carlo; therefore, we need only measure the trigger 6 inefficiency in data. To do this, we use data events from trigger 5 (found on QKNL tapes 1 through 36). Trigger 5 essentially only requires some energy in the calorimeter and has no Level 3 requirements, so all of these events are random accepts. The events are sent through the $3\pi^0$ analysis. For all those events which are reconstructed as $3\pi^0$ s, we check whether they are in trigger 6, using the the in-time slice of the Level 1 mask latch (KTeVana variable L1MASK_LAT). We use the latch because it contains all trigger 6 events before the prescale is applied; we need to check whether the event was in trigger 6 before the hardware prescale was applied since the prescale eliminates some of the events that are originally tagged as being in trigger 6.

The fraction of events which pass all $3\pi^0$ cuts but are not in trigger 6 is the rate of trigger 6 inefficiency. We find 402,193 trigger 5 events which reconstruct as $3\pi^0$ s. Of these, 402,176 are also in trigger 6. This gives an inefficiency of 0.0042%, with a statistical uncertainty of 0.0010%.

Because the statistical uncertainty on the measured inefficiency is relatively large compared to the inefficiency itself, we use the prescription described in [27] to translate this measurement of the inefficiency into a systematic uncertainty. The prescription is as follows. Let s be the inefficiency and let σ_s be the statistical uncertainty on the inefficiency. We convert $s \pm \sigma_s$ into a systematic uncertainty, Δ_s , such that the range $[-\Delta_s, +\Delta_s]$ includes 68.3% of the area of a Gaussian with mean s and width σ_s :

$$\frac{1}{\sigma_s \sqrt{2\pi}} \int_{-\Delta_s}^{+\Delta_s} dx \exp \left[-\frac{(x-s)^2}{2\sigma_s^2} \right] = 0.683. \quad (6.1)$$

Following this procedure gives a systematic uncertainty of 0.0047% at the one-sigma level. This is reported in the systematics table, Table 6.1, as $< 0.01\%$. No correction is made to the acceptance based on this negligible inefficiency.

6.7 $3\pi^0$ Trigger Prescale

The ratio $B(\pi^0 \rightarrow e^+e^-\gamma)/B(\pi^0 \rightarrow \gamma\gamma)$ is directly sensitive to any deviations in the trigger 6 prescale from the nominal value. (There is no trigger 14 prescale.) Trigger 6, the $3\pi^0$ trigger, has a hardware prescale of 2 and a software prescale of 5/2 (giving a total trigger-level prescale of 5). Recall that a hardware prescale of 2 means that every other event that comes through trigger 6 is thrown out. Because there are so many trigger 6 events (largely $3\pi^0$ decays), we can eliminate some of them via a prescale and still have plenty of statistics. The software prescale is not vulnerable to

inefficiencies; however, the hardware prescale is. We use two approaches to determine the hardware prescale's deviation from the nominal value of 2.

6.7.1 *Study Using Trigger 5 Random Accepts*

First, we use trigger 5 events that reconstruct as $3\pi^0$ s, as for the trigger 6 inefficiency study described in Section 6.6. We compare the number of these events that are in trigger 6 according to the latch (L1MASK_LAT – see Section 6.6), which is filled before the hardware prescale is applied, with the number that are in trigger 6 according to the trigger mask (KTeVana variable MSKTRG), which is filled after the prescale has been applied. The ratio of the latter to the former should be 0.5 (for the nominal prescale of 2). We find 201,285 events in the trigger mask after the prescale, and 402,176 events in the Level 1 mask latch (before the prescale), for a ratio of 0.50049 ± 0.00079 . This corresponds to a $0.098\% \pm 0.158\%$ difference from the nominal value of 0.5. Following the procedure described in Section 6.6, we convert this inefficiency into a systematic uncertainty of 0.19%.

6.7.2 *Study Using Scaler Data*

However, since the uncertainty on this measurement of the inefficiency is large compared to the inefficiency we find, we turn to another technique, which has larger statistics, to measure the prescale. We can use the scaler data that was recorded during the experiment to look at all events that came through trigger 6 before and after the prescale. The relevant variables in the scaler code are BTM_06 for before the prescale (BTM stands for beam trigger monitor) and RAW_L1_B06 for after the prescale [39].

We include only those runs which are used in the nominal analysis, and we measure

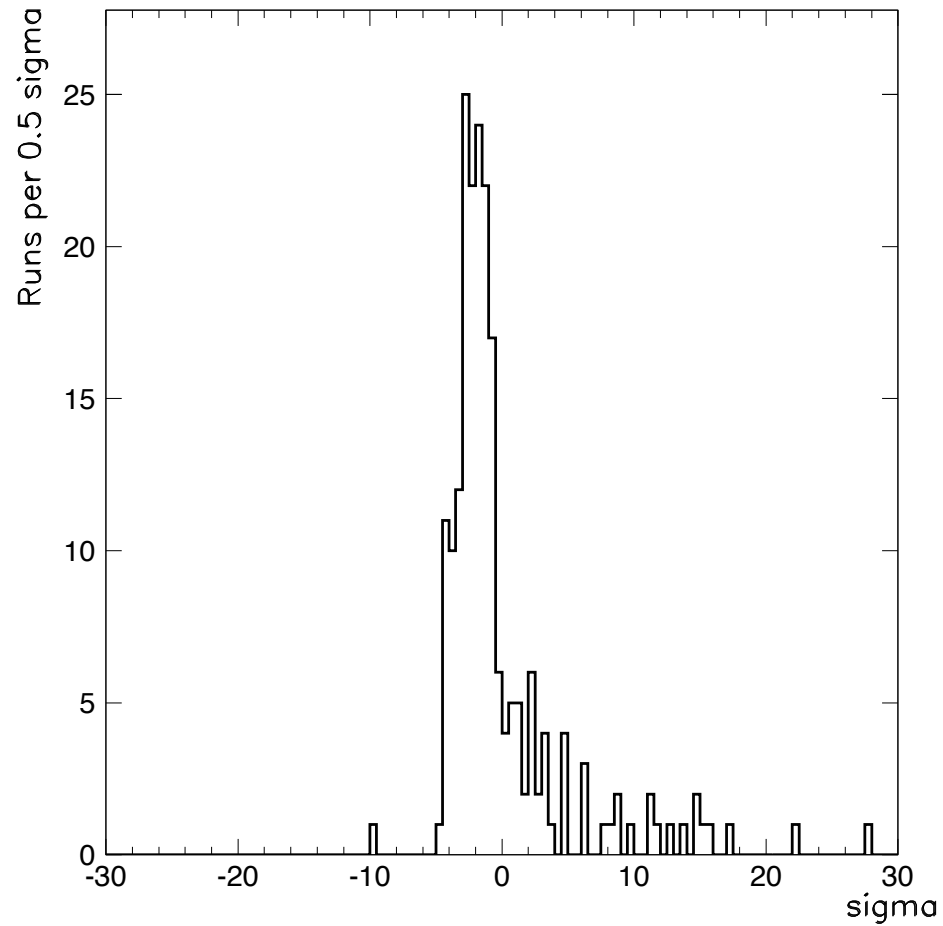


Figure 6.7: The σ distribution for the ratio of trigger 6 events after the hardware prescale to trigger 6 events before the hardware prescale for each run used in the nominal analysis, relative to the average ratio over all these runs.

both the overall ratio of L1_RAW_06 (after ps) to BTM_06 (before ps) and error, as well as this ratio and error for each run. Using the errors on each run, we can find the number of sigma away from average for each run's ratio. This sigma distribution is shown in Fig. 6.7. The overall ratio is $0.500044 \pm 3.1099 \times 10^{-6}$. The sigma distribution shows a significant number of outliers, most of which are from runs in which the measured prescale is greater than the nominal prescale of 1/2. This most likely indicates an intermittent defect in the prescale electronics.

Because some of the outliers are as far out as 30 sigma, we take an error on the ratio equal to 30 sigma (that is, $30 \times 3.1099 \times 10^{-6}$), or 9.3297×10^{-5} . This is a 0.01866% uncertainty on the measured prescale of 0.500044. Since the measured prescale deviates from 1/2 by 0.0088%, we have a very small uncertainty on the prescale of approximately $0.0088\% \pm 0.0187\%$. Using the prescription in Section 6.6, this deviation corresponds to a one-sigma uncertainty on the prescale of 0.0208%. If the uncertainty had been statistically different from zero (that is, if the measured prescale deviation from 1/2 had been statistically significant), we would have taken the uncertainty as an inefficiency in the prescale, and corrected for it in the acceptance. However, since it is not significant, we only include it as a systematic uncertainty.

6.8 Form Factor

As discussed in Section 1.3.1, the amplitude for the $\pi^0 \rightarrow e^+e^-\gamma$ decay contains a form factor, $f(x)$, at the $\pi^0\gamma\gamma$ vertex (where $x = (m_{e^+e^-}/m_\pi)^2$). We use the linear approximation, $f(x) \approx (1 + ax)$, where a is the π^0 slope parameter. The 2006 PDG value for a is 0.032 ± 0.004 [4], and this value is used in the simulation of the Dalitz decay (see Section 4.9.2).

To determine our sensitivity to the form factor, we generate MC with $a = 0.000$

(eight sigma below the nominal value) and with $a = 0.064$ (eight sigma above the nominal value). The change in acceptance is very small in both cases. Decreasing the value of a by eight sigma results in a decrease in the acceptance of $(0.388 \pm 0.274)\%$, which corresponds to a 0.518% uncertainty according to the prescription given in Section 6.6. Increasing the value of a by eight sigma results in an increase in the acceptance of $(0.155 \pm 0.274)\%$, which corresponds to a 0.318% uncertainty (again using the prescription found in Section 6.6). Taking the larger of these two uncertainties and dividing by 8 gives a one-sigma level systematic uncertainty due to the form factor of 0.06%.

6.9 Photon Inefficiency

In Section 3.7.1, we describe the shape χ^2 requirement, which is used to determine if a cluster corresponds to a photon by seeing how closely the cluster's transverse energy profile matches that expected for a photon. Although the requirement is loose (shape $\chi^2 < 100$), there is a small chance that a real photon will not pass this requirement.

In the V_{us} analysis [35], the effect of the photon cluster shape requirement (shape χ^2) was studied by removing this cut in the $B(K_L \rightarrow \pi^0 \pi^0 \pi^0) / B(K_L \rightarrow \pi^\pm e^\mp \nu)$ analysis. Removing the cut results in a change of 0.05% in the ratio, which is taken as a systematic uncertainty in that analysis. This measurement of $B(\pi^0 \rightarrow e^+ e^- \gamma) / B(\pi^0 \rightarrow \gamma \gamma)$ uses $K_L \rightarrow 3\pi_D^0$ and $K_L \rightarrow 3\pi^0$, so there is only a one-photon difference between the signal (5 γ s) and normalization (6 γ s) modes (as opposed to the six-photon difference in the study from the V_{us} analysis.) Thus, the photon inefficiency is 1/6 of the one found in the V_{us} analysis, or, $\sim 0.01\%$.

6.10 Background

The main source of background in the $K_L \rightarrow 3\pi_D^0$ decay is $K_L \rightarrow 3\pi^0 \rightarrow 6\gamma$, with one photon converting to an e^+e^- pair at the vacuum window. To study this, $3\pi^0$ Monte Carlo events are generated in trigger 14 as described in Section 4.10 and reconstructed with the Dalitz analysis. Figure 6.8 shows the distribution of reconstructed vertex z position for the conversion events, zoomed in to the region around the vacuum window at $z = 159$ meters.

For the background study, we generate 50 times as many $3\pi^0$ events as for the nominal $3\pi^0$ analysis. If these generated events had gone through the nominal $3\pi^0$ analysis, we would expect to reconstruct 50 times as many $3\pi^0$ decays as we did in the nominal analysis (that is, $50 \times 12,668,419$). Recall that in data, we find 3,529,065 $3\pi^0$ events, but this is after a total prescale of 50 has been applied; so, in data, there are really $50 \times 3,529,065$ $3\pi^0$ events.

In the Monte Carlo background sample, we find that seven conversion events remain after the Dalitz reconstruction is done and the selection criteria criteria are imposed. From this, we can estimate the number of conversion events (call this number x) that fake the Dalitz decay in the data sample we are using for this measurement:

$$\frac{7}{50 \times 12,668,419} = \frac{x}{50 \times 3,529,065}, \quad (6.2)$$

and,

$$x = 1.95. \quad (6.3)$$

The 1.95 conversion events that fake the Dalitz decay in the signal mode data sample of 63,693 events constitute a $3 \times 10^{-5} = 0.003\%$ background. This level of background is negligible, and instead of performing a background subtraction, we

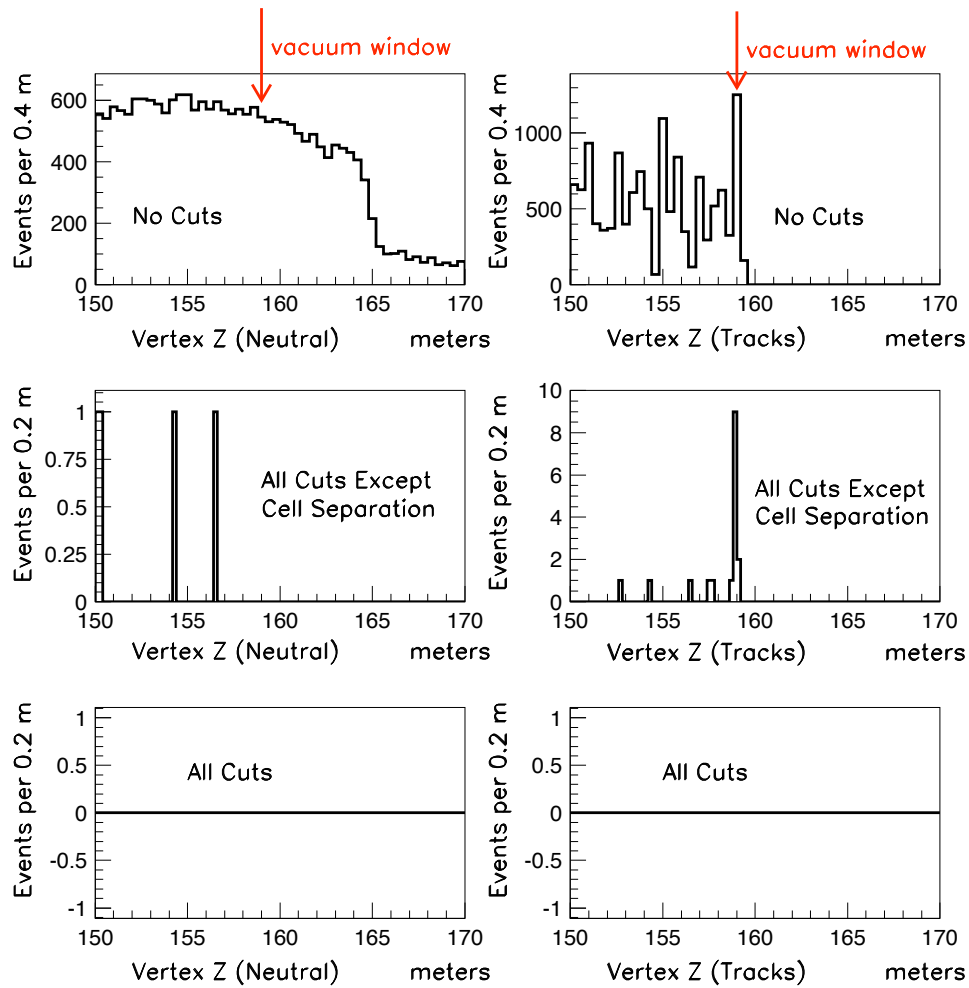


Figure 6.8: The reconstructed vertex z position of events with a photon conversion, focusing on the region near the vacuum window (at $z = 159$ m). The plots on the left show the reconstructed vertex position based on the neutral clusters in the calorimeter (the photons from two of the π^0 s). The plots on the right are the reconstructed vertex z position based on the vertex of the two tracks. The top plot on each side is before cuts, the middle plot is after all cuts except the cell separation requirement, and the bottom plot is after all cuts. In the top-right and middle-right plots, the spike at the vacuum window is visible, indicating that the tracks are from photon conversions there. Note that the vertex z requirement in the analysis applies to the z reconstructed from the neutral clusters. Also note that seven events remain after all cuts, although none of them are near the vacuum window, and so do not appear in the bottom two plots.

take this as a systematic error.

6.11 Cut Variations

Systematics associated with the selection criteria are studied by varying each selection requirement and monitoring the effect on $B(\pi^0 \rightarrow e^+e^-\gamma)/B(\pi^0 \rightarrow \gamma\gamma)$. For variables on which a requirement exists in both modes, a large fraction of any data-Monte Carlo disagreement should cancel in the ratio, and we find this to be the case when cuts are varied. For variables that only exist in the Dalitz mode, no such cancellation will occur, so systematic errors can arise from any disagreement between data and Monte Carlo. The requirements unique to the signal mode, such as vertex z position, cell separation requirement, and the e^+e^- mass requirement, are varied and no significant changes are observed in $B(\pi^0 \rightarrow e^+e^-\gamma)/B(\pi^0 \rightarrow \gamma\gamma)$. Based on the small variations we do observe, we estimate that our sensitivity to changes in the acceptance due to the selection criteria is no greater than 0.1%.

To confirm that we are relatively insensitive to cut variations, there are several variables to which we should pay particular attention. Since we rely on the MC to measure the acceptance in each mode, we need to make sure the distribution of the vertex z position is well-modelled in each mode. We would also like to investigate how well the MC simulates the cell separation distribution in the Dalitz mode, since we know the tracking efficiency varies with cell separation. Additionally, we check that varying the e^+e^- mass cut does not affect the result. We discuss each of these topics below.

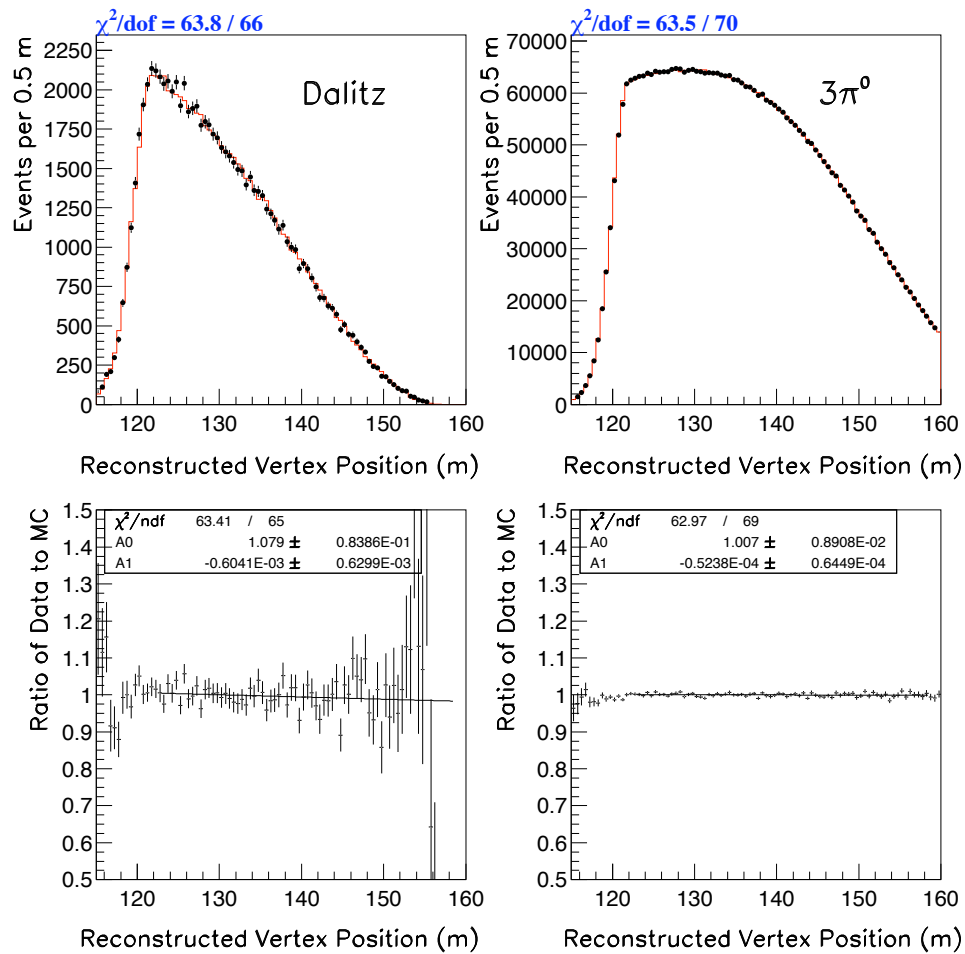


Figure 6.9: The reconstructed kaon z -vertex for both modes, after all selection requirements except the z requirement. The top plots are the data to MC overlays, where the dots are data and the solid histogram is Monte Carlo. The bottom plots are the data to MC ratios.

6.11.1 *Varying the Vertex z Requirement*

Plotting data to Monte Carlo overlays for each variable shows that the simulation models the physics very well. Figure 6.9 shows the data to MC overlays and ratios for the reconstructed vertex z positions in both Dalitz and $3\pi^0$ modes. There is no significant slope in the ratio of data to Monte Carlo z positions in either mode. The slope is $(-0.60 \pm 0.63) \times 10^{-3}$ per meter in the Dalitz mode and $(-0.52 \pm 0.64) \times 10^{-4}$ per meter in the $3\pi^0$ mode. This indicates that the acceptance in each mode is well-modelled.

6.11.2 *Varying the Cell Separation Requirement*

Figure 6.10 shows the cell separation distribution for the tracks in the Dalitz mode. The top left plot shows the distribution after all cuts except the cell separation cut; the right plot shows the distribution after making the additional requirement that the cell separation be greater than 3 (cells). It is reassuring that in the neighborhood of the cut, the data and MC agree. We explore this agreement further in Section 7.1.

6.11.3 *Varying the e^+e^- Mass Requirement*

Another important consideration is what happens if we vary the e^+e^- mass cut; the nominal cut is at $15 \text{ MeV}/c^2$, and we test cuts at 0, 10, 12, and $20 \text{ MeV}/c^2$. For each of these cut variations, the resulting $B(\pi^0 \rightarrow e^+e^-\gamma)/B(\pi^0 \rightarrow \gamma\gamma)$ differs from nominal by approximately 1 sigma (based on statistics). We conclude that the systematic uncertainty associated with the e^+e^- mass cut is not significant; any uncertainty is subsumed in the 0.1% overall uncertainty we have assigned for cut variations.

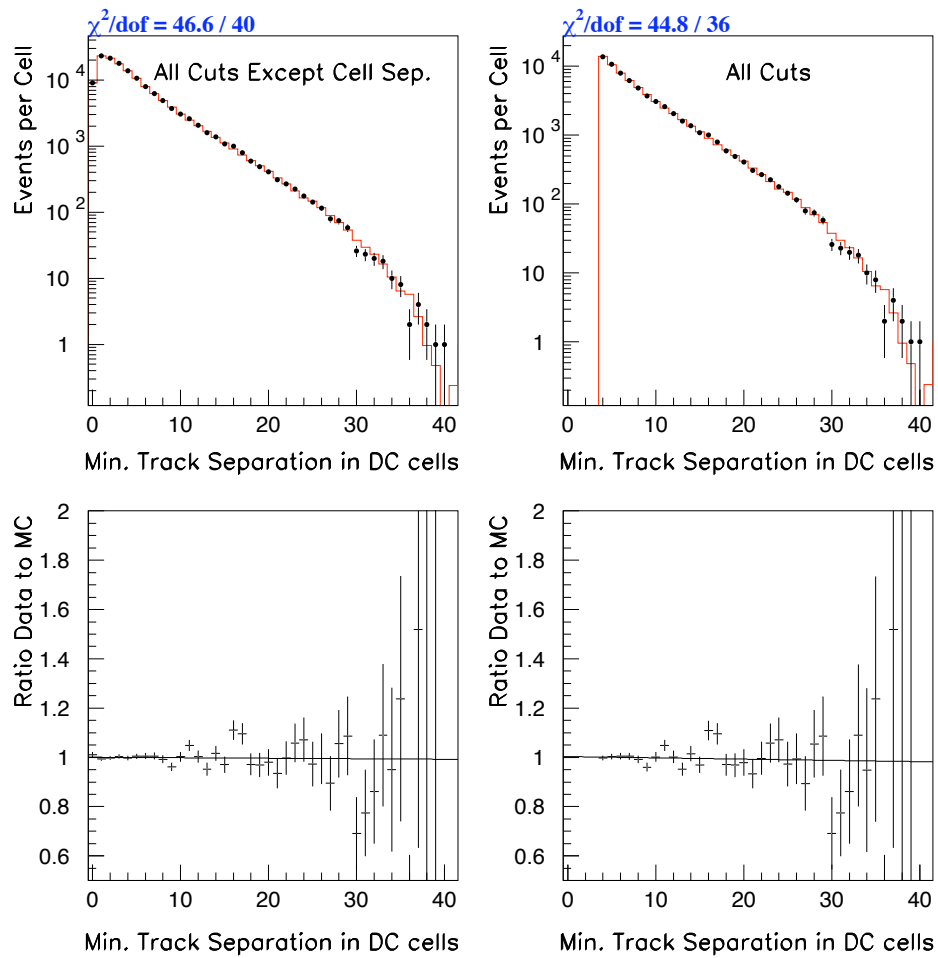


Figure 6.10: Data to MC overlays and ratios of the reconstructed cell separation of the tracks in the Dalitz mode. The dots are data and the solid histogram is MC. The left pair of plots is after all selection requirements except the cell separation cut, and the right pair is after all selection requirements.

6.12 e^+e^- Mass Scale

The requirement that the e^+e^- mass is greater than $15 \text{ MeV}/c^2$ is a possible source of systematic uncertainty. The e^+e^- mass requirement is sensitive to how well we reconstruct the e^+e^- mass; any scale shift in the reconstruction will lead to an uncertainty on the location of the cut, and in turn, to an uncertainty on the measurement. If there is a data-MC scale shift in the reconstructed e^+e^- mass, the cut that is nominally at $15 \text{ MeV}/c^2$ will not be in the same location in data and MC.

We first determine what level of such a data-MC scale shift would be detectable; we scale the e^+e^- mass in data by various factors and monitor the data to MC overlay to see what size shift results in significant disagreement in the distribution. The level of e^+e^- mass shift detectable in this manner is a 0.5% shift, and this corresponds to losing an extra 41 events in data. Therefore, the uncertainty associated with the e^+e^- mass cut is $41/63,693 = .06\%$.

6.13 Monte Carlo Statistics

The statistical uncertainty on the ratio of acceptances, which is 0.20%, is taken as the error due to MC statistics. The size of the signal mode Monte Carlo sample limits this uncertainty. However, the MC statistical uncertainty of 0.20% is significantly lower than the statistical uncertainty (from data) of 0.40%.

6.14 Other Systematics Checks

To simulate the slight discrepancy between the observed size of the drift chambers and the survey measurements, a DC expansion factor is used in the Monte Carlo. The default expansion factor is 1.00023 for all DC planes, and this expansion is im-

plemented both during event generation and during reconstruction of MC events. To estimate our sensitivity to this aspect of the simulation, we use two tests. First, we change the simulation so that there is no expansion at generation, but the reconstruction uses the default expansion factor. Second, we change to no expansion in both the generation and the reconstruction. In the former test, the acceptance change is less than one sigma from the nominal acceptance. In the latter, the acceptance change is about 1.5 sigma. Therefore, our sensitivity to the simulation of the drift chamber expansion is negligible.

CHAPTER 7

CROSS CHECKS

To cross-check our measurement of $B(\pi^0 \rightarrow e^+e^-\gamma)/B(\pi^0 \rightarrow \gamma\gamma)$, we investigate how the result depends on several factors including cell separation, e^+e^- mass, beam intensity, and data-taking run. We also check the result for consistency within subsets of the nominal sample, such as for inbends versus outbends (see Section 7.5) and for the two polarities of the analysis magnet.

7.1 Cell Separation Dependence

Because we expected, a priori, that tracks with a small opening angle are not well-simulated in the Monte Carlo, we require the tracks to be more than 3 cells apart in the first two drift chambers (see Section 3.7.2). We now verify that the ratio of branching ratios does not change significantly in the vicinity of this cut. The number of reconstructed Dalitz events for each value of cell separation in both data and MC is used to compute the ratio of branching ratios for each value of cell separation. For each computation, we use the overall number of reconstructed $3\pi^0$ events in data and MC, as well as the overall number of generated events in both modes.

Figure 7.1 shows the ratio of branching ratios as a function of cell separation, focussing on the result for low values of cell separation. Each point uses an independent sample of reconstructed Dalitz events in data and in MC, with the first six points corresponding to events with a minimum cell separation equal to the bin number (0 through 5), and the last point corresponding to events with a minimum cell separation of 6 or greater (that is, all of the events not contained in the first six points). The line is the weighted average, and the χ^2 is 2.03 per 6 degrees of freedom, which corresponds to a 91.7% probability. The plot indicates that $B(\pi^0 \rightarrow e^+e^-\gamma)/B(\pi^0 \rightarrow \gamma\gamma)$

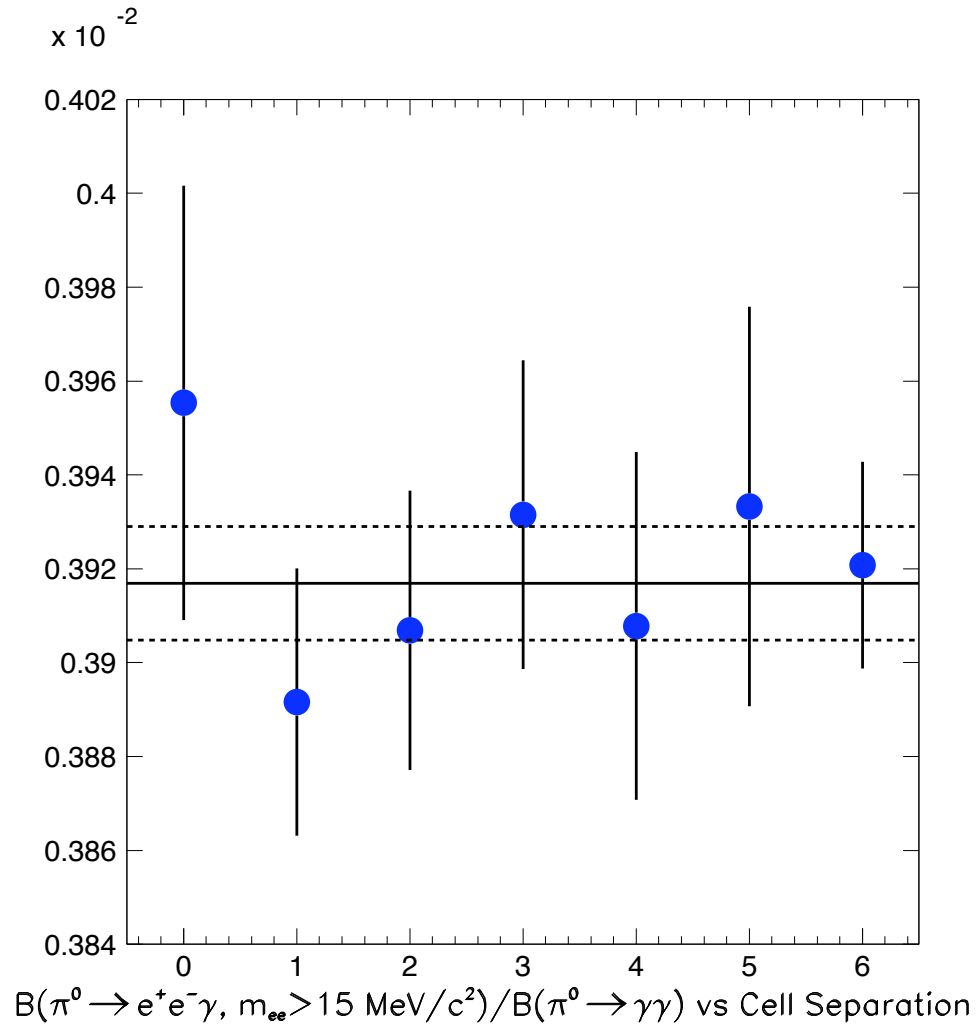


Figure 7.1: The ratio of branching ratios versus cell separation. The Dalitz events (both data and reconstructed MC events) that contribute to the answer in each of the first six bins are the events which have a minimum cell separation equal to the bin number. For example, the events in the cell separation = 0 bin all have a minimum cell separation of exactly 0. The last (seventh) point includes the rest of the events, that is, events which have a minimum cell separation greater than or equal to six. The error bars represent the independent statistical uncertainty in each bin. The solid horizontal line is the weighted average, and the dashed horizontal lines indicate the statistical uncertainty on the weighted average.

is stable as a function of cell separation.

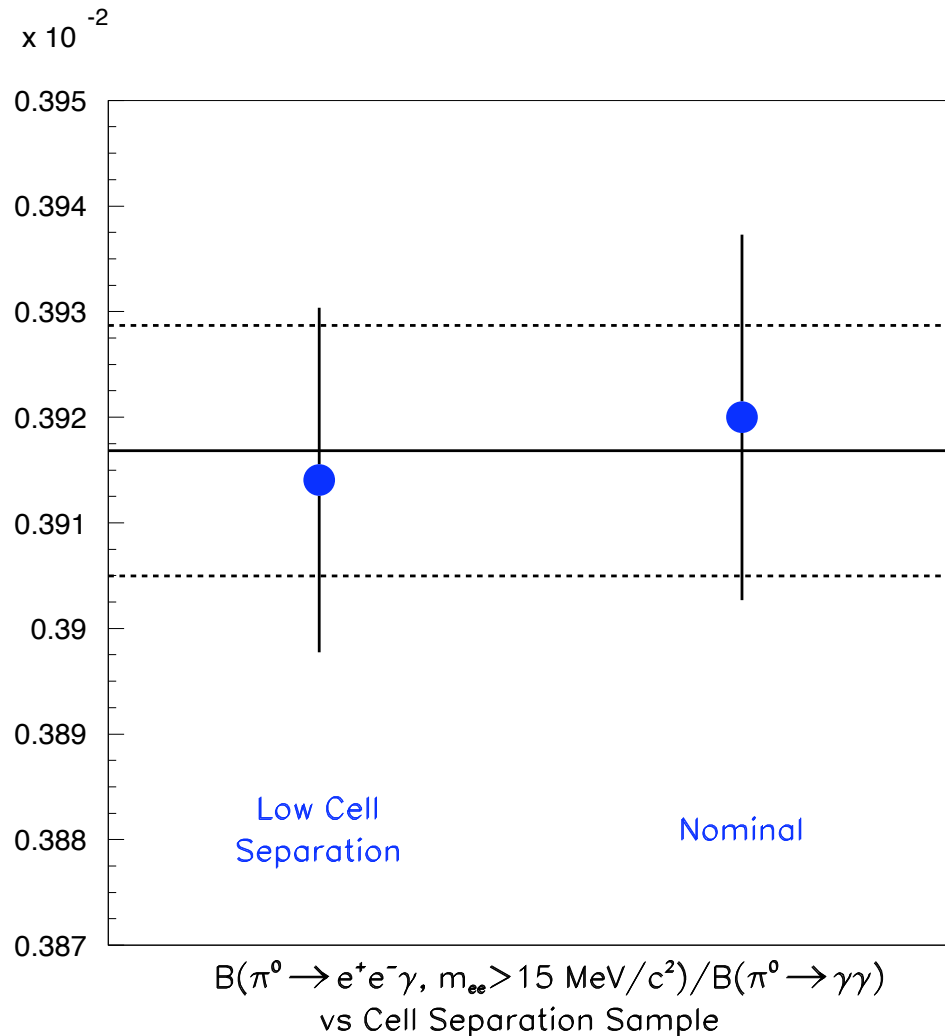


Figure 7.2: The ratio of branching ratios for the nominal sample on the right and for the sample of Dalitz events with low cell separations (less than or equal to 3 cells) on the left. The events in the low cell separation sample pass all other selection requirements. The error bars on the points indicate the uncertainty from the data and MC statistics on the Dalitz events in each (independent) sample. The solid line is the weighted average of the two points, and the dashed lines are the uncertainty on the weighted average.

The stability of $B(\pi^0 \rightarrow e^+e^-\gamma) / B(\pi^0 \rightarrow \gamma\gamma)$ can also be seen by comparing the nominal result to the result using the sample of events that are rejected only by the

cell separation requirement. Even with the requirement that the e^+e^- mass is greater than $15 \text{ MeV}/c^2$, the sample below the cell separation cut is slightly larger than the nominal sample.

Recall that the cell separation requirement effectively imposes an e^+e^- mass cutoff around $10 \text{ MeV}/c^2$, as shown in Fig. 3.12. However, the reverse is not true; although the e^+e^- mass requirement preferentially eliminates events with low cell separations, it does not result in a cell separation cutoff. There can be events with high e^+e^- mass but low cell separation. The cell separation cut is applied in both the x and y views of the drift chambers; that means, by definition, the cut rejects some fraction of events with large e^+e^- masses if the decay occurs very nearly vertically or horizontally (such that the two tracks are fully contained in either the x or y plane.)

Figure 7.2 shows $B(\pi^0 \rightarrow e^+e^-\gamma)/B(\pi^0 \rightarrow \gamma\gamma)$ in these two independent samples of events – those events that fail only the cell separation requirement and those events that pass the requirement (the nominal sample). The error bars are based on the independent statistical uncertainty for each sample. The results for the two samples are in very good agreement; the χ^2 is 0.06 per 1 degree of freedom (corresponding to an 80.2% probability).

7.2 e^+e^- Mass Dependence

We have seen that the e^+e^- mass distribution is very sensitive to radiative corrections, especially at the low end. The requirement that the e^+e^- mass be greater than $15 \text{ MeV}/c^2$ is imposed to avoid the low-mass region in part because of this sensitivity (in addition to the fact that the acceptance for events with low e^+e^- masses is very small). We have also noted that the requirement that the cell separation be greater than 3 cells effectively cuts off the e^+e^- mass distribution at $\sim 10 \text{ MeV}/c^2$; we can

use the events with e^+e^- masses between 10 and 15 MeV/c^2 as a cross check of our result. However, we first need to correct the result in each e^+e^- mass range to the result over the full kinematic range of the e^+e^- mass. We explain this procedure in detail for the nominal result in Section 8.1; for this cross check, we only quote the results.

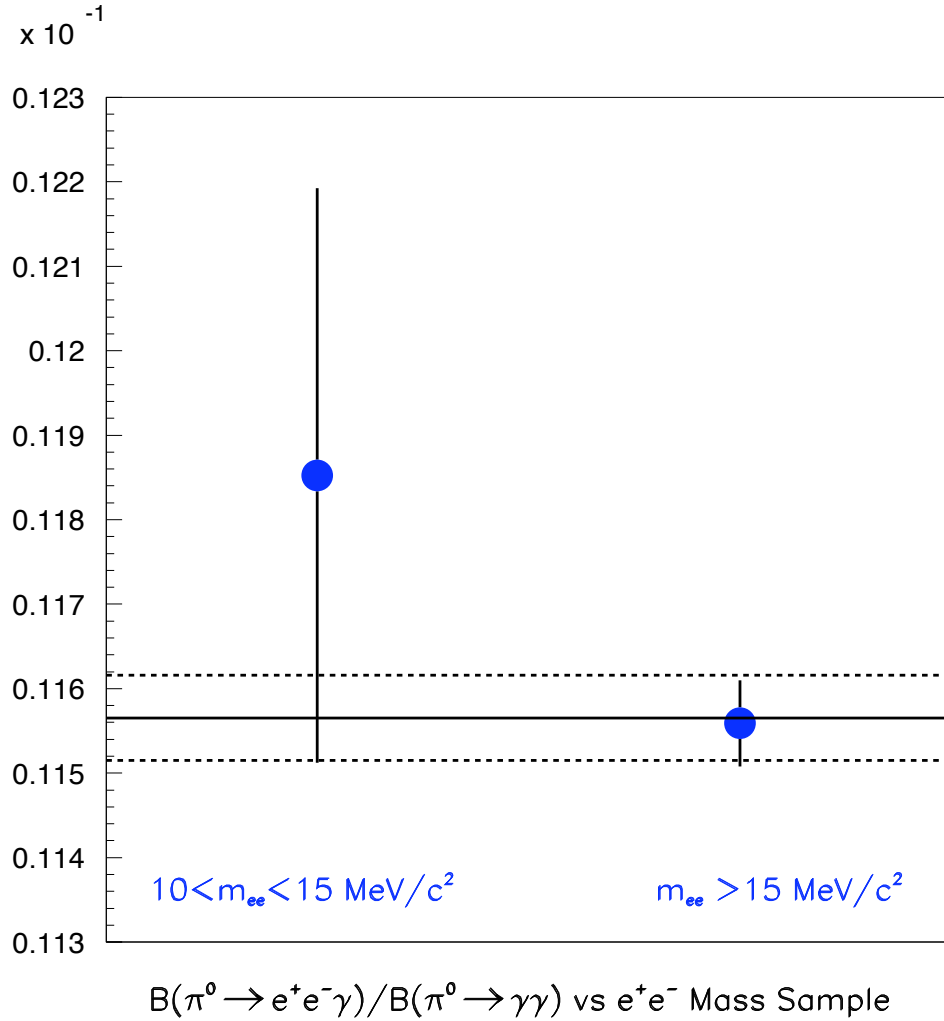


Figure 7.3: The result for events with e^+e^- mass between 10 and 15 MeV/c^2 that pass all other selection criteria, and the result for events in the nominal sample ($m_{e^+e^-} > 15 \text{ MeV}/c^2$). The error bars correspond to the independent statistical uncertainties in the two samples. The solid line is the weighted average and the dashed lines are the uncertainty on the weighted average.

Figure 7.3 shows $B(\pi^0 \rightarrow e^+e^-\gamma)/B(\pi^0 \rightarrow \gamma\gamma)$ (corrected to the full e^+e^- mass range) for the two independent samples of events – those events with an e^+e^- mass between 10 and 15 MeV/ c^2 that pass all other cuts and those events with an e^+e^- mass above 15 MeV/ c^2 (the nominal sample). The plot indicates agreement between the two samples, although the low e^+e^- mass sample has low statistics. The line indicates the weighted average, and the χ^2 is 0.73 per 1 degree of freedom, which is a 39.4% probability.

7.3 Intensity Dependence

As mentioned in Section 6.1, during 1999, E832 took data at several different beam intensities for systematic studies. Two intensities, “medium” and “high,” were used during nominal data-taking in addition to special low intensity runs, which are considered separately from the nominal data sample. The intensity is measured by the secondary emission monitor (SEM) in units of protons per spill. (Recall from Section 2.2 that each spill is approximately 40 seconds.) Although there were target SEM values for low, medium, and high intensity running, it is impossible to keep the intensity at a precise SEM value. Resolution effects, as well as turning the beam on and off, cause fluctuations in the intensity and deviations from the target SEM. For this reason, a run intended to be a medium intensity run contains some spills at low or high intensity. Table 7.1 gives the SEM ranges that correspond to the intensity samples for this analysis.

During data-taking, certain run ranges were used for medium intensity running, and others were used for high intensity running. While most events in a medium intensity run come from medium intensity spills, imperfections in controlling the beam intensity result in some low and high intensity spills during a medium intensity run.

| Intensity Sample | SEM Range ($\times 10^{12}$) (Protons per Spill) |
|------------------|---|
| Low | 0.0 – 3.0 |
| Medium | 3.0 – 5.5 |
| High | > 5.5 |

Table 7.1: The range of protons per spill corresponding to each of the three intensity ranges.

This is why, for this cross check, we create the intensity samples on an event-by-event (equivalent to spill-by-spill) basis rather than by grouping a particular set of runs together. Note that in the nominal analysis, some events fall into the low intensity range, even though none of the runs in the nominal analysis are low intensity runs; the number of such events is small and they are not used as part of this cross check (these events are, of course, included in the nominal result).

The low intensity data events from both modes are from two special low intensity runs that are not part of the nominal analysis (runs 14090 and 14092), which were crunched from the QKE tapes (QKE001-QKE018). The low intensity MC events were generated using accidental events corresponding to only these two run numbers. During data-taking, a series of special low intensity runs were intended to be used for systematics studies; unfortunately, problems with either trigger 6 or trigger 14 in several of these runs result in only two low intensity runs that are usable for cross checks for this analysis. Thus, the low intensity statistics are very poor, but we include them in the cross-check nonetheless.

Table 7.2 shows the number of reconstructed events in data and MC, the number of events generated in Monte Carlo, and the acceptance within each of the intensity ranges in each mode. In the Dalitz mode, the acceptance has already been corrected for the tracking inefficiency and the relative trigger inefficiency as was done for the nominal analysis in Section 5.2. The tracking inefficiency is applied separately to

the medium and high intensity samples based on the results of the tracking study described in Section 6.1; the medium intensity correction to the Dalitz acceptance is 0.9935 and the high intensity correction is 0.9928. No tracking correction is applied to the low intensity sample. The correction due to the trigger inefficiency is 0.9986 (determined in Section 6.5) for all three samples.

| Mode | Data Events | MC Events | MC Gen | Acceptance ($\times 10^{-2}$) | Error ($\times 10^{-2}$) |
|-----------------|-------------|-----------|-----------|------------------------------------|-------------------------------|
| $3\pi^0$ low | 33573 | 17366740 | 337616428 | 5.1439 | 0.0012 |
| Dalitz low | 608 | 186174 | 114468848 | 0.16241 | 0.00038 |
| $3\pi^0$ medium | 1612742 | 5772398 | 135643086 | 4.2556 | 0.0017 |
| Dalitz medium | 29573 | 121603 | 92003024 | 0.13113 | 0.00038 |
| $3\pi^0$ high | 1867849 | 6723682 | 193654697 | 3.4720 | 0.0013 |
| Dalitz high | 33147 | 140478 | 131331080 | 0.10605 | 0.00028 |

Table 7.2: Number of events in data and Monte Carlo, and acceptances (with errors) for both modes, in the special low intensity runs and in the medium and high intensity ranges of the nominal set of runs. In the Dalitz mode, the acceptance has been corrected for the tracking inefficiency and for the relative trigger inefficiency, as described in the text.

Using the number of events and acceptance in each intensity range, the ratio of branching ratios, $B(\pi^0 \rightarrow e^+e^-\gamma)/B(\pi^0 \rightarrow \gamma\gamma)$, is calculated independently in each intensity sample. The results are given in Table 7.3, and are shown in Fig. 7.4. The χ^2 for the weighted average in Fig. 7.4 is 7.4 per 2 degrees of freedom, corresponding to a probability of 2.4%.

Accidental activity increases with intensity. Looking at the MC with no accidental overlays allows us to see how much of a correction we would need if we did not simulate accidentals; the result for the ratio of branching ratios would be roughly 5% too low (see Fig. 7.5). Additionally, if accidentals are not simulated, there should be an intensity dependence in the result. We can see this by looking at the result using MC with no accidentals within each intensity sample. Because of the low statistics in the

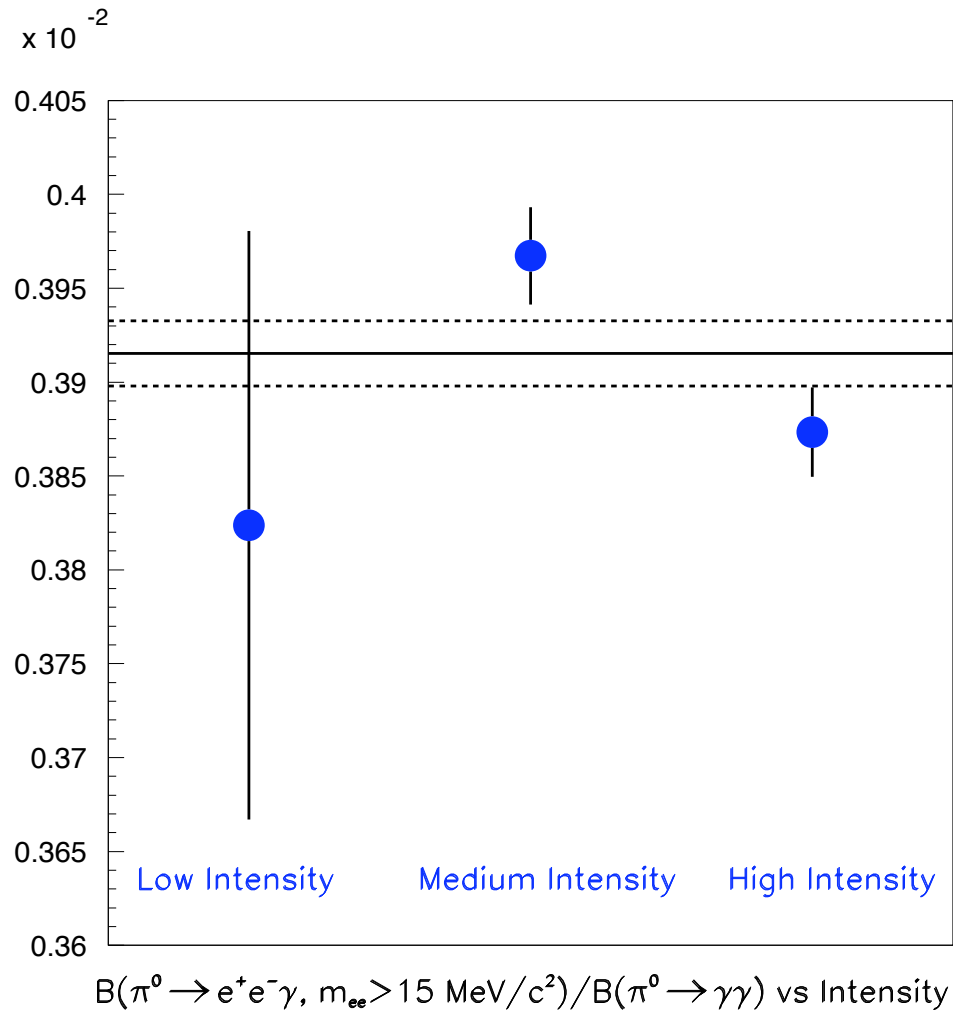


Figure 7.4: The dots are the ratio of branching ratios in each intensity sample. Note that the medium and high intensity samples are subsets of the nominal sample, while the low intensity sample is from a special set of runs described in the text. The solid line is the weighted average and the dashed lines indicate the uncertainty on the weighted average.

| Sample | $B(\pi^0 \rightarrow e^+e^-\gamma)/$ $B(\pi^0 \rightarrow \gamma\gamma)$ ($\times 10^{-2}$) | Stat. Error (Data and MC) ($\times 10^{-2}$) |
|------------------|---|--|
| Low Intensity | 0.3824 | 0.0157 |
| Medium Intensity | 0.3967 | 0.0026 |
| High Intensity | 0.3873 | 0.0024 |
| Nominal | 0.3920 | 0.0017 |

Table 7.3: The ratio of branching ratios in each intensity range as well as the error from both data and MC statistics. The nominal result is included for comparison.

special low-intensity runs, we only use the medium and high intensity samples in the nominal analysis for this part of the cross check. We compute the acceptances and $B(\pi^0 \rightarrow e^+e^-\gamma)/B(\pi^0 \rightarrow \gamma\gamma)$ in the medium and high intensity samples using MC with no accidental overlays, and compare to the results using nominal MC. Figure 7.5 shows the nominal result in the two intensity samples along with the weighted average (with uncertainties), as well as the results using no accidentals in the two intensity samples along with the weighted average.

We expect the accidentals to bring the results in the two intensity samples into better agreement with each other. Although it is not perfect, the results for the two intensity samples are in much better agreement when the MC with accidentals is used. The χ^2 for the results with nominal MC is 7.1 per 1 degree of freedom, which corresponds to a probability of 0.8%, while the χ^2 for the results using MC with no accidentals is 12.9 per 1 degree of freedom, which corresponds to a probability of 0.03%.

In order to further investigate any possible intensity dependence of the result, we next break up the 1999 runs into a series of run ranges according to average intensity during each run. For instance, runs 13670 through 13752 all had an average intensity within the medium intensity range (3.0×10^{12} to 5.5×10^{12} protons per spill); this

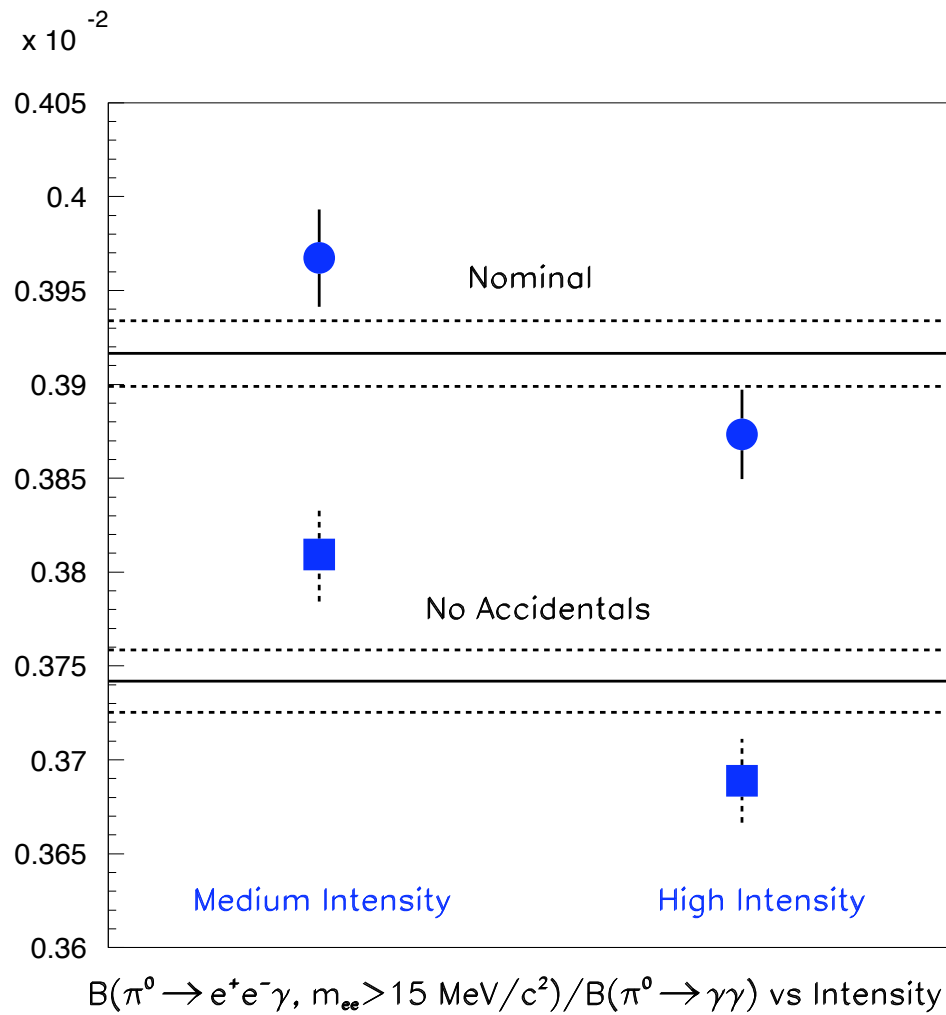


Figure 7.5: The dots are the result in the two intensity samples using nominal MC; the boxes are MC with no accidentals. The solid lines are the weighted averages of the result in the medium and high intensity samples for nominal MC and for MC with no accidentals. The dashed lines indicate the uncertainties on the weighted averages.

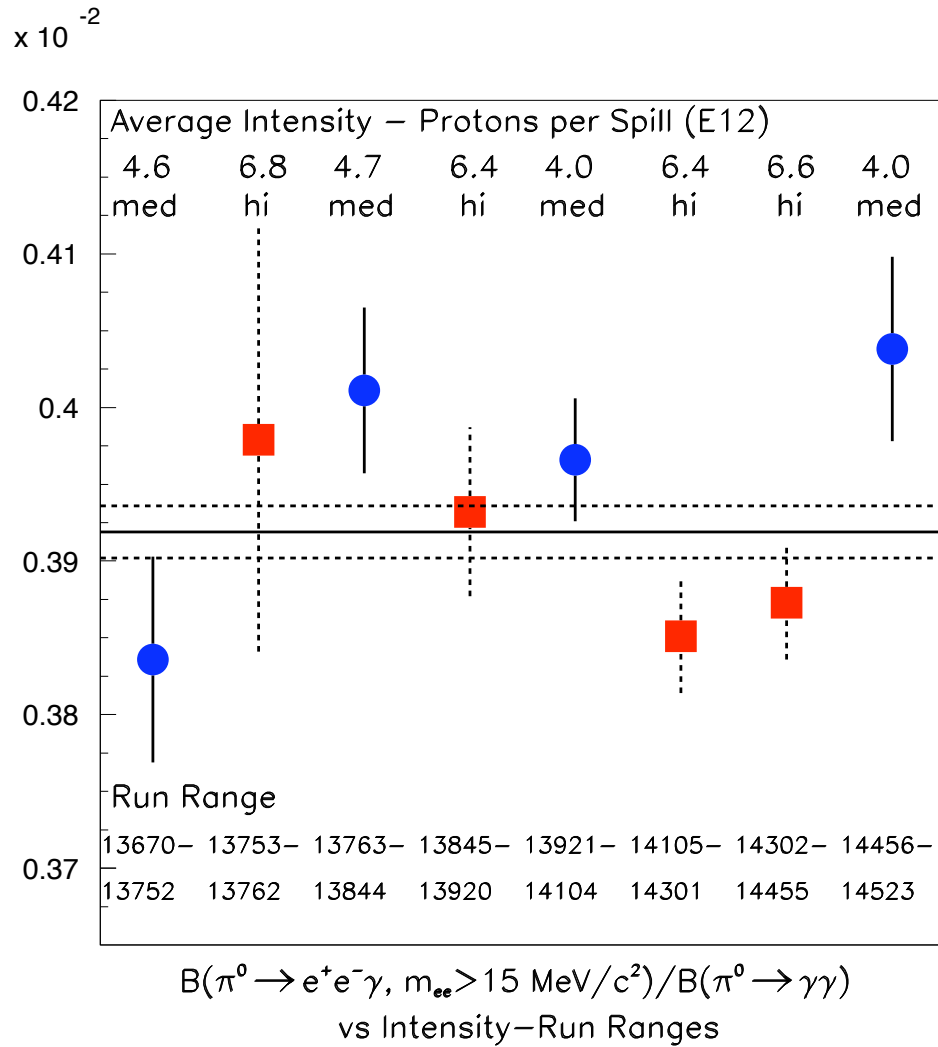


Figure 7.6: The points are the ratio of branching ratios in each of the eight subsamples described in the text. The run range and the average intensity is given for each subsample. The boxes indicate the results in the high intensity subsamples, while the dots indicate the results in the medium intensity subsamples. The error bars are the independent statistical uncertainties on each point. The solid line is the weighted average and the dashed lines indicate the uncertainty on the weighted average.

| Runs | Protons per Spill ($\times 10^{12}$) | Intensity |
|-------------|---|-----------|
| 13670-13752 | 4.6 | medium |
| 13753-13762 | 6.8 | high |
| 13763-13844 | 4.7 | medium |
| 13845-13920 | 6.4 | high |
| 13921-14104 | 4.0 | medium |
| 14105-14301 | 6.4 | high |
| 14302-14455 | 6.6 | high |
| 14456-14523 | 4.0 | medium |

Table 7.4: A list of the run ranges and the average intensities of each of the eight subsamples used in the final intensity dependence cross check described in the text.

run range is our first subsample. Table 7.4 lists the run ranges and average intensities for the eight subsamples.

We compute $B(\pi^0 \rightarrow e^+e^-\gamma)/B(\pi^0 \rightarrow \gamma\gamma)$ in each of the eight subsamples. Figure 7.6 shows the results, with the boxes for the high intensity subsamples and the dots for the medium intensity subsamples. The χ^2 for the result in these eight subsamples is 14.92 per 7 degrees of freedom, which corresponds to a probability of 3.7%. Recall from Fig. 7.4 that, overall, the high intensity result is less than the medium intensity result. Figure 7.6 shows that some of the high intensity data gives a result above the weighted average and some of the medium intensity data gives a result below the weighted average. This makes it unlikely that our result has an intensity dependence.

We perform one final independent cross-check which provides further evidence that there is no intensity dependence. Using random accepts from trigger 5 in the 1999 data, we look at $B(K_L \rightarrow \pi^\pm e^\mp \nu)/B(K_L \rightarrow 3\pi^0)$, which we abbreviate $B(Ke3)/B(K_L \rightarrow 3\pi^0)$, in each of the eight run-ranges in Table 7.4. The results are plotted in Fig. 7.7.

KTeV published a measurement of $B(K_L \rightarrow 3\pi^0)/B(Ke3)$ (the inverse of the

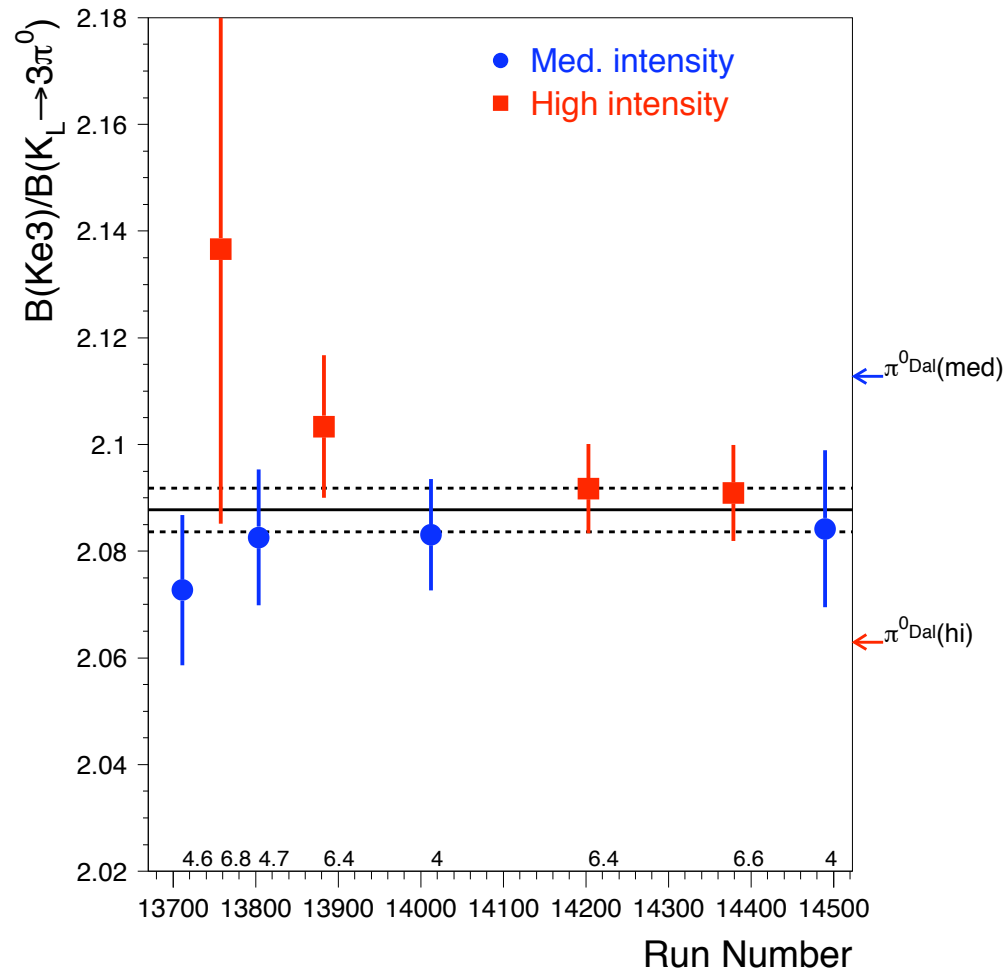


Figure 7.7: The points are the ratio of branching ratios of $K_L \rightarrow \pi^\pm e^\mp \nu$ (denoted Ke3) to $K_L \rightarrow 3\pi^0$ in each of the eight subsamples described in the text. The small numbers at the bottom of the plot are average intensity ($\times 10^{12}$) in each subsample. The boxes indicate the results in the high intensity subsamples, while the dots indicate the results in the medium intensity subsamples. The error bars are the independent statistical uncertainties on each point. The solid line is the weighted average and the dashed lines indicate the uncertainty on the weighted average. The small arrows outside the plot show the expected separation if the Ke3/ $3\pi^0$ high versus medium has the same ($\sim 2.4\%$) discrepancy as the Dalitz to $3\pi^0$ ratio of branching ratios. Figure courtesy of R. Kessler.

ratio plotted in Fig. 7.7) using trigger 5 random accepts from the 1997 dataset. This published result is $B(K_L \rightarrow 3\pi^0)/B(\text{Ke}3) = 0.4782 \pm 0.0014$ (stat) [38]. The measurement using the 1999 data of $B(K_L \rightarrow 3\pi^0)/B(\text{Ke}3) = 0.4798 \pm 0.0010$ (stat) is within one sigma (statistical) of the earlier published result.

This study of the intensity dependence of $B(\text{Ke}3)/B(K_L \rightarrow 3\pi^0)$ is a much higher statistics study than the intensity cross-check using our signal mode, and we observe no evidence of intensity dependence in the result. It should be noted that the cross check with Ke3 and $3\pi^0$ decays uses events from the same trigger (trigger 5); therefore, this cross check provides evidence that any detector-related intensity dependence is well-simulated in the Monte Carlo. It does not necessarily rule out intensity-dependent trigger issues; however, the systematics studies described in Section 6.5 indicate that potential trigger problems are small (corresponding to an uncertainty of $\sim 0.14\%$). Additionally, we imposed the same trigger and veto requirements in the signal and normalization modes to the extent possible (see Section 3.2), so that most trigger problems would cancel in the ratio of branching ratios, $B(\pi^0 \rightarrow e^+e^-\gamma)/B(\pi^0 \rightarrow \gamma\gamma)$.

7.4 Run Dependence

Another cross check involves comparing $B(\pi^0 \rightarrow e^+e^-\gamma)/B(\pi^0 \rightarrow \gamma\gamma)$ in each data-taking run to the overall result.

Recall that, before imposing any selection requirements, we check the data sample integrity (see Section 3.3) by looking at the ratio of the number of $3\pi^0$ events to the number of Dalitz events in each DAQ plane in each run, and comparing that ratio to the ratio over all runs. We use the statistical uncertainty within each run to determine, for each individual ratio, the number of sigma away from the overall average ratio.

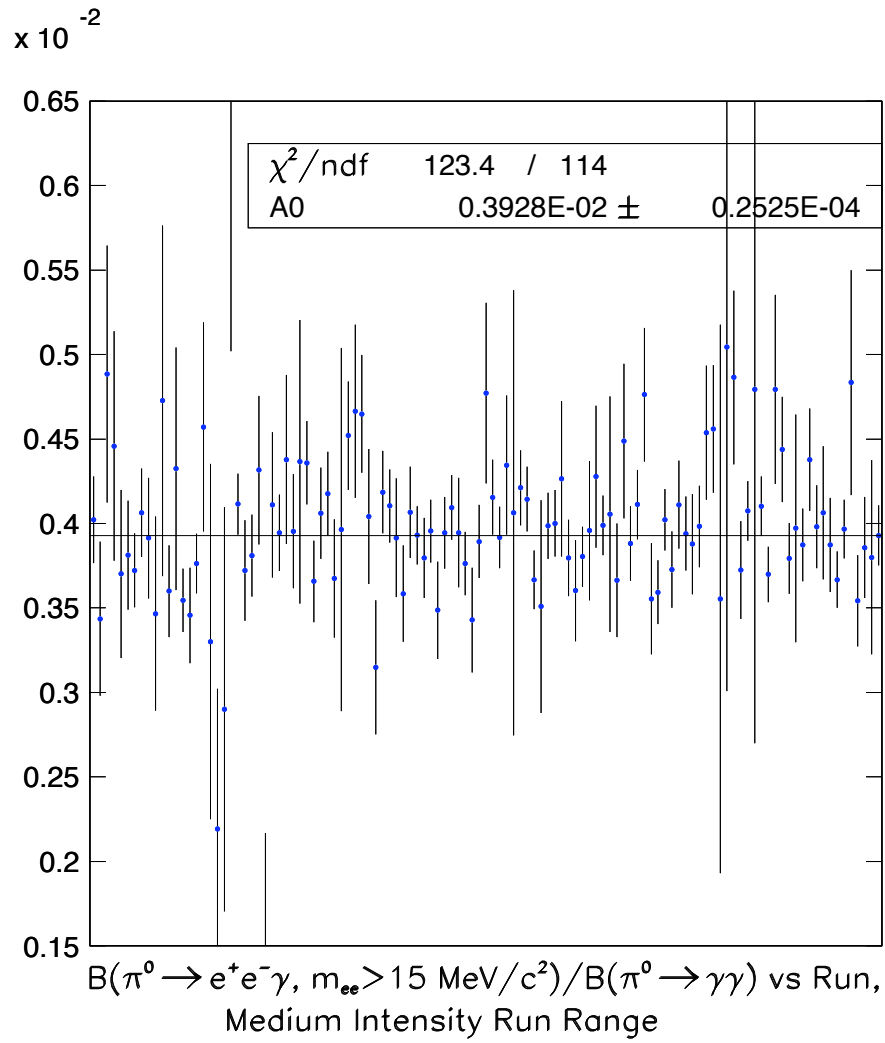


Figure 7.8: The ratio of branching ratios versus run, for medium intensity runs, which are defined as runs 13670 through 14104. (Note that this does not exactly correspond to the medium intensity sample, since events for the medium intensity sample are selected on a spill-by-spill basis.) Only runs which have a non-zero number of events are included. The error bars on the points are based on the independent statistical uncertainty in each run. The line is the weighted average across all medium intensity runs.

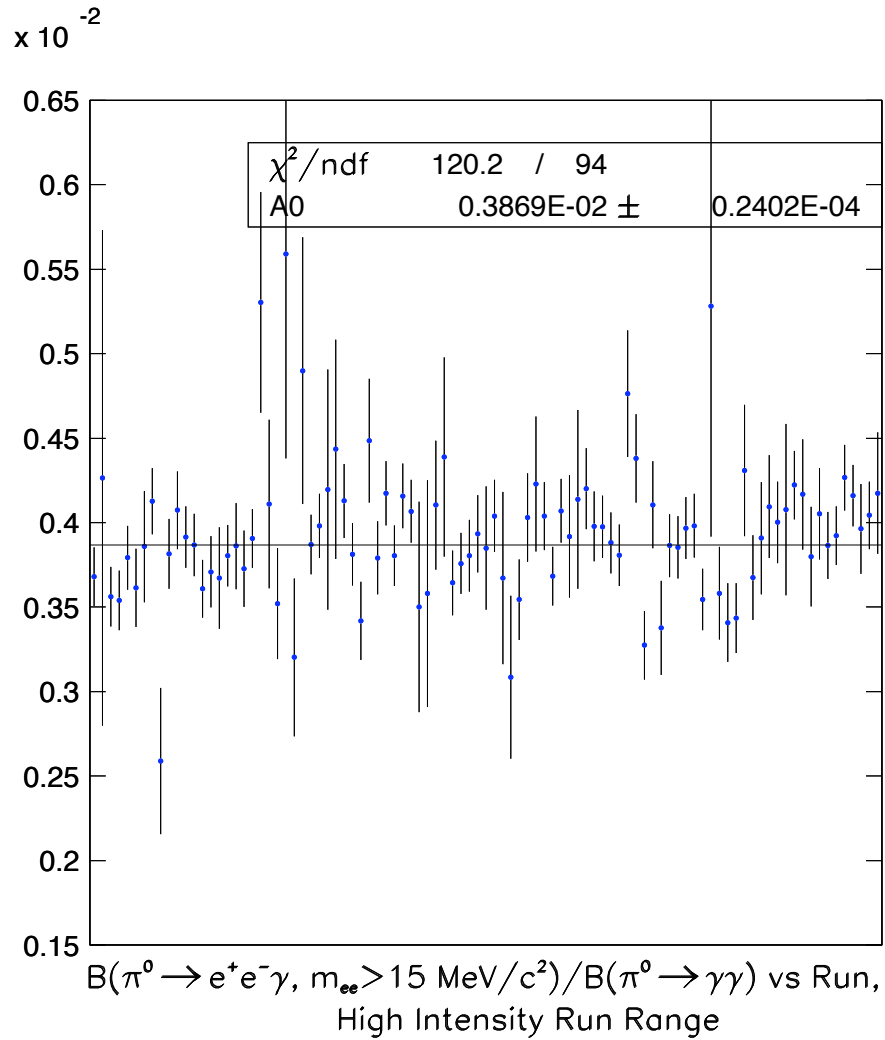


Figure 7.9: The ratio of branching ratios versus run, for high intensity runs, which are defined as runs 14105 through 14523. (Note that this does not exactly correspond to the high intensity sample, since events for the high intensity sample are selected on a spill-by-spill basis.) Only runs which have a non-zero number of events are included. The error bars on the points are based on the independent statistical uncertainty in each run. The line is the weighted average across all of the high intensity runs.

We then look at this sigma distribution to confirm that there are no outliers.

A similar check is performed after the analysis for events passing all selection requirements. For each run that has a non-zero number of events, we compute $B(\pi^0 \rightarrow e^+e^-\gamma)/B(\pi^0 \rightarrow \gamma\gamma)$ and its uncertainty based on the number of events reconstructed in data and in MC in both decay modes. The aim is to compare the run-by-run result with the result across all runs.

Recall from Section 7.3 that two beam intensities were used during data-taking. To focus on a possible run-dependence of the result in this study, it is appropriate to perform this cross check separately for the medium intensity runs and for the high intensity runs. As mentioned, not all of the events in a particular run are at the target intensity for that run, but the majority of events are. Although we broke the 1999 run range into eight intensity samples in Section 7.3, here it is sufficient to use two samples. Roughly, runs 13670-14104 were taken at medium intensity, while runs 14105-14523 were taken at high intensity. For this cross check, we will use these run ranges to break the nominal sample into two subsamples.

Figure 7.8 shows $B(\pi^0 \rightarrow e^+e^-\gamma)/B(\pi^0 \rightarrow \gamma\gamma)$ for each run in the medium intensity run range along with the weighted average. The χ^2 is 123.4 for 114 degrees of freedom, which corresponds to a probability of 25.9%. Figure 7.9 is the same plot for the high intensity run range; the χ^2 is 120.2 for 94 degrees of freedom, corresponding to a probability of 3.6%.

7.5 Inbends versus Outbends

We can separate the signal mode event sample into “inbends” and “outbends,” based on whether the tracks bend toward or away from each other at the analysis magnet. Figure 7.10 shows the track configurations corresponding to inbends and outbends.

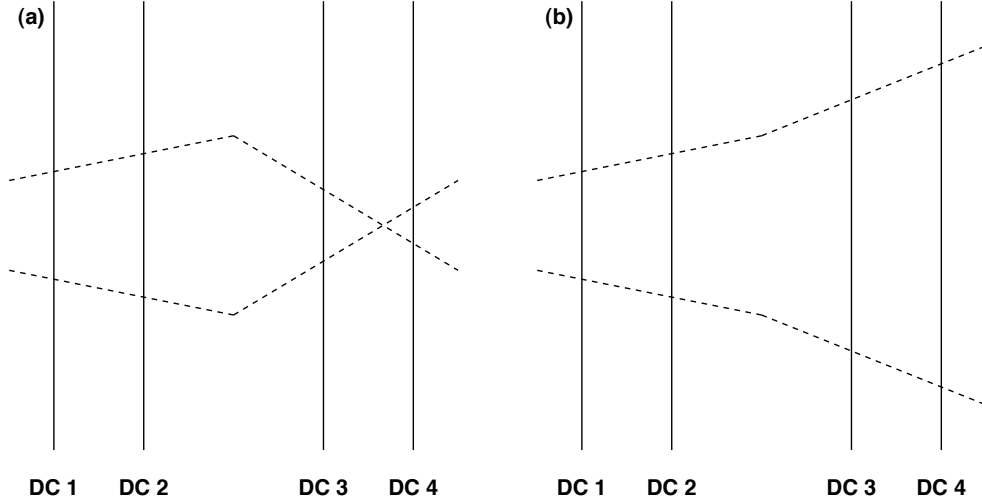


Figure 7.10: The track configuration corresponding to (a) an inbend event and (b) an outbend event.

Figure 7.11 shows the result, $B(\pi^0 \rightarrow e^+e^-\gamma)/B(\pi^0 \rightarrow \gamma\gamma)$, separately for inbends and for outbends, along with the weighted average for the two samples. Note that the weighted average is just the nominal result for $B(\pi^0 \rightarrow e^+e^-\gamma)/B(\pi^0 \rightarrow \gamma\gamma)$, as expected. The χ^2 is 2.20 per 1 degree of freedom, corresponding to a probability of 13.8%.

7.6 Magnet Polarity

We can separate the signal mode event sample into subsamples taken with each of the two polarities of the analysis magnet. As mentioned in Section 2.4.1, the magnetic field was reversed periodically during data-taking to reduce systematic biases related to the field orientation. Although the magnet should not affect the $3\pi^0$ events, we can also separate the normalization sample into events collected during each of the two magnet polarities. The calculation of $B(\pi^0 \rightarrow e^+e^-\gamma)/B(\pi^0 \rightarrow \gamma\gamma)$ will therefore be independent in the two magnet polarity samples.

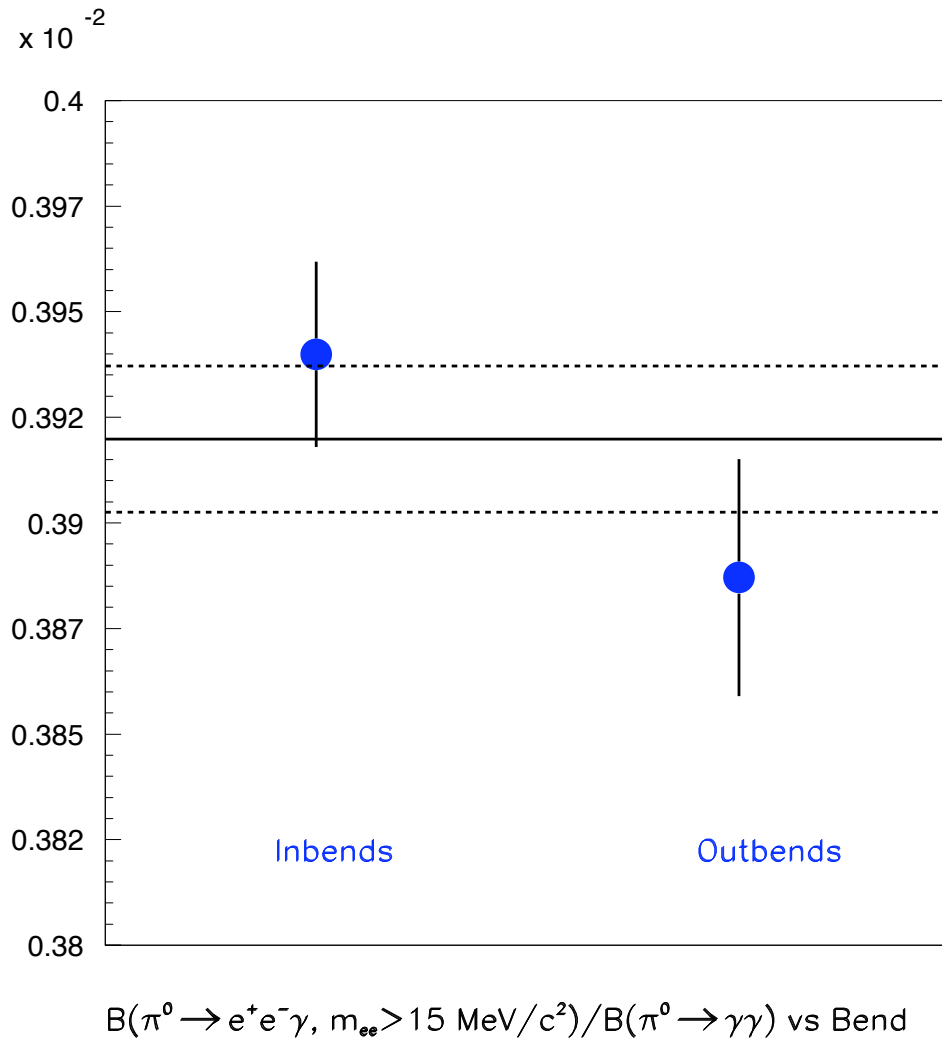
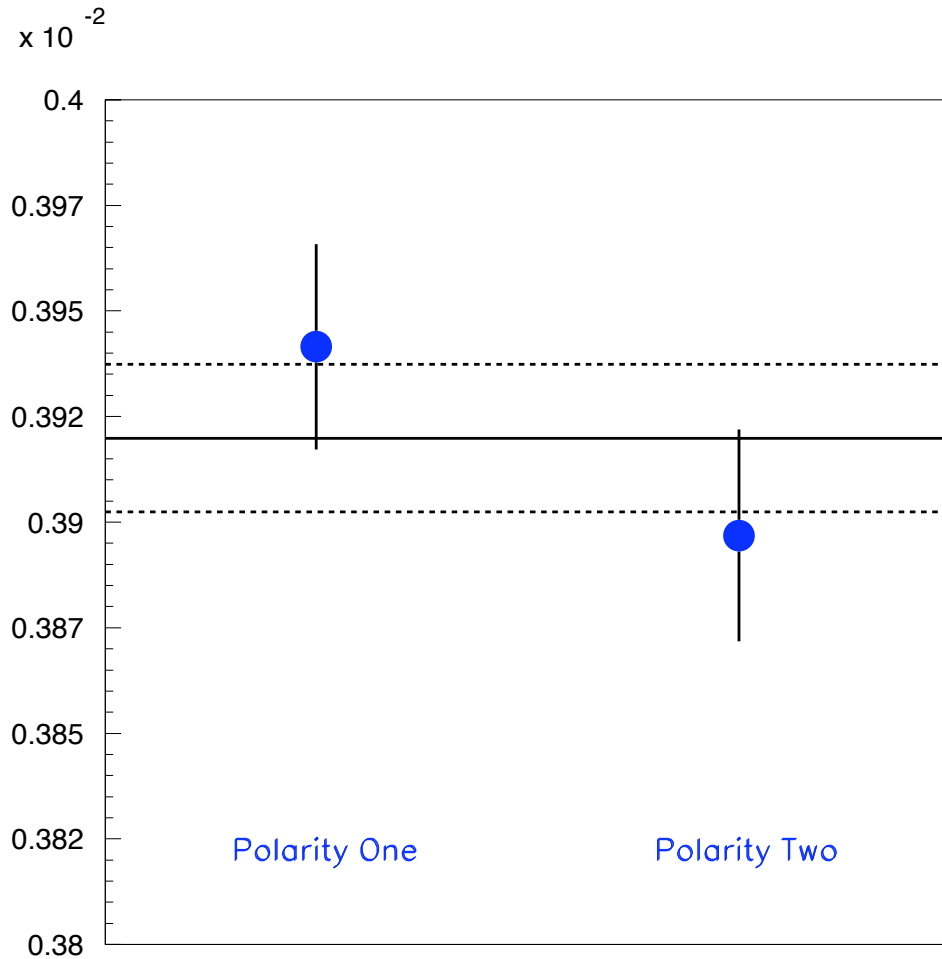


Figure 7.11: The ratio of branching ratios in the two subsamples of the nominal sample corresponding to which way the tracks bend at the magnet, denoted inbends and outbends. The uncertainties on the two points are based on the reconstructed Dalitz event statistics in data and MC. The solid line is the weighted average and the dashed lines indicate the uncertainty on the weighted average.

Figure 7.12 shows the result separately for the two analysis magnet polarities, along with the weighted average for the two samples. The weighted average is just the nominal result for $B(\pi^0 \rightarrow e^+e^-\gamma)/B(\pi^0 \rightarrow \gamma\gamma)$, as expected. The χ^2 is 1.64 per 1 degree of freedom, corresponding to a probability of 20.1%.



$B(\pi^0 \rightarrow e^+e^-\gamma, m_{ee} > 15 \text{ MeV}/c^2)/B(\pi^0 \rightarrow \gamma\gamma)$ vs Magnet Polarity

Figure 7.12: The ratio of branching ratios in the two subsamples of the nominal sample corresponding to the two analysis magnet polarities. The uncertainties on the two points are based on the reconstructed event statistics in data and MC for both decay modes. The solid line is the weighted average and the dashed lines indicate the uncertainty on the weighted average.

CHAPTER 8

CONCLUSION

In this dissertation, we have presented a measurement of the Dalitz decay branching ratio for e^+e^- masses greater than $15 \text{ MeV}/c^2$. In order to compare to previous measurements and to use the result as the normalization mode in branching ratio measurements of rare pion and kaon decays, we need to correct the result to the full kinematic range of the e^+e^- pair.

8.1 Final Result

In Section 5.3, we calculated our result with the e^+e^- mass cut at $15 \text{ MeV}/c^2$ to be $B(\pi^0 \rightarrow e^+e^-\gamma, m_{e^+e^-} > 15 \text{ MeV}/c^2)/B(\pi^0 \rightarrow \gamma\gamma) = 0.3920 \times 10^{-2}$. We correct our measurement to the full e^+e^- mass range by relying on the Mikaelian and Smith [12] calculation of the e^+e^- mass spectrum as implemented in the KTeV MC to predict the number of events generated below our $15 \text{ MeV}/c^2$ e^+e^- mass cutoff.

Since there are 226,985,152 events generated above the e^+e^- mass cutoff, and 669,320,768 events generated over the entire mass range, our measurement accounts for $226,985,152/669,320,768 = 0.339128$ of the Dalitz decays. To correct to the full e^+e^- mass range, we need to divide our measurement by this fraction.

Correcting to the full e^+e^- mass range results in $B(\pi^0 \rightarrow e^+e^-\gamma)/B(\pi^0 \rightarrow \gamma\gamma) = 1.1559\%$. With a statistical uncertainty of 0.40% and a systematic uncertainty of 0.93% (for a total relative uncertainty of 1.01%), we have a final result of

$$B(\pi^0 \rightarrow e^+e^-\gamma)/B(\pi^0 \rightarrow \gamma\gamma) = (1.1559 \pm 0.0046 \pm 0.0107)\%. \quad (8.1)$$

8.2 Comparison to Previous Measurements and to Theory

A summary of the previous measurements, the prediction from theory, and this new result of $B(\pi^0 \rightarrow e^+e^-\gamma)/B(\pi^0 \rightarrow \gamma\gamma)$ is given in Table 8.1. Figure 8.1 shows these previous measurements and the theoretical prediction along with this new result from KTeV. The uncertainty on this new measurement is less than half the PDG uncer-

| Year | Author | $\frac{B(\pi^0 \rightarrow e^+e^-\gamma)}{B(\pi^0 \rightarrow \gamma\gamma)}$ (%) | Uncertainty | Reference |
|------|-----------------------------|---|--------------|-----------|
| 1960 | Budagov | 1.17 | ± 0.15 | [21] |
| 1961 | Samios | 1.166 | ± 0.047 | [20] |
| 1972 | Theory Mikaelian & Smith | 1.196 | ± 0.012 | [12] |
| 1981 | Schardt | 1.25 | ± 0.04 | [19] |
| 2007 | KTeV | 1.1559 | ± 0.0117 | - |

Table 8.1: A summary of the previous measurements and theoretical prediction for the π^0 Dalitz decay branching ratio.

tainty [4] and a factor of 3 better than any single previous measurement. Combining the three previous measurements of $B(\pi^0 \rightarrow e^+e^-\gamma)/B(\pi^0 \rightarrow \gamma\gamma)$ with this new result gives a new world average of $(1.1635 \pm 0.0109)\%$.

In Table 8.1 and in Fig. 8.1, we have estimated a 1% uncertainty on the theoretical prediction based on comments in [12]. With this level of uncertainty, our result agrees with the theory at the 2.4 sigma level.

8.3 Effect of New Result on Other Measurements

Part of the motivation for measuring $B(\pi^0 \rightarrow e^+e^-\gamma)/B(\pi^0 \rightarrow \gamma\gamma)$ stems from its use as a normalization mode in many rare decays of pions and kaons, some of which are listed in Section 1.1; that list is reproduced here:

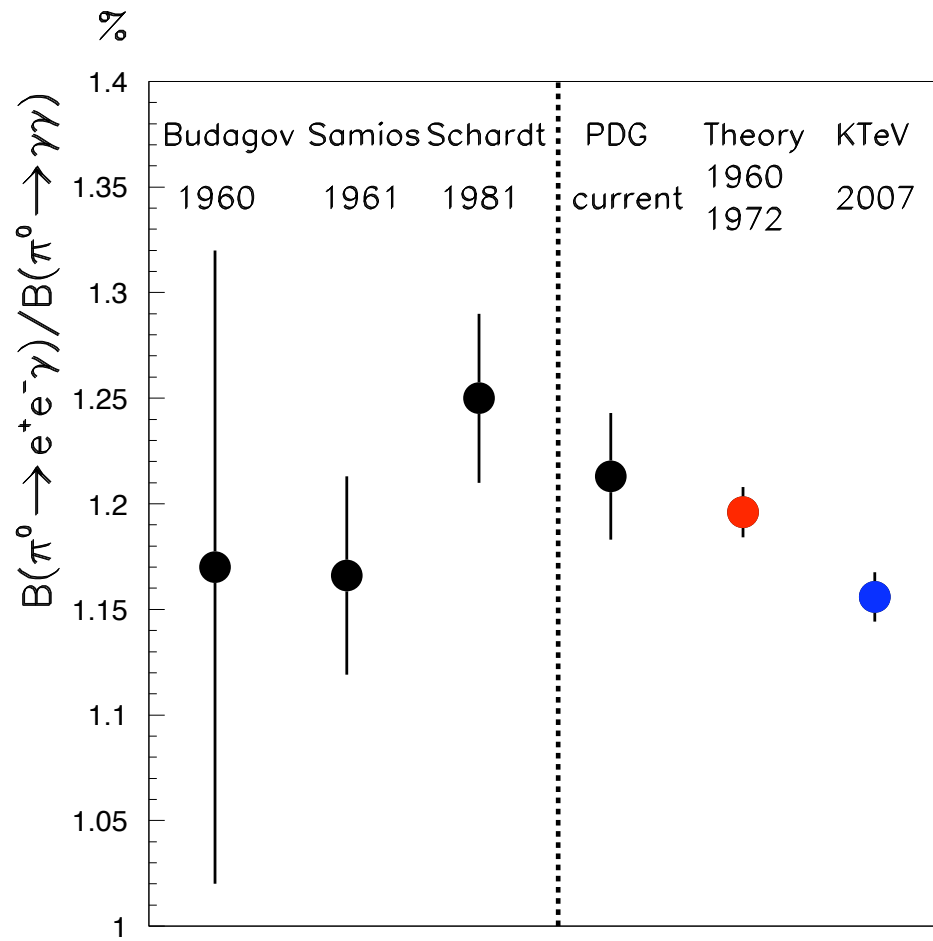


Figure 8.1: A comparison of previous measurements, theoretical predictions, and this KTeV measurement of $B(\pi^0 \rightarrow e^+e^-\gamma)/B(\pi^0 \rightarrow \gamma\gamma)$.

- $\pi^0 \rightarrow e^+e^-$
- $K_L \rightarrow e^+e^-\gamma$
- $K_L \rightarrow e^+e^-e^+e^-$
- $K_L \rightarrow \pi^+\pi^-\pi^0e^+e^-$
- $K_L \rightarrow \pi^0e^+e^-\gamma$
- $K_L \rightarrow \pi^0\pi^0\gamma$

The uncertainty on the π^0 Dalitz branching fraction is taken as an external systematic uncertainty in the measurement of each of these decay modes. Note that the $K_L \rightarrow e^+e^-e^+e^-$ decay is normalized to $K_L \rightarrow \pi^0\pi_D^0\pi_D^0$, and therefore has to take twice the uncertainty on the π^0 Dalitz branching fraction as part of its systematic uncertainty [40]. To illustrate the effect of this new measurement of the $\pi^0 \rightarrow e^+e^-\gamma$ branching fraction (and its significantly smaller uncertainty), we correct recent KTeV results for two of the above decay modes: $\pi^0 \rightarrow e^+e^-$ and $K_L \rightarrow e^+e^-\gamma$.

8.3.1 Correcting the KTeV measurement of $B(\pi^0 \rightarrow e^+e^-)$

The KTeV collaboration recently published a new result for $B(\pi^0 \rightarrow e^+e^-)$ with $\pi^0 \rightarrow e^+e^-\gamma$ as the normalization mode [41]. Using the 2006 PDG average for the branching ratio of $\pi^0 \rightarrow e^+e^-\gamma$, they calculate an absolute branching ratio of $B(\pi^0 \rightarrow e^+e^-, x_D > 0.95) = (6.44 \pm 0.25 \pm 0.22) \times 10^{-8}$ (with $x_D = (m_{e^+e^-}/m_\pi)^2$), where the first uncertainty is from statistics and the second is from systematics, including a 2.7% external uncertainty from $B(\pi^0 \rightarrow e^+e^-\gamma)$. Correcting this result using our measurement of $B(\pi^0 \rightarrow e^+e^-\gamma)$ yields a slightly lower central value and a smaller systematic uncertainty: $B(\pi^0 \rightarrow e^+e^-, x_D > 0.95) = (6.14 \pm 0.24 \pm 0.15) \times 10^{-8}$. Figure 8.2 compares the result for $B(\pi^0 \rightarrow e^+e^-)$ using the 2006 PDG average of $B(\pi^0 \rightarrow e^+e^-\gamma)$ with the result for $B(\pi^0 \rightarrow e^+e^-)$ using this measurement of $B(\pi^0 \rightarrow e^+e^-\gamma)$.

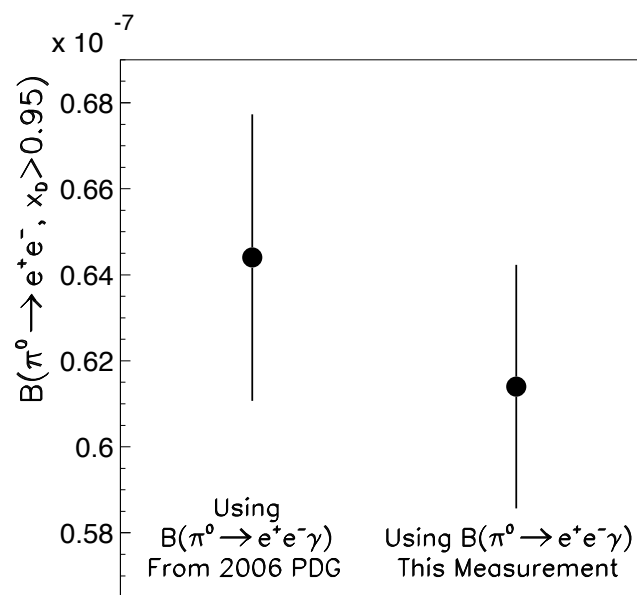


Figure 8.2: The recent KTeV result for $B(\pi^0 \rightarrow e^+e^-)$, using the 2006 PDG average for the normalization decay mode ($\pi^0 \rightarrow e^+e^-\gamma$) branching ratio (left) and corrected using this new result for the $\pi^0 \rightarrow e^+e^-\gamma$ branching ratio (right).

8.3.2 Correcting the KTeV measurement of $B(K_L \rightarrow e^+e^-\gamma)$

The KTeV collaboration recently published a new result for $B(K_L \rightarrow e^+e^-\gamma)$ [42], where the normalization mode is $K_L \rightarrow \pi^0\pi^0\pi_D^0$. The relative external systematic uncertainty from the normalization mode is 2.83%, most of which comes from the uncertainty on $B(\pi^0 \rightarrow e^+e^-\gamma)$. The KTeV measurement uses the 2006 PDG result for $B(\pi^0 \rightarrow e^+e^-\gamma)$, and finds $B(K_L \rightarrow e^+e^-\gamma) = (9.128 \pm 0.032 \pm 0.070 \pm 0.252) \times 10^{-6}$, where the first uncertainty is from statistics, the second is from systematics, and the third is the external uncertainty from the normalization. Correcting this result using our measurement of $B(\pi^0 \rightarrow e^+e^-\gamma)$ yields a slightly lower central value and a smaller external systematic uncertainty: $B(K_L \rightarrow e^+e^-\gamma) = (8.701 \pm 0.030 \pm 0.067 \pm 0.108) \times 10^{-6}$. Figure 8.3 compares the KTeV result for $B(K_L \rightarrow e^+e^-\gamma)$ using the 2006 PDG average of $B(\pi^0 \rightarrow e^+e^-\gamma)$ with the result for $B(K_L \rightarrow e^+e^-\gamma)$ using this measurement of $B(\pi^0 \rightarrow e^+e^-\gamma)$.

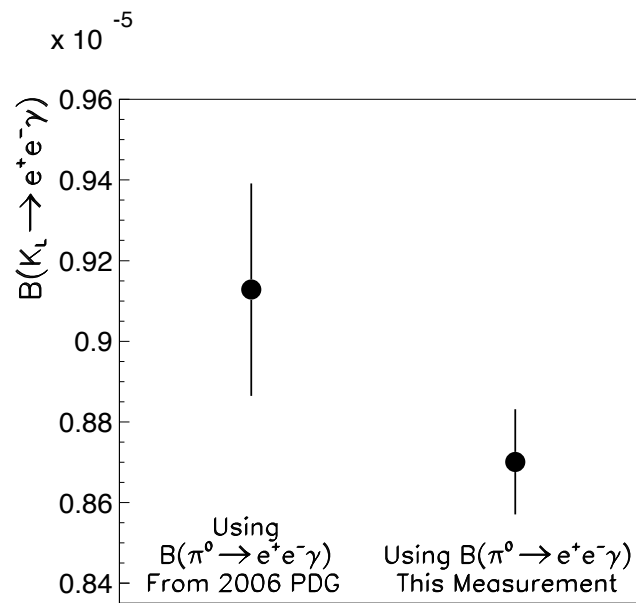


Figure 8.3: The recent KTeV result for $B(K_L \rightarrow e^+e^-\gamma)$, using the 2006 PDG average for $B(\pi^0 \rightarrow e^+e^-\gamma)$ in the normalization decay mode branching ratio (left) and corrected using this new result for the $\pi^0 \rightarrow e^+e^-\gamma$ branching ratio (right).

REFERENCES

- [1] R. H. Dalitz. *Proc. Phys. Soc. (London)*, A64, 1951.
- [2] J. Steinberger. *Phys. Rev.*, 76, 1949.
- [3] J. Steinberger et al. *Phys. Rev.*, 78, 1950.
- [4] W.-M. Yao et al. (Particle Data Group). *J. Phys.*, G33, 2006.
- [5] N. Kroll and W. Wada. *Phys. Rev.*, 98, 1955.
- [6] L.G. Landsberg. *Phys. Rep.*, 128, 1985.
- [7] R. Meijer Drees et al. *Phys. Rev.*, D45, 1992.
- [8] F. Farzanpay et al. *Phys. Let.*, B278, 1992.
- [9] H. Fonvieille et al. *Phys. Let.*, B233, 1989.
- [10] B.E. Lautrup and J. Smith. *Phys. Rev.*, D3, 1971.
- [11] D. Joseph. *Nuovo Cimento*, 16, 1960.
- [12] K.O. Mikaelian and J. Smith. *Phys. Rev.*, D5, 1972.
- [13] K. Kampf, M. Knecht, and J. Novotny. *Int. Conf. Hadron Structure*, 2002.
- [14] K. Kampf, M. Knecht, and J. Novotny. *Eur. Phys. J.*, C46, 2006.
- [15] R.W. Brown. *Phys. Rev.*, D1, 1970.
- [16] M. Lambin and J. Pestieau. *Phys. Rev.*, D31, 1985.
- [17] G.B. Tupper et al. *Phys. Rev.*, D28, 1984.
- [18] D. Beder. *Phys. Rev.*, D34, 1986.
- [19] M.A. Schardt et al. *Phys. Rev.*, D23, 1981.
- [20] N.P. Samios. *Phys. Rev.*, 121, 1961.
- [21] Y.A. Budagov et al. *JETP*, 11, 1960.
- [22] R.A. Daniel, J.H. Davies, J.H. Mulvey, and D.H. Perkins. *Phil. Mag.*, 43, 1952.
- [23] J. Lord, J. Fainberg, D. Haskin, and M. Schein. *Phys. Rev.*, 87, 1952.
- [24] B.M. Anand. *Proc. Phys. Soc. (London)*, A220, 1953.

- [25] P. Lindenfeld, A. Sachs, and J. Steinberger. *Phys. Rev.*, 89, 1953.
- [26] C.P. Sargent, R. Cornelius, M. Rinehart, L.M. Lederman, and K. Rogers. *Phys. Rev.*, 98, 1955.
- [27] A. Alavi-Harati et al. *Phys. Rev.*, D67, 2003.
- [28] J.A. Graham. *PhD Thesis, University of Chicago*, 2001.
- [29] V. Prasad. *PhD Thesis, University of Chicago*, 2002.
- [30] P.S. Shawhan. *PhD Thesis, University of Chicago*, 1999.
- [31] J. Whitmore. *Nucl. Instrum. Methods Phys. Res.*, A409, 1998.
- [32] T. Barker and U. Nauenberg. *KTeV Internal Memo*, 102, 1993.
- [33] T. Barker and U. Nauenberg. *KTeV Internal Memo*, 132, 1993.
- [34] E.D. Zimmerman. *PhD Thesis, University of Chicago*, 1999.
- [35] T. Alexopoulos et al. *Phys. Rev. Lett.*, 93, 2004.
- [36] A.J. Malensek. *Fermilab Report*, FN-341(E), 1981.
- [37] R. Brun et al. *GEANT 3.21*, 1994.
- [38] T. Alexopoulos et al. *Phys. Rev.*, D70, 2004.
- [39] A. Alavi-Harati et al. Sdaq documentation. *KTeV Internal Note*, 625, 1999.
- [40] A. Alavi-Harati et al. *Phys. Rev. Lett.*, 86:5425–5429, 2001.
- [41] E. Abouzaid et al. *Phys. Rev.*, D75, 2007.
- [42] E. Abouzaid et al. *Phys. Rev.*, D74, 2006.